2018

Multiscale modelling of martensitic phase transformation: Example of Si I to Si II

Hao Chen
Iowa State University

Multiscale modelling of martensitic phase transformation: Example of Si I to Si II

by

Hao Chen

A dissertation submitted to the graduate faculty

in partial fulfillment of the requirements for the degree of

DOCTOR OF PHILOSOPHY

Major: Engineering Mechanics

Program of Study Committee:
Liming Xiong, Co-major Professor
Valery I. Levitas, Co-major Professor
Ashraf Bastawros
Azadeh Sheidaei
Baskar Ganapathysubramanian

The student author, whose presentation of the scholarship herein was approved by the program of study committee, is solely responsible for the content of this dissertation. The Graduate College will ensure this dissertation is globally accessible and will not permit alterations after a degree is conferred.

Iowa State University

Ames, Iowa

2018

DEDICATION

I would like to dedicate this thesis to my father Jianhua Chen, Liangmei Liang and my sister Yan Chen for their continuous support.

TABLE OF CONTENTS

Page

LIST OF TABLES

Page

LIST OF FIGURES

Page

ACKNOWLEDGMENTS

I would like to take this opportunity to express my thanks to those who helped me with various aspects of conducting research and the writing of this thesis. First and foremost, Dr. Liming Xiong and Dr. Valery Levitas for their guidance, patience and support throughout this research and the writing of this thesis. Their insights and words of encouragement have often inspired me and renewed my hopes for completing my graduate education. I would also like to thank my committee members for their efforts and contributions to this work: Dr. Ashraf Bastawros, Dr. Azadeh Sheidaei, Dr. Vinay Dayal and Dr. Baskar Ganapathysubramanian I would additionally like to thank my friends Ji Rigelesaiyin, Thanh Phan, Yipeng Peng, Dr. Anup Basak, Dr. Krishan Kumar Pandey, Hamed Babaei, Ehsan Esfahani, Mehdi Kamrani, Dr. Senlin Cui, Dr. Biao Feng and Dr. Yong Seok Hwang in our group to help me and discuss with me about problems. I also want to thank Dr. Oleg Zarechnyy for helping me with the TA task.

ABSTRACT

Martensitic phase transformations (PTs), amorphization, twinning, and dislocation motion are the main deformation mechanisms in many crystalline materials. However, the interaction between these material behaviors are not well understood. In this work, we try to understand the interaction between dislocation motion and PTs through multiscale modelling using density functional theory (DFT, in collaboration with Drs. Zarkevich and Johnson from Ames Laboratory), molecular dynamics (MD), continuum mechanics and concurrent atomistic-continuum (CAC) method. The following topics are discussed.

1. A continuum/atomistic approach for predicting lattice instability during martensitic PTs is developed for the general loading with an arbitrary stress tensor and large strains. It was applied to the transformation between semiconducting Si I and metallic Si II phases. The instability criterion represents the critical value of the modified transformation work, which is linear in normal to cubic faces components of the true stress tensor and is independent of shear stresses.

2. Starting with thermodynamic predictions and combining with MD simulations, special triaxial compression-tension states were found at which the stresses for the instability of the crystal lattice of silicon are the same for direct and reverse Si I $\leftrightarrow$ Si II PTs. This leads to unique homogeneous and hysteresis-free first-order PTs. Zero hysteresis and homogeneous transformations are the optimal property for various PT applications, which drastically reduce damage and energy dissipation.

3. DFT calculations were carried out. It turned out that the instability stress plane also exists in the stress space, which demonstrates the relaibility of the MD results.

4. A nonlinear elastic model which reproduce lattice instability of Si under normal stress and shear stress correctly was developed.

5. To scale up the simulation size, parallel algorithm was developed for a CAC method which has been demonstrated to be able to reproduce phase transformation in Si. Using spatial decomposition method, the parallel efficiency reached 90% with the maximum number of processors that can be accessed, i.e., 768 from Condo at ISU. The parallel efficiency as well as the applicability of CAC in predicting dislocation-mediated plasticity in submicron-sized specimen containing billions of atoms are demonstrated.

6. Under shear, the 60^odislocation pile-up against different grain boundaries in Si induces amorphous shear band. The shear stress needed for amorphization decreases almost linearly with the number of dislocations in a pile-up.

7. The shuffle screw dislocation transmit into the neighboring grain for all GBs in silicon. The critical shear stress averaged over the whole sample for the transmission is dependent on the local structure of the GBs.

CHAPTER 1. GENERAL INTRODUCTION

1.1 Introduction

1.1.1 The interaction between phase transformation and dislocations in experiments

In many materials, phase transformation and dislocation mediated plastic deformations were observed at the same time. For example, during the polishing of the micron-sized polycrystalline Si((82))(Fig. 6.1a), the damaged region including an aSi and a damaged crystalline region ((87))(Fig. 6.1b) could be induced at a sub-micron scale. The aSi is usually on the topmost surface of the nanoscratches. The lattice in the damaged subsurface layer contains defects including dislocations, stacking faults, and slip bands(Fig. 6.1b). In the nanoscale transition region (from the amorphous layer to the crystalline layer), the Si-I grain is surrounded by aSi. There are many crystalline pockets embedded in aSi with sizes less than 5nm and even smaller((26))(Fig. 6.1c-e). However, understanding the interaction of phase transformations, plasticity, and grain structure is still unclear. Recently, Yang et al. ((31)) showed that dislocation accumulation (pileup) in silicon nanocrystals can induce the formation of amorphous phases. They found that the shear-driven amorphization occurs in a dominant shear band starting with the diamond-cubic (dc) to diamond-hexagonal (dh) phase transition and then proceeds by dislocation nucleation and accumulation in the newly formed dh-Si phase. In contrast, Wang et al. found that diamond cubic Si transforms into amorphous silicon through slip-mediated generation and storage of stacking faults, without involvng any intermediate crystalline phases ((86)).Atwater and Brown ((4)) found that amorphous silicon nucleated heterogeneously at the GBs during the irradiation of polycrystalline Si thin films. Ballin et al. ((5)) found that dislocation with a common burgers vector 1/2[011] transmitted from one grain to the neighboring grain at $\Sigma 9$ GBs using the in-situ high-voltage electron microscopy.

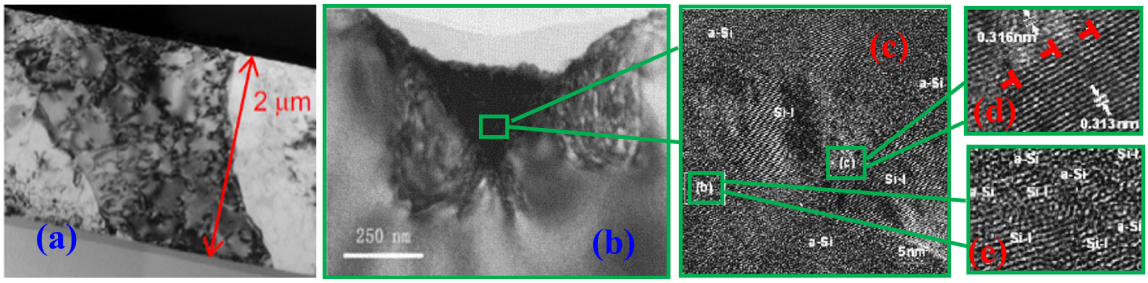

Figure 1.1 Images of multiscale microstructures of phase transformations and dislocations in polycrystalline Si. (a) TEM image of 2μm thick Si film solar cells((82)); (b) TEM image of Si under nanoscratching((87)); (c) HRTEM image of phase transformations zone((26)); (d) dislocations on the aSi/Si-I interface((26)); (e) nanocrystalline aSi/Si-I in PTs zone((26)).

1.1.2 Lattice Instability during phase transformation

Theoretically, a crystalline material in thermal equilibrium at ambient conditions has the lattice structure that minimizes the Gibbs free energy. The traditional approach ((27)) can be divided into two main criteria. The first one is that lattice instability occurs when some elastic moduli (C_{ij}) or their combinations reduce to zero and it results in various reasonable/succesful applications. This is because the elastic energy change associated with an arbitraty deformation given by small strains e_i is

$$U_{elast} = 1/2V_0 \sum_{i,j=1}^{6} C_{ij}e_ie_j + O(e^3) \tag{1}$$

V_0 is the volume of the undeformed sample. A lattice is dynamically stable only if U_{elast} is positive for any small deformation which imply that the eigenvalue of the matrix C_{ij} are positive. In cubic lattice symmetry, dynamical stability requires that

$$C_{11} + 2C_{12} > 0, C_{11} > |C_{12}|, C_{44} > 0. \tag{2}$$

The second criteria is that its frequency $\omega(\mathbf{q}, s)^2 > 0$ for all $\mathbf{q}$ and s, where $\mathbf{q}$ is the wave vector and s is a label denoting the polarization and the phonon branches. An example of this is the fcc structure of tungsten which have dynamical instabilities in large regions of $\mathbf{q}$ in the first Brillouin zone((21)).

However, (a) there are cases when instability is not related to any of these criteria; while some softening is observed, elastic moduli and phonon frequencies are still far from zero value, see ((28; 70; 23; 68; 1)). (b) There are fundamental problems with such an approach. All of the above instabilities are related to inelastic structural changes, which generate dissipation and usually require additional internal variables or order parameters for their description, which are neglected in ((32; 62; 85; 1; 56; 57; 28; 70; 23; 68)). (c) Instability can be studied under prescribed (controlled) stress tensors only, and results are different for different prescribed stresses, e.g., true Cauchy stress (force per unit actual area) or first Piola-Kirchhoff stress (force per unit undeformed area). Results are also different for different choice of the finite strains measures ((32; 62; 85)), which is practically arbitrary. In simulations of heterogeneous microstructure evolution in materials under mechanical loadings, stress components can be prescribed at boundary only and it is impossible to define, which of the stress tensors is controlled in each material point within bulk material. Consequently, such instability criteria cannot be directly applied. (d) Elastic moduli and phonon spectra should be calculated directly in atomistic simulations for each multiaxial strain state and it is practically impossible to develop a predictive analytical theory determining which combination of six components of stress tensors leads to initiation of a PT. In this work, we have applied density functional theory, molecular dynamics and continuum method to study the lattice instability of crystal phases using example from Si I phase to Si II phase.

Phase transformations (PTs) in solids are traditionally characterized by the pressure-temperature phase diagram, each line of which corresponds to thermodynamic equilibrium (79). However, actually observed PTs occur under significant deviations from the equilibrium (99; 72; 76; 7), and most first-order PT are accompanied by a hysteresis. For example, the phase equilibrium pressure for graphite-diamond in carbon at room temperature is 2.45 GPa; however, due to hysteresis, the direct PT starts at 70 GPa in experiment (72). The high-pressure superhard cubic phase of boron nitride (BN) is stable at ambient conditions (76), however, highly disordered hexagonal BN does not transform even at 52.8 GPa (7). The reason for deviation of the actual PT pressure from the equilibrium one is the enthalpy barrier. When the effect of thermal fluctuations can be neglected, e.g., at low temperature and relatively short observation time, the PT criterion is related to disappearance of the enthalpy barrier, i.e., to the lattice instability. That is why lattice instability conditions are intensively studied under hydrostatic, uniaxial and multiaxial loadings (32; 62; 85; 28; 70; 52; 53). While phase equilibrium under stress tensor can be derived within continuum thermodynamic treatment for elastic (29) and elastoplastic (46) materials, lattice instability requires a separate consideration.

In experiments, there is a significant reduction in the PT pressure due to the deviatoric (non-hydrostatic) stresses and especially plastic strains (47; 1; 7; 20; 51). For example, a large plastic shear reduced PT from highly disordered to superhard wurtzitic BN from 52.8 to 6.7 GPa (7), i.e., by an order of magnitude. This phenomenon is extremely important from both fundamental and applied points of view, because it may reduce the PT pressure for numerous high-pressure phases with unique properties to a practical level. A physical mechanism responsible for this reduction was suggested in (47). Plastic strain produces dislocation pileups. Since all stresses at the tip of a dislocation pileup are proportional to the number of dislocations in a pileup, which can be as high as 10 to 100, local stresses exceed the lattice instability limit and cause barrierless nucleation of a high-pressure phase even at relatively small external pressure. This was rationalized in (47) based on analytical model and in (54; 35) using phase field approach. However, input in the phase field model – PT (instability) criteria for direct and reverse PTs for an ideal crystal under *general*

stress tensor – was assumed hypothetically because such criteria are not known for any material. In addition, for many materials there is a significant difference between calculated instability pressure (e.g., 64-80 GPa for Si I→Si II PT (63; 23)) and experimentally determined PT pressure (e.g., 9-12 GPa for the same PT (19)). This reduction was qualitatively explained by presence of the local stress concentrators around defects (dislocations, grain boundaries, etc.) and the effect of the nonhydrostatic stresses. Quantitative solution of this problem requires knowledge of the lattice instability conditions under stress tensor, similar to the previous problem.

1.1.3 Current State of Multiscale Modelling

Multiscale modelling methods can be divided into sequential and concurrent methods. In sepuential methods, MD simulations are deployed to calibrate the constitutive models and parameters for higher order models. For example, to simulate material plasicity, information about dislocation nucleation, the strength of dislocation junctions, dislocation mobility, and dislocation interactions from atomistic modelling are used to develop short-range interaction rules. These rules are then feed into continuum-level models such as dislocation dynamics((3; 2; 81)). One major challenge of such sequential approach is how to average the fine scale information and how to input the averaged information into the higher scale models. In contrast, concurrent methods directly combine a fine-scale description of materials with a higher order material description within one computer model((10; 12; 103; 83; 88; 40)). Examples of such concurrent methods for multiscale plasticity include the coupled atomistic and discrete dislocation formulation((73; 74; 75; 59)), coupled discrete dislocation and continuum crystal plasticity((84)), and the multiresolution molecular mechanics((7)). A comprehensive review of concurrent multiscale methods can be found in Refs. ((60; 61)).

A direct combination of a fine-scale model, e.g., MD, with a higher order model, such as finite element (FE), within one computational framework introduces an unrealistic numerical interface into the computational model. Due to the mismatch of material descriptions between MD and FE, an atomistic/continuum interface needs to be constructed through a careful numerical implemen-

tation. Most of the efforts are then devoted to construct such numerical interface by matching or bridging the atomistic and continuum descriptions sush that defects can pass from MD to FE. Different from other concurrent multiscale methods which directly combines MD and FE, the recently developed concurrent atomistic-continuum (CAC) method is based on a new atomistic field formalism that unifies the atomistic and continuum description of materials within one theoretical framework((91)). The coarse-grained (CG) domain in CAC admits dislocation nucleation and migration on the boundaries within the gaps between elements without the need of adaptive mesh refinement((93)). CAC has been successfully applied to simulate a variety of material behaviors, such as slip transfer of dislocations across grain boundaries((95)), dislocations bowing out from Frank-Read sources((94)), dislocation-void interaction((92)), dislocations and fracture in strontium titante((97; 96)), dynamics crack propagation((18)), fast moving dislocations((90)), and phonon dynamics in a 1-D polyatomic chain((89)). It is noted that, because the original version of the CAC simulator was not massively parallelized, those applications were mainly limited to material behavior from the atomistic to the nanoscale.

1.1.3.1 A brief review of the CAC method

The theoretical foundation of CAC is an atomistic field formalism proposed by Chen((15; 16)), in which a crystalline material is viewed as a continuous collection of lattice points, while embedded within each point is a unit cell containing a group of discrete atoms((16)). Chen((16)) defined the continuum-level physical quantities from the atomic scale and formulated the microscopic balance equations of the physical quantities including mass density, linear momentum density, and the internal energy density.

It is noted that, the continuum description of those physical quanties is by means of continuous functions in terms of x and t in the physical space. Microscopic dynamic quantities in classical N-body dynamics, on the other hand, are functions of (r,p),i.e., the positions and momenta of atoms, in phase space:

$$\mathbf{r} = \{\mathbf{R}^k, k = 1, 2, 3..., n\} \tag{3}$$

$$\mathbf{p} = \{\mathbf{m}^k\mathbf{V}^k, k = 1, 2, 3...n\} \tag{4}$$

where $\mathbf{R^k}$ is the position vector and $\mathbf{V^k}$ is the velocity of the kth atom, m^k is the atomic mass, and n is the total number of atoms in the system. In the atomistic field formalism, the quantities in the phase space and the physical space descriptions can be linked through utilizing the localization function $\delta((16))$, i.e.,

$$\rho(\mathbf{x}) = \sum_{k=1}^{n} \delta(\mathbf{R}^k - x) \tag{5}$$

$$\rho(\mathbf{x})\mathbf{v}(\mathbf{x}) = \sum_{k=1}^{n} m^k V^k \delta(\mathbf{R^k} - \mathbf{x}) \tag{6}$$

where ρ is the microscopic local mass density and $\rho\mathbf{v}$ is the momentum density in physical coordinate. Taking the time derivatives of Eqs. 6, Chen ((16)) formulated the microscopic balance equations of the mass and linear momentum. In particular, for a monoatomic crystal under no external forces, the balance equation of linear momentum can be re-written as ((16))

$$\rho\ddot{\mathbf{x}} = \mathbf{f}_{int}(\mathbf{x}) \tag{7}$$

where

$$\mathbf{f}_{int} = \sum_{k=1} n \sum_{i} \delta(\mathbf{R}^k - x)\mathbf{F}_{ik} \tag{8}$$

is the internal force density, F_{ik} is the atomic force acting on atom k by atom i and δ is a Dirac δ-function.

It is daunting to directly compute F_{ik} for all the atomic pairs. Thus, one critical step in numerical implementation of the atomistic field formalism is to efficiently and accurately calculate

the internal force density $\mathbf{f}_{int}$ in equation (8). Xiong et al. ((91)) performed a FE implementation of the atomistic field formalism and the numerical procedure was coined as CAC, which discretizes the computational domain into piecewise elements. Gaussian quadrature was deployed to perform the spatial integration to calculate the internal force density((91)). Later, Yang et al. ((97)) and Xu et al. ((93)) modified the quadrature rules and demonstrated that the generalized stacking fault energy, core structure and the stress field around a mixed dislocation in CAC models are comparable with that from MD. In implementation, the computational domain is discretized into piecewise elements. Each element is in a rhombohedral shape and contains a collection of lattice cells. The displacement within the element is approximated by

$$\mathbf{u} = \Phi_\xi(\mathbf{x})\mathbf{U}_\xi \tag{9}$$

where $\mathbf{U}_\xi$ are finite element nodal displacements, $\Phi_\xi(\mathbf{x})$ is the standard tri-linear shape function. In the numerical integration scheme, the internal force on node ξ is calculated as follows((93)):

$$f_{int}^{\xi} = \frac{\sum_\mu \omega_\mu \Phi_{\xi\mu} F_\mu}{\sum_\mu \omega_\mu \Phi_{\xi\mu}} \tag{10}$$

where F^μ is the force on the integration point μ, ω_μ is the weight, and $\Phi_{\xi\mu}$ is the value of the shape function Φ_ξ at the integration point μ. The weight ω_μ is determined by the number of atoms that integration point represents. In detail, for those integration points located on nodal sites, $\omega_\mu = 1$; for those on the element edges, $\omega_\mu = N_l - 2$; for those on the surface, $\omega_\mu = (N_l - 2)^2$; and for those within the interior of the elements, $\omega_\mu = (N_l - 2)^3$. Here, N_l is the number of atoms along the edge of each coarse element. It is clear that the CAC model will degenerate into full MD simulations when $N_l = 2$ and $\mu = 8$. Such an atomic-scale mesh is referred as the finest mesh in CAC method and will function as a fully atomistic domain.

Bibliography

[1] Alippi, P., Marcus, P., and Scheffler, M. (1997). Strained tetragonal states and bain paths in metals. *Physical review letters*, 78(20):3892.

[2] Amodeo, R. and Ghoniem, N. (1990a). Dislocation dynamics. ii. applications to the formation of persistent slip bands, planar arrays, and dislocation cells. *Physical Review B*, 41(10):6968.

[3] Amodeo, R. J. and Ghoniem, N. M. (1990b). Dislocation dynamics. i. a proposed methodology for deformation micromechanics. *Physical Review B*, 41(10):6958.

[4] Atwater, H. A. and Brown, W. L. (1990). Grain boundary mediated amorphization in silicon during ion irradiation. *Applied Physics Letters*, 56(1):30–32.

[5] Baillin, X., Pelissier, J., Bacmann, J., Jacques, A., and George, A. (1987). Dislocation transmission through= 9 symmetrical tilt boundaries in silicon and germanium: I. in situ observations by synchrotron x-ray topography and high-voltage electron microscopy. *Philosophical Magazine A*, 55(2):143–164.

[23] Balamane, H., Halicioglu, T., and Tiller, W. (1992). Comparative study of silicon empirical interatomic potentials. *Physical Review B*, 46(4):2250.

[7] Biyikli, E. and To, A. C. (2017). Multiresolution molecular mechanics: Implementation and efficiency. *Journal of Computational Physics*, 328:27–45.

[1] Blank, V. D. and Estrin, E. I. (2013). *Phase transitions in solids under high pressure*. CRC Press.

[9] Blöchl, P. E. (1994). Projector augmented-wave method. *Physical review B*, 50(24):17953.

[10] Broughton, J. Q., Abraham, F. F., Bernstein, N., and Kaxiras, E. (1999). Concurrent coupling of length scales: methodology and application. *Physical review B*, 60(4):2391.

[14] Cai, W., Bulatov, V. V., Chang, J., Li, J., and Yip, S. (2004). Dislocation core effects on mobility. *Dislocations in solids*, 12:1–80.

[12] Cai, W., de Koning, M., Bulatov, V. V., and Yip, S. (2000). Minimizing boundary reflections in coupled-domain simulations. *Physical Review Letters*, 85(15):3213.

[13] Černỳ, M., Řehák, P., Umeno, Y., and Pokluda, J. (2012). Stability and strength of covalent crystals under uniaxial and triaxial loading from first principles. *Journal of Physics: Condensed Matter*, 25(3):035401.

[6] Chen, X., Xiong, L., Chernatynskiy, A., and Chen, Y. (2014). A molecular dynamics study of tilt grain boundary resistance to slip and heat transfer in nanocrystalline silicon. *Journal of Applied Physics*, 116(24):244309.

[15] Chen, Y. (2006). Local stress and heat flux in atomistic systems involving three-body forces. *The Journal of chemical physics*, 124(5):054113.

[16] Chen, Y. (2009). Reformulation of microscopic balance equations for multiscale materials modeling. *The Journal of chemical physics*, 130(13):134706.

[17] Deb, S. K., Wilding, M., Somayazulu, M., and McMillan, P. F. (2001). Pressure-induced amorphization and an amorphous–amorphous transition in densified porous silicon. *Nature*, 414(6863):528.

[18] Deng, Q. and Chen, Y. (2013). A coarse-grained atomistic method for 3d dynamic fracture simulation. *International Journal for Multiscale Computational Engineering*, 11(3).

[19] Domnich, V., Ge, D., and Gogotsi, Y. (2004). Indentation-induced phase transformations in semiconductors. *High Pressure Surface Science and Engineering*, pages 381–442.

[20] Edalati, K. and Horita, Z. (2016). A review on high-pressure torsion (hpt) from 1935 to 1988. *Materials Science and Engineering: A*, 652:325–352.

[21] Einarsdotter, K., Sadigh, B., Grimvall, G., and Ozoliņš, V. (1997). Phonon instabilities in fcc and bcc tungsten. *Physical review letters*, 79(11):2073.

[22] Elliott, R. S., Triantafyllidis, N., and Shaw, J. A. (2011). Reversible stress-induced martensitic phase transformations in a bi-atomic crystal. *Journal of the Mechanics and Physics of Solids*, 59(2):216–236.

[23] Gaál-Nagy, K., Schmitt, M., Pavone, P., and Strauch, D. (2001a). Ab initio study of the high-pressure phase transition from the cubic-diamond to the β-tin structure of si. *Computational materials science*, 22(1-2):49–55.

[24] Gaál-Nagy, K., Schmitt, M., Pavone, P., and Strauch, D. (2001b). Ab initio study of the high-pressure phase transition from the cubic-diamond to the β-tin structure of si. *Computational materials science*, 22(1-2):49–55.

[25] Gaál-Nagy, K. and Strauch, D. (2006). Phonons in the β-tin, i m m a, and sh phases of silicon from ab initio calculations. *Physical Review B*, 73(1):014117.

[26] Ge, D., Domnich, V., and Gogotsi, Y. (2003). High-resolution transmission electron microscopy study of metastable silicon phases produced by nanoindentation. *Journal of applied physics*, 93(5):2418–2423.

[27] Grimvall, G., Magyari-Köpe, B., Ozoliņš, V., and Persson, K. A. (2012a). Lattice instabilities in metallic elements. *Reviews of Modern Physics*, 84(2):945.

[28] Grimvall, G., Magyari-Köpe, B., Ozoliņš, V., and Persson, K. A. (2012b). Lattice instabilities in metallic elements. *Reviews of Modern Physics*, 84(2):945.

[29] Grinfeld, M. (1991). *Thermodynamic Methods in the Theory of Heterogeneus Systems*. Longman Scientific and Technical.

[26] Hahn, E., Zhao, S., Bringa, E., and Meyers, M. (2016). Supersonic dislocation bursts in silicon. *Scientific reports*, 6:26977.

[31] He, Y., Zhong, L., Fan, F., Wang, C., Zhu, T., and Mao, S. X. (2016). In situ observation of shear-driven amorphization in silicon crystals. *Nature nanotechnology*.

[32] Hill, R. and Milstein, F. (1977). Principles of stability analysis of ideal crystals. *Physical Review B*, 15(6):3087.

[15] Hull, D. and Bacon, D. J. (2001). *Introduction to dislocations*. Butterworth-Heinemann.

[10] Javanbakht, M. and Levitas, V. I. (2016a). Phase field approach to dislocation evolution at large strains: Computational aspects. *International Journal of Solids and Structures*, 82:95–110.

[35] Javanbakht, M. and Levitas, V. I. (2016b). Phase field simulations of plastic strain-induced phase transformations under high pressure and large shear. *Physical Review B*, 94(21):214104.

[7] Ji, C., Levitas, V. I., Zhu, H., Chaudhuri, J., Marathe, A., and Ma, Y. (2012). Shear-induced phase transition of nanocrystalline hexagonal boron nitride to wurtzitic structure at room temperature and lower pressure. *Proceedings of the National Academy of Sciences*, 109(47):19108–19112.

[8] Jin, Z.-H., Gumbsch, P., Albe, K., Ma, E., Lu, K., Gleiter, H., and Hahn, H. (2008). Interactions between non-screw lattice dislocations and coherent twin boundaries in face-centered cubic metals. *Acta Materialia*, 56(5):1126–1135.

[7] Jin, Z.-H., Gumbsch, P., Ma, E., Albe, K., Lu, K., Hahn, H., and Gleiter, H. (2006). The interaction mechanism of screw dislocations with coherent twin boundaries in different face-centred cubic metals. *Scripta Materialia*, 54(6):1163–1168.

[39] Johnson, D. D. (1988). Modified broydens method for accelerating convergence in self-consistent calculations. *Physical Review B*, 38(18):12807.

[40] Klein, P. A. and Zimmerman, J. A. (2006). Coupled atomistic–continuum simulations using arbitrary overlapping domains. *Journal of Computational Physics*, 213(1):86–116.

[12] Kohyama, M., Yamamoto, R., and Doyama, M. (1986). Structures and energies of symmetrical¡ 011¿ tilt grain boundaries in silicon. *physica status solidi (b)*, 137(1):11–20.

[42] Kresse, G. and Furthmüller, J. (1996). Efficiency of ab-initio total energy calculations for metals and semiconductors using a plane-wave basis set. *Computational materials science*, 6(1):15–50.

[43] Kresse, G. and Hafner, J. (1993). Ab initio molecular dynamics for liquid metals. *Physical Review B*, 47(1):558.

[44] Kresse, G. and Hafner, J. (1994). Ab initio molecular-dynamics simulation of the liquid-metal–amorphous-semiconductor transition in germanium. *Physical Review B*, 49(20):14251.

[45] Kresse, G. and Joubert, D. (1999). From ultrasoft pseudopotentials to the projector augmented-wave method. *Physical Review B*, 59(3):1758.

[46] Levitas, V. I. (1998). Thermomechanical theory of martensitic phase transformations in inelastic materials. *International Journal of Solids and Structures*, 35(9-10):889–940.

[47] Levitas, V. I. (2004). High-pressure mechanochemistry: conceptual multiscale theory and interpretation of experiments. *Physical Review B*, 70(18):184118.

[48] Levitas, V. I. (2005). Crystal-amorphous and crystal-crystal phase transformations via virtual melting. *Physical review letters*, 95(7):075701.

[49] Levitas, V. I. (2013). Phase-field theory for martensitic phase transformations at large strains. *International Journal of Plasticity*, 49:85–118.

[50] Levitas, V. I. (2017). Elastic model for stress–tensor-induced martensitic transformation and lattice instability in silicon under large strains. *Materials Research Letters*, 5(8):554–561.

[51] Levitas, V. I. (2018). High pressure phase transformations revisited. *Journal of Physics: Condensed Matter*, 30(16):163001.

[52] Levitas, V. I., Chen, H., and Xiong, L. (2017a). Lattice instability during phase transformations under multiaxial stress: Modified transformation work criterion. *Physical Review B*, 96(5):054118.

[53] Levitas, V. I., Chen, H., and Xiong, L. (2017b). Triaxial-stress-induced homogeneous hysteresis-free first-order phase transformations with stable intermediate phases. *Physical review letters*, 118(2):025701.

[54] Levitas, V. I. and Javanbakht, M. (2014a). Phase transformations in nanograin materials under high pressure and plastic shear: nanoscale mechanisms. *Nanoscale*, 6(1):162–166.

[9] Levitas, V. I. and Javanbakht, M. (2014b). Phase transformations in nanograin materials under high pressure and plastic shear: nanoscale mechanisms. *Nanoscale*, 6(1):162–166.

[56] Li, J., Van Vliet, K. J., Zhu, T., Yip, S., and Suresh, S. (2002). Atomistic mechanisms governing elastic limit and incipient plasticity in crystals. *Nature*, 418(6895):307.

[57] Li, J., Zhu, T., Yip, S., Van Vliet, K. J., and Suresh, S. (2004). Elastic criterion for dislocation nucleation. *Materials Science and Engineering: A*, 365(1-2):25–30.

[3] Martinez-Hernandez, M., Kirchner, H., Korner, A., George, A., and Michel, J. (1987). Dislocations at grain boundaries in deformed silicon. *Philosophical Magazine A*, 56(5):641–658.

[59] Miller, R. E., Shilkrot, L., and Curtin, W. A. (2004). A coupled atomistics and discrete dislocation plasticity simulation of nanoindentation into single crystal thin films. *Acta Materialia*, 52(2):271–284.

[60] Miller, R. E. and Tadmor, E. B. (2007). Hybrid continuum mechanics and atomistic methods for simulating materials deformation and failure. *MRS bulletin*, 32(11):920–926.

[61] Miller, R. E. and Tadmor, E. B. (2009). A unified framework and performance benchmark of fourteen multiscale atomistic/continuum coupling methods. *Modelling and Simulation in Materials Science and Engineering*, 17(5):053001.

[62] Milstein, F., Marschall, J., and Fang, H. E. (1995). Theoretical bcc fcc transitions in metals via bifurcations under uniaxial load. *Physical review letters*, 74(15):2977.

[63] Mizushima, K., Yip, S., and Kaxiras, E. (1994). Ideal crystal stability and pressure-induced phase transition in silicon. *Physical Review B*, 50(20):14952.

[64] Monkhorst, H. J. and Pack, J. D. (1976). Special points for brillouin-zone integrations. *Physical review B*, 13(12):5188.

[65] Patten, J. (2004). Ductile regime machining of semiconductors and ceramics. *High Pressure Surface Science and Engineering*.

[66] Perdew, J. P., Burke, K., and Ernzerhof, M. (1996). Generalized gradient approximation made simple. *Physical review letters*, 77(18):3865.

[17] Pizzagalli, L., Godet, J., Guénolé, J., Brochard, S., Holmstrom, E., Nordlund, K., and Albaret, T. (2013). A new parametrization of the stillinger–weber potential for an improved description of defects and plasticity of silicon. *Journal of Physics: Condensed Matter*, 25(5):055801.

[68] Planes, A. and Mañosa, L. (2001). Vibrational properties of shape-memory alloys. In *Solid state physics*, volume 55, pages 159–267. Elsevier.

[18] Plimpton, S. (1995). Fast parallel algorithms for short-range molecular dynamics. *Journal of computational physics*, 117(1):1–19.

[70] Pokluda, J., Černỳ, M., Šob, M., and Umeno, Y. (2015). Ab initio calculations of mechanical properties: Methods and applications. *Progress in Materials Science*, 73:127–158.

[13] Ratanaphan, S., Yoon, Y., and Rohrer, G. S. (2014). The five parameter grain boundary character distribution of polycrystalline silicon. *Journal of materials science*, 49(14):4938–4945.

[72] Schindler, T. and Vohra, Y. K. (1995). A micro-raman investigation of high-pressure quenched graphite. *Journal of Physics: Condensed Matter*, 7(47):L637.

[73] Shilkrot, L., Curtin, W. A., and Miller, R. E. (2002a). A coupled atomistic/continuum model of defects in solids. *Journal of the Mechanics and Physics of Solids*, 50(10):2085–2106.

[74] Shilkrot, L., Miller, R., and Curtin, W. (2002b). Coupled atomistic and discrete dislocation plasticity. *Physical review letters*, 89(2):025501.

[75] Shilkrot, L., Miller, R. E., and Curtin, W. A. (2004). Multiscale plasticity modeling: coupled atomistics and discrete dislocation mechanics. *Journal of the Mechanics and Physics of Solids*, 52(4):755–787.

[76] Solozhenko, V. L. (1995). Boron nitride phase diagram. state of the art. *International Journal of High Pressure Research*, 13(4):199–214.

[19] Stukowski, A. (2009). Visualization and analysis of atomistic simulation data with ovito–the open visualization tool. *Modelling and Simulation in Materials Science and Engineering*, 18(1):015012.

[78] Telyatnik, R., Osipov, A., and Kukushkin, S. (2016). Ab initio modelling of nonlinear elasto-plastic properties of diamond-like c, sic, si, ge crystals upon large strains. *Materials Physics & Mechanics*, 29(1).

[79] Tonkov, E. Y. and Ponyatovsky, E. (2004). *Phase transformations of elements under high pressure*, volume 4. CRC press.

[80] Umeno, Y. and Černỳ, M. (2008). Effect of normal stress on the ideal shear strength in covalent crystals. *Physical Review B*, 77(10):100101.

[81] Van der Giessen, E. and Needleman, A. (1995). Discrete dislocation plasticity: a simple planar model. *Modelling and Simulation in Materials Science and Engineering*, 3(5):689.

[82] Varlamov, S., Dore, J., Evans, R., Ong, D., Eggleston, B., Kunz, O., Schubert, U., Young, T., Huang, J., Soderstrom, T., et al. (2013). Polycrystalline silicon on glass thin-film solar cells: A

transition from solid-phase to liquid-phase crystallised silicon. *Solar Energy Materials and Solar Cells*, 119:246–255.

[83] Wagner, G. J. and Liu, W. K. (2003). Coupling of atomistic and continuum simulations using a bridging scale decomposition. *Journal of Computational Physics*, 190(1):249–274.

[84] Wallin, M., Curtin, W., Ristinmaa, M., and Needleman, A. (2008). Multi-scale plasticity modeling: Coupled discrete dislocation and continuum crystal plasticity. *Journal of the Mechanics and Physics of Solids*, 56(11):3167–3180.

[85] Wang, J., Yip, S., Phillpot, S., and Wolf, D. (1993). Crystal instabilities at finite strain. *Physical Review Letters*, 71(25):4182.

[86] Wang, Y.-C., Zhang, W., Wang, L.-Y., Zhuang, Z., Ma, E., Li, J., and Shan, Z.-W. (2016). In situ tem study of deformation-induced crystalline-to-amorphous transition in silicon. *NPG Asia Materials*, 8(7):e291.

[87] Wu, Y., Huang, H., Zou, J., and Dell, J. (2009). Nanoscratch-induced deformation of single crystal silicon. *Journal of Vacuum Science & Technology B: Microelectronics and Nanometer Structures Processing, Measurement, and Phenomena*, 27(3):1374–1377.

[88] Xiao, S. and Belytschko, T. (2004). A bridging domain method for coupling continua with molecular dynamics. *Computer methods in applied mechanics and engineering*, 193(17-20):1645–1669.

[89] Xiong, L., Chen, X., Zhang, N., McDowell, D. L., and Chen, Y. (2014). Prediction of phonon properties of 1d polyatomic systems using concurrent atomistic–continuum simulation. *Archive of Applied Mechanics*, 84(9-11):1665–1675.

[90] Xiong, L., Rigelesaiyin, J., Chen, X., Xu, S., McDowell, D. L., and Chen, Y. (2016). Coarse-grained elastodynamics of fast moving dislocations. *Acta Materialia*, 104:143–155.

[91] Xiong, L., Tucker, G., McDowell, D. L., and Chen, Y. (2011). Coarse-grained atomistic simulation of dislocations. *Journal of the Mechanics and Physics of Solids*, 59(2):160–177.

[92] Xiong, L., Xu, S., McDowell, D. L., and Chen, Y. (2015). Concurrent atomistic–continuum simulations of dislocation–void interactions in fcc crystals. *International Journal of Plasticity*, 65:33–42.

[93] Xu, S., Che, R., Xiong, L., Chen, Y., and McDowell, D. L. (2015). A quasistatic implementation of the concurrent atomistic-continuum method for fcc crystals. *International Journal of Plasticity*, 72:91–126.

[94] Xu, S., Xiong, L., Chen, Y., and McDowell, D. L. (2016a). An analysis of key characteristics of the frank-read source process in fcc metals. *Journal of the Mechanics and Physics of Solids*, 96:460–476.

[95] Xu, S., Xiong, L., Chen, Y., and McDowell, D. L. (2016b). Sequential slip transfer of mixed-character dislocations across $\sigma 3$ coherent twin boundary in fcc metals: a concurrent atomistic-continuum study. *npj Computational Materials*, 2:15016.

[96] Yang, S. and Chen, Y. (2015). Concurrent atomistic and continuum simulation of bi-crystal strontium titanate with tilt grain boundary. *Proc. R. Soc. A*, 471(2175):20140758.

[97] Yang, S., Xiong, L., Deng, Q., and Chen, Y. (2013). Concurrent atomistic and continuum simulation of strontium titanate. *Acta Materialia*, 61(1):89–102.

[98] Yim, W. and Paff, R. (1974). Thermal expansion of aln, sapphire, and silicon. *Journal of Applied Physics*, 45(3):1456–1457.

[99] Zarkevich, N. A. and Johnson, D. D. (2015a). Coexistence pressure for a martensitic transformation from theory and experiment: Revisiting the bcc-hcp transition of iron under pressure. *Phys. Rev. B*, 91:174104.

[100] Zarkevich, N. A. and Johnson, D. D. (2015b). Magneto-structural transformations via a solid-state nudged elastic band method: Application to iron under pressure. *J. Chem. Phys.*, 143(6):064707.

[101] Zarkevich, N. A. and Johnson, D. D. (2015c). Nudged-elastic band method with two climbing images: finding transition states in complex energy landscapes. *The Journal of chemical physics*, 142(2):024106.

[102] Zarkevich, N. A., Levitas, V. I., Chen, H., and Johnson, D. D. (2018). *to be published*.

[103] Zhou, M. and McDowell, D. L. (2002). Equivalent continuum for dynamically deforming atomistic particle systems. *Philosophical Magazine A*, 82(13):2547–2574.

CHAPTER 2. LATTICE INSTABILITY DURING PHASE TRANSFORMATIONS UNDER MULTIAXIAL STRESS: MODIFIED TRANSFORMATION WORK CRITERION

Reproduced from: 'Levitas, Valery I., Hao Chen, and Liming Xiong. Lattice instability during phase transformations under multiaxial stress: modified transformation work criterion. Physical Review B 96.5 (2017): 054118.'

2.1 Introduction

Between two crystalline phases, melting, amorphization, fracture, twinning, and dislocation nucleation. The traditional approach (32; 62; 85; 1; 56; 57; 7; 28; 70) (coined below as zero-moduli condition) states that lattice instability occurs when some elastic moduli or their combinations reduce to zero and it results in various reasonable/succesful applications. For multilattices, relative shift vectors are included in instability criteria along with shear moduli within the same description (7; 22; 28; 70). In addition, phonon stability (soft-mode) criteria (7; 22; 56; 57; 28; 70) were applied, which for the long wavelength limit should coincide with zero-moduli criteria, but also give additional conditions for short wavelength. However,

(a) there are many cases when instability is not related to any of these criteria; while some softening is observed, elastic moduli and phonon frequencies are still far from zero value, see (28; 70; 23; 68; 1).

(b) There are also fundamental problems with the zero-moduli approach. All of the above instabilities are related to inelastic structural changes, which generate dissipation and usually require additional internal variables or order parameters for their description, which are neglected in (7; 32; 62; 85; 1; 56; 57; 28; 70; 22; 23; 68).

(c) Instability can be studied under prescribed (controlled) stress tensors, and results are different for different prescribed stresses, e.g., true Cauchy stress (force per unit actual area) or first Piola-Kirchhoff stress (force per unit undeformed area). Results are also different for different choice of the finite strains measures (32; 62; 85), which is practically arbitrary. In simulations of heterogeneous microstructure evolution in materials under mechanical loadings, stress components can be prescribed at boundary only and it is impossible to define, which of the stress tensors is controlled in each material point within bulk material. Consequently, such instability criteria cannot be directly applied in continuum simulations.

(d) Elastic moduli and phonon spectra should be calculated directly in atomistic simulations for each multiaxial strain state and it is practically impossible to develop a predictive analytical theory determining which combination of six components of stress tensors leads to initiation of a PT.

Here, we developed a conceptually novel approach to predict lattice instability during crystal-crystal PTs and confirmed/specified the formalism for direct and reverse PTs between Si I and Si II phases using MD simulations.

(a) This approach includes an order parameter η describing the entire transformation process (like in Landau-type theory for PTs) and instability criterion is strictly derived utilizing the second law of thermodynamics.

(b) This criterion is independent of the prescribed stress tensor measure and is confirmed by MD simulations.

(c) The instability criterion for both direct and reverse PTs is derived and found to be corresponding to the critical value of the modified transformation work; the criterion can be calibrated by MD simulations for Si at two different stress states; then the criterion describes hundreds of MD simulations for silicon under various combinations of triaxial normal stresses and shear stresses.

(d) The effect of all three shear stresses along cubic axes on the lattice instability of Si I is found to be negligible in atomistic simulations, in agrement with our criterion.

(e) While jumps in elastic moduli during PT contribute to the general theory and can be used as additional degrees of freedom to improve correspondence between theory and MD results, simulations show that their contribution is negligible.

(f) Good correspondence between theory and simulations is obtained only for the case when local theory takes into account a geometrically nonlinear term contributing to interfacial stresses for general heterogeneous solutions, which was traditionally neglected in the Landau-type theory. This, however, does not mean that interfaces or interface stresses affect our criterion, because it is formulated for homogeneous states.

(g) For PT Si I→Si II, instability also corresponds to zero elastic modulus when the Cauchy stress is prescribed, i.e., known results when one of the traditional criteria is predictive may be consistent with our criterion as well. However, for the reverse PT, Si II→Si I, the traditional approach is not applicable while our criterion still holds.

(h) Comparison of theoretical and MD results leads to a significant advancement of the generalized Landau theory in terms of unexpected dependence of transformation strain and free energy on the order parameter.

Tensors will be designated with boldface symbols; contractions of tensors $A = \{A_{ij}\}$ and $B = \{B_{ji}\}$ over one and two indices is designated as $A{\cdot}B = \{A_{ij}\, B_{jk}\}$ and $A{:}B = A_{ij}\, B_{ji}$. Symbol $:=$ means equal by definition; I is the unit tensor; and the transpose of A is A^T.

2.2 Lattice instability crterion

Similar to the previous works (32; 62; 85; 1; 56; 57; 7; 28; 70; 22) and thermodynamic textbooks, we are looking for instability criterion for homogenously stressed material under homogeneous infinitesimal fluctuations, i.e., instability of the local constitutive equations. After this criterion is satisfied, material transforms to the alternative phase either homogeneously or, if heterogeneous perturbations are present (due to thermal fluctuation or numerical errors in continuum approaches), heterogeneously, see Fig. 6.1, supplementary figures and movies. However, transformation process

that occurs after instability criterion is met does not affect the criterion itself, i.e., the instability criterion does not contain any information about any heterogeneities and interfaces.

Let $U_t = I + \bar{\varepsilon_t}$ be the transformation deformation gradient that transforms the crystal lattice of the parent phase 1 into the crystal lattice of the product phase 2 when both are under stress-free conditions. We decompose $\bar{\varepsilon_t}$ into spherical ε_{0t} and deviatoric e_t parts, $\varepsilon_t = 1/3\bar{\varepsilon}_{0t}I + e_t$. The order parameter η encodes the transformation process: for (meta)stable phases $\eta = \hat{\eta}$, where $\hat{\eta} = 0$ for phase 1 or $\hat{\eta} = 1$ for phase 2. The multiplicative decomposition of the deformation gradient $F = F_e \cdot U_t$ into elastic F_e and transformational U_t contributions will be used. The Landau-type theory for PTs under large strains, which includes formulation of lattice instability conditions under spontaneous variations of the order parameters, was developed in (49) but without allowing for interfacial stresses. Generalization for the case with interfacial stresses was completed in (11) but without the consideration of the instability conditions. Here we will generalize the instability criteria in (49) for the case with interfacial stresses using the same steps as in (49); we demonstrate that despite the fact that we consider homogeneous states here, modification in the local Helmholtz energy per unit initial volume ψ required for allowing the interface stresses is important for a formulation of the final instability criterion. Then, we specify and validate these criteria utilizing MD simulations.

Using the first and second laws of thermodynamics, the dissipation rate due to phase transformation can be derived in the form (49)

$$D = X\dot{\eta} \geq 0; \qquad X := P^T \cdot F_e : \frac{\partial U_t(\eta)}{\partial \eta} - \frac{\partial \psi(E_e, \theta, \eta)}{\partial \eta}, \tag{1}$$

where X is the thermodynamic force for change in η, $E_e = 0.5(F_e^T \cdot F_e - I)$ is the Lagrangian elastic strain, and θ is the temperature. Determination of η-dependence of U_t and ψ is one of the main problems in formulation of the Landau-type theories. These dependences should satisfy the constraint that $X = 0$ for $\eta = \hat{\eta}$ for any stress P, temperature θ, and elastic deformation gradient F_e; otherwise, equilibrium phases will not correspond to $\eta = 0$ and $\eta = 1$. We prescribe the first nonsymmetric Piola-Kirchoff stress P and suggest the following thermodynamic definition of the lattice instability:

if a spontaneous deviation of the order parameter $\Delta\eta$ from the thermodynamic equilibrium values $\hat{\eta}$ is thermodynamically admissible, i.e., dissipation rate $D \geq 0$, then the thermodynamic equilibrium is unstable. Such a definition results in the following instability condition :

$$\frac{\partial X\left(P, F_e, \hat{\eta}\right)}{\partial \eta} = P^T \cdot F_e : \frac{\partial^2 U_t(\hat{\eta})}{\partial \eta^2} - \frac{\partial^2 \psi\left(E_e, \hat{\eta}\right)}{\partial \eta^2} \geq 0, \tag{2}$$

where $\hat{\eta} = 0$ corresponds to criterion for $1 \rightarrow 2$ PT and $\hat{\eta} = 1$ is for criterion for $2 \rightarrow 1$ PT. It is proven that *the same PT criterion (2) is valid independent of the change of the prescribe stress measure*, in particular, for the prescribed Cauchy stress,

In the coordinate system related to the cubic lattice, the variable transformation deformation gradient that describes the transformation process $1 \leftrightarrow 2$ is $U_t(\eta) = I + \varepsilon_t(\eta)$ with

$$\varepsilon_t(\eta) = 1/3\varepsilon_{0t}\varphi(a_1, \eta)I + e_t\varphi(a_2, \eta); \qquad \varphi(a, \eta) := a\eta^2(1-\eta)^2 + (4\eta^3 - 3\eta^4), \tag{3}$$

where a_i are the material parameters. Traditionally (49; 11), $a_1 = a_2$ and all components of transformation strain change proportionally during PT, which was a strong assumption. To describe MD results, we need to use *different parameters for spherical and deviatoric transformation strain.* The Helmholtz free energy per unit mass is accepted in the form (11):

$$\psi(E_e, \eta, \theta) = \psi^e(F_e, \eta, \theta) + J\breve{\psi}^\theta(\theta, \eta) + \tilde{\psi}^\theta(\theta, \eta); \quad J = detF. \tag{4}$$

Here, $J = detF$, ψ^e is the elastic energy; $\breve{\psi}^\theta = A(\theta)\eta^2(1-\eta)^2$ is the double-well barrier; $\tilde{\psi}^\theta = \Delta G^\theta(\theta)\eta^3(4-3\eta)$ is the part of the thermal energy proportional to the difference between the thermal parts of the energies of phases 2 and 1, $\Delta G^\theta 244$. It is justified in (11) that for correct introduction of the interfacial stresses in the Ginzburg-Landau theory for an interface between two phases, along with modifications in the gradient energy, the local double-well barrier $\breve{\psi}^\theta$ should be also multiplied by J. Thus, while we consider homogeneous states and interfaces are not present, still we have the term J, which is required for consistent interfacial stresses for heterogeneous states. This should not be surprising, because for two phase states $\breve{\psi}^\theta$ is localized at the interfaces, i.e., where $0 < \eta < 1$, and is zero in the bulk, where $\eta = 0$ or 1. While for homogeneous stable states $\eta = 0$ or 1 and $\breve{\psi}^\theta = 0$, the second derivative of $\breve{\psi}^\theta$ at $\eta = 0$ or 1 is not zero, which makes contribution to the instability conditions.

Substituting Eqs.(3) and (4) along with relationship $P = J\sigma{\cdot}F^{T^{-1}}$ in criterion (2), we obtain

$$W := \sigma{:}F_e^{T-1} \cdot U_t^{-1} \cdot \frac{\partial^2 U_t}{\partial \eta^2}{\cdot}F_e^T \geq \frac{1}{J}\frac{\partial^2 \psi^e}{\partial \eta^2} + \frac{\partial^2 \breve{\psi}^\theta}{\partial \eta^2} + \frac{1}{J}\frac{\partial^2 \tilde{\psi}^\theta}{\partial \eta^2}; \qquad \eta = \hat{\eta}. \tag{5}$$

The first term in the right-hand side is due to variation of elastic moduli of i^{th} order $C^i(\eta)$, $i = 2,,3,...$, during PT, which produces nonlinear contributions in strain E_e, and consequently, stresses. MD simulations below demonstrate that instability criterion is linear in stresses, i.e., contribution of this term should be negligible. This term can be eliminated if $d^2C^i(\hat{\eta})/d\eta^2 = 0$, e.g., for $C^i(\eta) = C_1^i + (C_2^i - C_1^i)\chi(\eta)$ with $\chi(\eta) := \eta^3(10 - 15\eta + 6\eta^2)$. This gives a general idea for formulating the Landau potential: different interpolation functions can be used for different material properties, and if some properties should not contribute to instability conditions, function $\chi(\eta)$ can be used. For PT $1 \to 2$, i.e., for $\eta = 0$, $U_t = I$, direct calculations show that the last term also disappears, and Eq.(5) simplifies to

$$W = \sigma{:}F_e^{T-1} \cdot \frac{\partial^2 U_t(0)}{\partial \eta^2}{\cdot}F_e^T \geq 2A(\theta), \tag{6}$$

Eq.(2) is our final instability criterion for general loading. For the particular case of loading by three stresses normal to the cubic faces, all tensors in Eq.(2) are coaxial, F_e^{T-1} and F_e^T eliminate each other, and with the help of Eq.(3) we obtain the following instability criterion:

$$W = a_1\sigma_0\varepsilon_{0t} + a_2 S{:}e_t \geq A(\theta), \tag{7}$$

where $\sigma_0 := 1/3\sigma{:}I$ is the mean stress and S is the deviatoric stress. Since W represents a modified transformation work (for $a_1 = a_2 = 1$ it transforms to the transformation work), instability criterion (3) and more general criterion (2) will be called the critical modified transformation work criterion. Similar criterion can be obtained for the reverse PT $2 \to 1$ by placing $\eta = 1$. This was done, but results will be presented for the case when phase 2 was considered as the reference phase and the same criteria (2) and (3) are applicable with U_t^{-1} instead of U_t.

2.3 Confirmation of the instability criterion by molecular dynamics simulations

In order to confirm and specify the obtained lattice instability criterion, MD results for cubic-tetragonal PTs Si I↔Si II have been first obtained for various combinations of three normal prescribed Cauchy stresses σ_i along cubic axes; negative stresses are compressive, and compressive σ_3 has the largest magnitude. Components $\varepsilon_{t1} = \varepsilon_{t2} = 0.1753$ and $\varepsilon_{t3} = -0.447$, therefore, $\varepsilon_{t0} = -0.0964$ have been determined by comparing crystal lattice of Si I and II at zero stresses. Then for the reverse PT $U_t^r = U_t^{-1}$, i.e., components $\varepsilon_{t1}^r = \varepsilon_{t2}^r = -0.1492$, $\varepsilon_{t3}^r = 0.8083$, and therefore $\varepsilon_{t0} = 0.5099$. Microstructure evolution during PTs Si I↔Si II is presented in Fig. 6.1, supplementary figures and movies. Typical uniaxial stress - strain curves for σ, P, and the second Piola-Kirchhoff stress $T = F^{-1} \cdot P$ for direct and reverse PTs are shown in Fig. 6.1 under prescribed σ, P, and displacements (strains). For prescribed σ, instability for PT Si I→Si II starts at maximum Cauchy stress (point I, $E = 0.2293$), i.e., at zero value of corresponding elastic modulus, which is typical here for multiaxial loading as well; P and T continue growing beyond the instability point I. However, reverse PT starts at a minimum stress but *nonzero value of any elastic moduli*, i.e., it cannot be described by traditional zero-moduli approach. Instability is easily detected by the impossibility of equilibrating the system under fixed σ until it transforms to an alternative phase. After instability point I, the microstructure initially evolves homogeneously, then heterogeneously with stochastic fluctuations, then with bands consisting of some intermediate phases (Fig. 6.1). At larger strains, bands with fully formed Si II appear and grow. However, if starting with band structure, the stress increases (i.e., strain reduces) toward instability point I, heterogeneous fluctuating structure is observed even in the vicinity of instability point I (Fig. 6.1). Thus, multiple solutions–including homogenous and various heterogeneous ones–are observed after instability. Importantly, instability under heterogeneous perturbations does not start earlier than it is determined by criterion (3) under homogenous perturbations.

When the first Piola-Kirchhoff stress P was prescribed instead of σ, the *stress-strain curves and instability point I did not change*. This is in agreement with predictions of our approach and in

contrast to zero-moduli approach (32; 62; 85; 1; 56; 57). Since P continues growing after instability for some stress increment until $E = 0.2610$, the sample with homogeneous microstructure still can be equilibrated until maximum of P. In the Ginzburg-Landau simulations this solution would correspond to nonzero η, i.e., some intermediate homogenous phase. Since we cannot determine our order parameter from MD simulations for the PT in Si (because there are no visible shuffles (see below) and we cannot distinguish elastic and transformation strains for the intermediate states), we cannot claim from this homogenous simulation result that instability point is the same as for prescribed σ. However, if starting with a band structure at larger strain, the first Piola-Kirchhoff stress increases (strain reduces) toward instability point I, heterogeneous structure is retained in the vicinity of instability point I and disappears after crossing it (Fig. 6.1), similar to the case with controlled Cauchy stress. Thus, multiple solutions (including homogenous and various heterogeneous) are observed after maximum in the Cauchy stress I, which confirms our analytical result that instability stress is independent of the type of prescribed stress. We believe that if we would solve the problem for a much longer time between maxima in σ and P, then proper fluctuation will lead to heterogeneous solution as well.

For strain-controlled loading, the equilibrium stress-strain curve is determined in Fig. 6.1b, which is the same for direct and reverse PTs. Stress-strain curves for direct and reverse PTs under controlled P and σ differ slightly but are still very close to each other and curves for strain-controlled loading, despite the finite loading rate. Again, while initial homogenous structure persisted untill $E = 0.2927$, if we instead started with larger strain and a two-phase microstructure and reduced the strain, the heterogeneous microstructure is retained until instability point I. Since multiple solutions exists for $E > 0.2293$, $E = 0.2293$ is the instability point for prescribed strain as well.

The main result is that *instability stresses for both direct and reverse PTs for the broad variation of all three stresses are described within high accuracy by the criterion* (3), see Figs. 5.2-5.3. Thus, it is sufficient to find just two material parameters for two different stress states in order to describe instability at any other stress states. For direct PT, these parameters are $A(\theta)/a_1 = 5.40GPa$ and $a_2/a_1 = 0.76$, for the reverse PT $A(\theta)/a_1 = 7.83GPa$ and $a_2/a_1 = 1.04$. In particular, for $\sigma_1 = \sigma_2$,

both instability lines are combined in Fig. 5.3A. Due to different slopes, stress hysteresis (i.e., difference between instability stress for direct and reverse PT) reduces down to zero with reducing compressive and then increasing tensile σ_1. Since the phase equilibrium line is between instability lines, when they intersect, this is the phase equilibrium stress as well. Thus, the energy barrier between phases disappears at this point; consequently, interface energy is zero, and the interface width diverges (11), but transformation strain is finite. This is a very unusual type of PT. If confirmed by experiments, these results will allow one to control/reduce stress hysteresis, interface energy, and dissipation by controlling the multiaxial stress state.

According to criterion (3), if one varies σ_2 while keeping $\sigma_1 = -\sigma_2$, critical σ_3 for instability should not change. It looks counterintuitive from traditional wisdom because such a loading changes the symmetry of a lattice in the $1-2$ plane. However, this prediction is confirmed in Fig. 5.3B for both direct and reverse PTs with high accuracy.

Note that the parameter J for Si I→Si II PT varies between 0.780 and 0.942 for our simulation results, i.e., by 20%. If the multiplier J was not introduced in front of $\breve{\psi}^{\theta}$ in Eq.(4) for correct description of interfacial stresses, such an error would be observed between instability criterion (2) and results of the simulation. This demonstrates nontrivial consistency in the description of completely unrelated phenomena, such as instability under a homogeneous state and stresses within a finite-width interface between parent and product phases. Also, since interfacial stresses for solid-solid PTs have been introduced recently in (11) and were not implemented in the Ginzburg-Landau theory by any other group (in contrast to the sharp interface approach, see, e.g., (16)), this result will give further motivation for introducing them in other Ginzburg-Landau theories.

Also, due to the absence of off-diagonal terms in U_t, shear stresses along cubic planes should not contribute to criterion (2) in the small-strain approximation, but they do change symmetry of the lattice in various ways. There is a small contribution from shear stresses due to geometric nonlinearity. Again, MD simulations prove the validity of the instability criterion (2) for applied single, double, and three shear stresses at different planes (Fig. 4.4): change in the modified transformation work W does not exceed $\pm 2\%$.

It is intriguing that our instability criterion (3) also corresponds to the zero-elastic-moduli condition in terms of Cauchy stress for some cases. Explanation of this coincidence is the future challenging problem, which hopefully will lead to a new understanding of the nature of crystal instabilities. However, even now, this coincidence has three important consequences.

(a) It explains why the zero-moduli condition was successful for the description of many results (32; 62; 85; 1; 28; 70), and it is not in contradiction with the criterion (3).

(b) While the choice of the stress measure in the previous instability conditions was arbitrary (32; 62) (which lead to the choice of the instability criterion without proper justification), current results clarify that it should be the Cauchy stress.

(c) The unexpected result that zero-modulus conditions are met at the plane (3) in stress space creates a very strong constraint on the formulation of the nonlinear elasticity rule. This should lead to significant progress in the formulation of higher-order elastic potential, stress-strain relationships, and, consequently, Landau potential for large strains.

One of the important physical questions is: what is the order parameter, which, by definition, describes instability? There are three options: (a) It can be related to some combination of components of the strain tensor, which results in the zero-moduli instability condition. This direction was initiated in (17) and is still broadly represented. However, since zero-moduli instability condition is not applicable at least to Si II→Si I PT, the order parameter cannot be related to the components of the strain tensor. (b) It can be related to some shuffles, which would result in all the equations obtained here. However, the present MD simulations of Si I to Si II transformations show that the displacements of all atoms inside the crystal cell correspond to the same F which agrees with the Cauchy-Born hypothesis. That is, we cannot identify any shuffles, which are independent of F. (c) Because instability is described in terms of components of the transformation deformation gradient U_t, the order parameter in this work is unambiguously and naturally related to each components of U_t through interpolation functions $\varphi(a, \eta)$ (Eq.(3)), which satisfy the above formulated conditions. This is an important conclusion for the development of the Ginzburg-Landau-type theories.

Traditionally, instability criterion is evaluated for the current equilibrium state of the crystal lattice and is independent of its final state, i.e., product phase. However, instability criterion (3) includes transformation strain, i.e., it depends on the final state of the lattice. This is a seeming contradiction. Indeed, the transformation strain appears in the instability criterion because of specific interpolation function (3) chosen in our theory. However, multiplication of the components of the transformation strain in Eq.(3) by different multipliers a_1 and a_2 changes transformation strain to a completely different tensor, which is not related to the product phase.

2.4 Concluding remarks

To summarize, a conceptually novel approach and a specific crystal lattice instability criterion, which predicts the initiation of the first order PTs in materials under general multiaxial loadings, are developed and validated. In contrast to the existing traditional instability criteria (such as zero moduli or soft phonon modes), the developed approach includes an order parameter, which describes the entire dissipative transformation process. The proposed criterion is rigorously derived utilizing the second law of thermodynamics. The criterion is proven to represent material properties and is independent of the type of the prescribed stress or strain measures. The criterion is validated through hundreds of MD simulations, for direct and reverse PTs between Si I and Si II phases under various combinations of three normal and three shear stresses. The correspondence between theory and simulations is excellent, deviation does not exceed 2 %. Most interestingly, all three shear stresses do not affect instability, which directly follows from our theory but sounds very counterintuitive compared to traditional approaches. The criterion is linear in all stress components and can be calibrated by simulations at only two different stress states. Thus, it represents a predictive analytical tool, which determines how to combine six stress components to initiate various PTs in materials. Traditional approaches do not supply an analytical expression and require numerical simulations for each stress state. That is why there was no data in literature for PT criteria under more than two stresses. The obtained results also significantly advance the generalized

Landau-type theory for PTs in terms of unexpected dependence of transformation strain, elastic and thermal parts of the free energy as functions of an order parameter.

It is clear that the employment of empirical interatomic potentials introduces errors in the obtained results and that ab initio studies will be more reliable for Si and other materials. Still, instability criterion (2) is proven here for the model material described by the chosen interatomic potential, which is sufficient from the conceptual point of view. We expect that the obtained results will stimulate similar ab initio studies and experimental measurements of lattice instabilities under multiaxial loading in order to check the validity of instability criterion (2). However, direct experimental proof is not straightforward due to the presence of defects which cause local lattice instability before external stresses reach criterion (2). We may speculate that defects can modify the parameters in criterion (2), but criterion (2) still remains linear in stress relationships; this will be checked numerically with the Ginzburg-Landau approach (54) calibrated by results obtained here. One of the confirming experimental results is reported in (19) for variant-variant transformation in Cu-Al-Ni alloy under biaxial tension. Also, similar linear stress conditions for initiation of plastic flow in metallic glasses were revealed in MD simulations in (20) which may indicate that our theoretical approach will also be applicable for this instability, as well as dislocations, twinning, and different types of PTs. Another important result of the current study is enabling the quantitative estimation of the strong effect of nonhydrostatic stresses on high pressure PTs, which is observed experimentally and utilized to drastically reduce transformation pressure (1; 6; 7).

Some equations and derivations

1. Dissipation rate

Using the first and second laws of thermodynamics, the dissipation rate due to phase transformation for homogeneous states can be derived in the following form (49)

$$D = X\dot{\eta} \geq 0; \qquad X := P^T \cdot F_e : \frac{\partial U_t(\eta)}{\partial \eta} - \frac{\partial \psi(E_e, \theta, \eta)}{\partial \eta}, \tag{8}$$

where X is the thermodynamic force for change in η, $E_e = 0.5(F_e^T \cdot F_e - I)$ is the Lagrangian elastic strain, and θ is the temperature.

2. Material properties in the generalized Landau theory

We would like to enforce that for stable or metastable bulk phases $\eta = \hat{\eta}$, where $\hat{\eta} = 0$ for phase 1 and $\hat{\eta} = 1$ for phase 2. It is convenient to express any material property M (e.g., transformation strain U_t, elastic moduli of i^{th} order $C^i(\eta)$, $i = 2, , 3, ...$, energy, entropy, specific heat, etc.) in the form

$$M(\eta, \theta) = M_1(\theta) + (M_2(\theta) - M_0(\theta))\varphi_m(\eta), \tag{9}$$

where M_1 and M_2 are values of the property M in bulk phases 1 and 2, respectively, and $\varphi_m(\eta)$ is the corresponding interpolation function, which satisfies evident conditions

$$\varphi_m(0) = 0, \qquad \varphi_m(1) = 1. \tag{10}$$

3. Thermodynamic equilibrium condition for the order parameter

However, it is not sufficient to verbally impose that $\eta = 0$ corresponds to phase 1 and $\eta = 1$ corresponds to phase 2. This should directly follow from the thermodynamic equilibrium condition for the order parameter η, which is $X = 0$. Thus, we impose the following condition:

The set of constant order parameter $\eta = \hat{\eta}$ should satisfy the thermodynamic equilibrium condition

$$X = P^T \cdot F_e : \frac{\partial U_t(\eta)}{\partial \eta} - \frac{\partial \psi(E_e, \theta, \eta)}{\partial \eta} = 0 \tag{11}$$

for any stress P, temperature θ, and corresponding elastic deformation gradient F_e. Otherwise, thermodynamic equilibrium values of the order parameter obtained from the condition $X = 0$ will depend on P and/or θ. Substituting them in Eq.(9) will introduce artificial temperature and stress dependence of the property M and will not allow known properties M_1 and M_2 for bulk phases 1 and 2 to be obtained.

Due to the independence of U_t and ψ, Eq.(11) splits into two equations:

$$\frac{\partial U_t(\hat{\eta})}{\partial \eta} = 0; \qquad \frac{\partial \psi(E_e, \theta, \hat{\eta})}{\partial \eta} = 0. \tag{12}$$

Also, following from Eq.(12), for any material property one has

$$\frac{d\varphi_m(0)}{d\eta} = \frac{d\varphi_m(1)}{d\eta} = 0. \tag{13}$$

These constraints play a crucial role in finding equations for F_t and ψ as well as lattice instability criterion.

4. Criterion for the instability of the thermodynamic equilibrium under prescribed first Piola-Kirchoff stress P

Instability of the homogeneous equilibrium state under homogeneous perturbations, i.e., for material point, can only be analyzed for prescribed boundary conditions for some stress measure. We will start with prescribed nominal force stress–i.e., the nonsymmetric first Piola-Kirchoff stress P.

Definition. If a spontaneous deviation of the order parameter $\Delta\eta$ from the thermodynamic equilibrium values $\hat{\eta}$ is thermodynamically admissible under prescribed boundary conditions – that is, $D \geq 0$ – then the equilibrium is unstable.

Thus, one has the following condition:

$$X\left(P, F_e + \Delta F_e, \hat{\eta} + \Delta\eta\right)\, \dot{\eta} \geq 0 \qquad \rightarrow \text{ equilibrium of phase } \hat{\eta} \text{ is unstable,} \tag{14}$$

for stress $P = const$ and the elastic deformation gradient F_e that varies due to spontaneous variation in η. Developing the Taylor series of X around equilibrium values $\hat{\eta}$ while taking into account that $X\left(P, F_e, \hat{\eta}\right) = 0$, one obtains from Eq. (14):

$$\left.\frac{\partial X\left(P, F_e, \hat{\eta}\right)}{\partial \eta}\right|_P \dot{\eta}^2 \geq 0 \quad \rightarrow \quad \left.\frac{\partial X\left(P, F_e, \hat{\eta}\right)}{\partial \eta}\right|_P \geq 0. \tag{15}$$

Let us find an explicit expression for $\left.\frac{\partial X}{\partial \eta}\right|_P$ by direct differentiating the expression for X from Eq. (11):

$$\left.\frac{\partial X}{\partial \eta}\right|_P = P^T \cdot \frac{\partial F_e}{\partial \eta} : \frac{\partial U_t}{\partial \eta} + P^T \cdot F_e : \frac{\partial^2 U_t}{\partial \eta^2} - \left.\frac{\partial^2 \psi\left(E_e, \hat{\eta}\right)}{\partial \eta^2}\right|_{F_e} - \left.\frac{\partial^2 \psi\left(E_e, \hat{\eta}\right)}{\partial \eta\, \partial F_e} : \frac{\partial F_e^T}{\partial \eta}\right|_P. \tag{16}$$

According to the elasticity rule,

$$P \cdot U_t = \frac{\partial \psi}{\partial F_e} \quad \rightarrow \quad P = f(F_e, U_t), \tag{17}$$

where f is some function. Differentiating Eq. (17) one has

$$\frac{\partial P}{\partial \eta} = 0 = \frac{\partial f}{\partial F_e^T} : \frac{\partial F_e(\hat{\eta})}{\partial \eta}\bigg|_P + \frac{\partial f}{\partial U_t} : \frac{\partial U_t(\hat{\eta})}{\partial \eta}. \tag{18}$$

The last term in Eq. (18) and the first term Eq. (16) disappear, since, according to Eq. (12) $\frac{\partial U_t(\hat{\eta})}{\partial \eta} = 0$. Then Eq. (18) represents a system of nine homogeneous linear equations with respect to $\frac{\partial F_e(\hat{\eta})}{\partial \eta}$. Since in general $det\left(\frac{\partial f}{\partial F_e^T}\right) \neq 0$ (excluding some special stress states), this system has only the solution

$$\frac{\partial F_e(\hat{\eta})}{\partial \eta}\bigg|_P = 0. \tag{19}$$

Thus, the fourth term in Eq. (16) also disappears and Eq. (16) simplifies to

$$\frac{\partial X\left(P, F_e, \hat{\eta}\right)}{\partial \eta}\bigg|_P = P^T \cdot F_e : \frac{\partial^2 U_t(\hat{\eta})}{\partial \eta^2} - \frac{\partial^2 \psi\left(E_e\,,\ \hat{\eta}\right)}{\partial \eta^2}\bigg|_{E_e}. \tag{20}$$

This is our general instability criterion Eq. (2) in the main text.

5. Instability of the thermodynamic equilibrium for an arbitrary prescribed stress

Let some other stress measure $\tilde{T}$ be prescribed instead of nominal stress P, which is connected to P through a function $P = \phi(\tilde{T}, F) = \phi_1(\tilde{T}, F_e, U_t(\eta)) = \phi_2(\tilde{T}, F_e, \eta)$. Repeating the same procedure but at a fixed $\tilde{T}$, one obtains the following equation instead of Eq.(15)

$$\frac{\partial X\left(\tilde{T}, F_e, \hat{\eta}\right)}{\partial \eta}\bigg|_{\tilde{T}} \geq 0. \tag{21}$$

We find an explicit expression for $\frac{\partial X}{\partial \eta}\big|_{\tilde{T}}$ by direct differentiating the expression for X from Eq. (11) as follows:

$$\begin{aligned}\frac{\partial X}{\partial \eta}\bigg|_{\tilde{T}} = \frac{\partial P^T}{\partial \eta}\bigg|_{\tilde{T}} \cdot F_e : \frac{\partial U_t}{\partial \eta} + P^T \cdot \frac{\partial F_e}{\partial \eta}\bigg|_{\tilde{T}} : \frac{\partial U_t}{\partial \eta} + P^T \cdot F_e : \frac{\partial^2 U_t}{\partial \eta^2} \\ - \frac{\partial^2 \psi\left(E_e\,, \hat{\eta}\right)}{\partial \eta^2}\bigg|_{E_e} - \frac{\partial^2 \psi\left(E_e\,, \hat{\eta}\right)}{\partial \eta\, \partial F_e} : \frac{\partial F_e^T}{\partial \eta}\bigg|_{\tilde{T}}.\end{aligned} \tag{22}$$

The first two terms in Eq. (22) disappear, since, according to Eq. (12) $\frac{\partial U_t(\hat{\eta})}{\partial \eta} = 0$. Let us show that the last term in Eq. (22) is zero as well.

First, we consider that $\tilde{T}$ is a nonsymmetric tensor. Then, the elasticity rule can be presented in the form $\tilde{T} = q(F_e, U_t)$, where q is some function. Differentiating this equation with respect to η at $\tilde{T} = const$, one obtains

$$0 = \frac{\partial q}{\partial F_e^T} : \frac{\partial F_e(\hat{\eta})}{\partial \eta}\bigg|_{\tilde{T}} + \frac{\partial q}{\partial U_t} : \frac{\partial U_t(\hat{\eta})}{\partial \eta}. \tag{23}$$

The second term is equal to zero, and since in general $det\left(\frac{\partial q}{\partial F_e^T}\right) \neq 0$ (excluding some special stress states for some special stress measures), a system of nine linear equations (23) has the only solution:

$$\frac{\partial F_e(\hat{\eta})}{\partial \eta}\bigg|_{\tilde{T}} = 0. \tag{24}$$

Thus, the last term in Eq. (22) disappears, and we arrive at the instability criterion Eq. (20) for any prescribed stress measure.

If $\tilde{T}$ is a symmetric tensor, for example, Cauchy stress σ, then Eq. (23) represents six equations only, with nine unknowns. To exclude arbitrariness of the rigid-body rotation, an additional kinematic constraint should be given, which can be expressed in the form of three scalar equations $j(F_e \cdot U_t) = const$. For example, one can impose in component form

$$F_{21} = \{F_e \cdot U_t\}_{21} = 1, \qquad F_{23} = \{F_e \cdot U_t\}_{23} = 1, \qquad F_{31} = \{F_e \cdot U_t\}_{31} = 1. \tag{25}$$

Differentiating the equation of kinematic constraint with respect to η obtains

$$0 = \frac{\partial j}{\partial F_e^T} : \frac{\partial F_e(\hat{\eta})}{\partial \eta} + \frac{\partial j}{\partial U_t} : \frac{\partial U_t(\hat{\eta})}{\partial \eta}. \tag{26}$$

Again, the second term is equal to zero. Since in general the determinant of the system of nine linear equations (23) and (26) is not equal to zero, we again obtain Eq. (24).

Thus, again the last term in Eq. (22) disappears, and we arrive at the instability criterion Eq. (20) for any prescribed stress measure. Independence of the instability criterion of the boundary conditions is a very unexpected result. It is a direct consequence of conditions (12) related to the independence of the thermodynamic equilibrium value of the order parameter and consequently, the transformation strain of the stresses and temperature.

6. Evaluating the term $\frac{\partial^2(J\breve{\psi}^\theta)}{\partial\eta^2}$ in the instability criterion

Evaluation of all terms in the instability criterion (2) after substitution of explicit expressions for U_t (Eq. (3)) and ψ (Eq. (4)) is straightforward with only one exception. It is related to the new multiplier J in the term $J\breve{\psi}^\theta(\theta,\eta)$ due to interfacial stresses (see (11)), which was not considered in (49). First we prove that according to Eqs. (12) and (24),

$$\frac{\partial F(\hat{\eta})}{\partial\,\eta} = F_e \cdot \frac{\partial U_t(\hat{\eta})}{\partial\,\eta} + \frac{\partial F_e(\hat{\eta})}{\partial\,\eta} \cdot U_t(\hat{\eta}) = 0. \tag{27}$$

Then, we evaluate

$$\frac{\partial(J\breve{\psi}^\theta)}{\partial\eta} = \breve{\psi}^\theta \frac{\partial J}{\partial F^T}{:}\frac{\partial F}{\partial\,\eta} + J\frac{\partial\breve{\psi}^\theta}{\partial\eta} \tag{28}$$

and

$$\frac{\partial^2(J\breve{\psi}^\theta(\hat{\eta}))}{\partial\eta^2} = \breve{\psi}^\theta(\hat{\eta})\frac{\partial}{\partial\eta}\left(\frac{\partial J}{\partial F^T}{:}\frac{\partial F}{\partial\,\eta}\right) + 2\frac{\partial\breve{\psi}^\theta(\hat{\eta})}{\partial\eta}\frac{\partial J}{\partial F^T}{:}\frac{\partial F(\hat{\eta})}{\partial\,\eta} + J\frac{\partial^2\breve{\psi}^\theta(\hat{\eta})}{\partial\eta^2} = J\frac{\partial^2\breve{\psi}^\theta(\hat{\eta})}{\partial\eta^2}. \tag{29}$$

Indeed, the first term in Eq. (29) disappears because $\breve{\psi}^\theta(\hat{\eta}) = 0$ and the second term is zero because of Eq. (27). Eq. (29) was used in transferring from Eq.(4) to Eq.(5).

7. Modified transformation work for the general stress tensor

The general form of the Cauchy stress applied to the simulation sample is

$$\sigma = \sigma_{11} \quad \tau_{12} \quad \tau_{13} \tag{30}$$

$$\tau_{12} \quad \sigma_{22} \quad \tau_{23} \tag{31}$$

$$\tau_{13} \quad \tau_{23} \quad \sigma_{33}$$

. (32)

Under this stress state, the formula for the total and elastic deformation gradient is

$$F = F_{11} \quad F_{12} \quad F_{13} \tag{33}$$

$$0 \quad F_{22} \quad F_{23} \tag{34}$$

$$0 \quad 0 \quad F_{33}$$

, (35)

$$F_e = F_{11}^e \quad F_{12}^e \quad F_{13}^e \tag{36}$$

$$0 \quad F_{22}^e \quad F_{23}^e \tag{37}$$

$$0 \quad 0 \quad F_{33}^e$$

, (38)

where zeros under the diagonal are due to our way of excluding the rigid-body rotation. Substituting (S1) and (S2) into equation (7), the explicit general form of the expression for the modified transformation work in equation (6) in the main text is

$$W = a_1\sigma_0\varepsilon_{0t}+a_2S{:}e_t+a_2[\tau_{13}F_{13}(e_{33}-e_{11})/F_{33}+\tau_{23}F_{23}(e_{33}-e_{22})/F_{33}+\tau_{12}F_{12}(e_{22}-e_{11})/F_{22}+\tau_{13}F_{12}F_{23}(e_{11}-e_{22})/(F \tag{39}$$

When shear stresses are absent, this equation transforms to equation (6) in the main text.

Simulation Method

In this work, classical MD simulations were performed using the LAMMPS package (15). The employed interatomic force field for the interactions between Si atoms was from the Tersoff interatomic potential (23). This potential has been demonstrated to be successful in describing the crystal structure transition from the diamond-cubic to β-Sn in single crystal silicon (Si I to Si II) under a uniaxial stress of $\sim$12GPa (see (63) and current results), which is close to the experimental value (28). The majority of simulations have been performed for a Si sample containing 64,000 atoms. To prove a size-independence of the results, simulations under uniaxial loading were performed for varying sample sizes of 5nm to 40nm, which contained 8,000 to 4,096,000 atoms. A time step of 1 fs was used in all simulations. The system temperature is set as $T = 1K$ to eliminate the possibility of the occurrence of thermally activated PTs. Effects of the free surfaces on the

PTs were excluded by employing periodic boundary conditions along all three cubic directions. For uniaxial loading, simulations were conducted under (a) a specified first Pila-Kirchhoff stress; (b) a specified Cauchy stress; and (c) a strain-controlled loading. Here the first Piola-Kirchhoff stress was applied to the system by enforcing constant forces on the top and bottom layers of the atomistic system along the directions of compression. The Cauchy stress was applied to the system using the Berendsen algorithm (28), in which the instantaneous stress of the system was calculated using the virial formula and controlled in two steps. First, a Cauchy stress increment of 0.01 GPa was applied to the simulation cell; this was then followed by an equilibration of the entire specimen for 10 ps. In order to ensure that a desired Cauchy stress has been achieved, the system virial stress at the end of each loading increment was calculated and was checked against the prescribed stress, assuming that the averaged Cauchy stress coincides with the virial stress (29). It should be noted that such a weak-coupling stress-controlling strategy is different from that of using the Parinello-Rahman algorithm (31), which, in contrast, approximately controls the deviatoric component of the second Piola-Kirchhoff stress (32). In the strain-controlled loading, the fix deform method in LAMMPS was employed. That is, each time after the simulation box size along the main loading direction was changed at a value of 0.2 angstrom, the system was equilibrated for 100 ps. This equilibration process occurred with a fixed box size along the loading direction and zero stress along the other direction. Multiaxial loading was performed under controlled normal components of the Cauchy stress utilizing the Berendsen algorithm (28). However, shear stresses in LAMMPS cannot be applied with the Berendsen algorithm. They were applied with the Parinello-Rahman algorithm (31), which controls the deviatoric part of the second Piola-Kirchhoff stress (32). At the instability point, the Cauchy stress was calculated and substituted in the instability criterion.

Transformation process

A typical phase transformation processes, which was found in our MD simulations, is presented in Figs. S1 and S2. They are visualized using OVITO(30), with colors representing the local von-Mises shear strain.

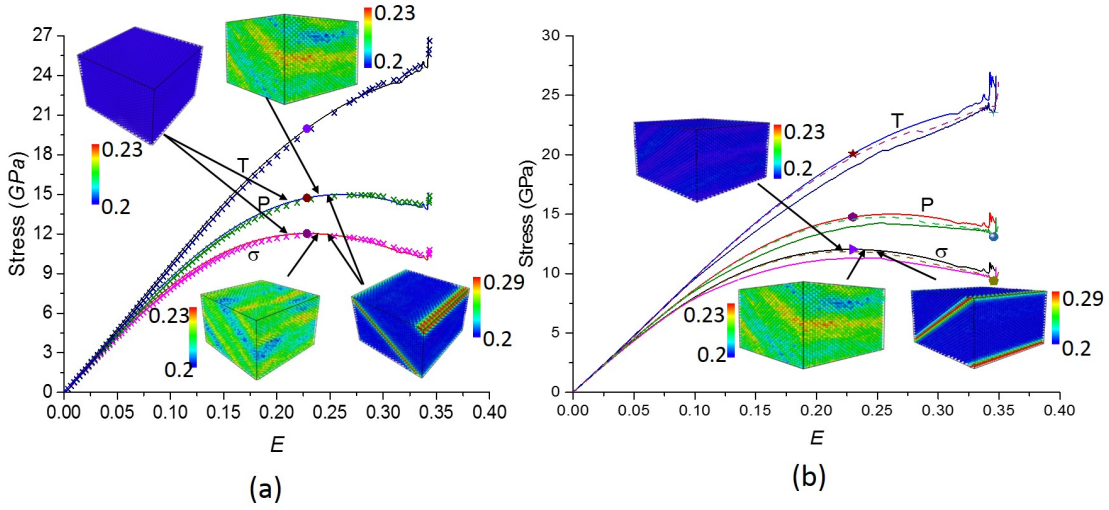

Figure 2.1 Stress - Lagrangian strain E curves for uniaxial compression ($\sigma_1 = \sigma_2 = 0$) for the Cauchy σ, the first Piola-Kirchhoff P, and the second Piola-Kirchhoff stress T for direct ((a) and upper curves in (b)) and reverse (lower curves in (b)) PTs Si I↔Si II. Dots mark instability points, which correspond to stresses above (or below for reverse PT) which crystal cannot be at equilibrium at prescribed σ or multiple (homogeneous and heterogeneous) microstructures exist. After loss of stability, the microstructure initially evolves homogeneously, then heterogeneously with stochastic fluctuations, then with bands consisting of some intermediate phases and, at larger strains, bands with fully formed Si II. Heterogenous microstructures in Fig. 1 are obtain from two phase band structures at larger strains by returning toward instability point I. (a) Results obtained for prescribed σ (lines) and P (symbols) are not distinguishable. Microstructures near σ and P curves are obtained under corresponding prescribed stresses σ and P, respectively. (b) Stress - strain curves for strain controlled loading (dashed lines), which are the same for direct and reverse PTs, in comparison with curves under controlled stresses for direct (upper lines) and reverse (lover) lines PTs.

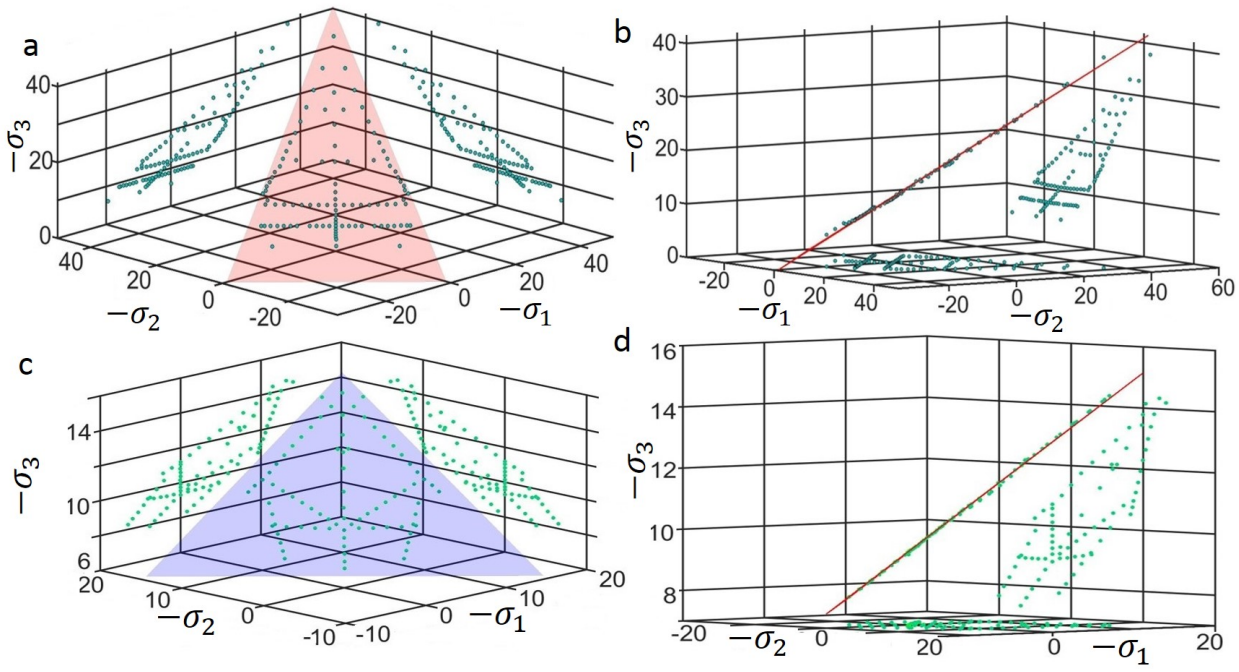

Figure 2.2 Conformation of lattice instability criterion (3). (A) Plane in stress space corresponding to the instability criterion (3) for direct Si I→Si II PT and instability points from MD simulations, along with projection of each point on $\sigma_i - \sigma_j$ planes. Projections allow one to determine coordinates of each point. (B) The same plot but rotated until theoretical plane (3) is visible as a line, to demonstrate how close all simulation points are to the theoretical plane. (C) and (D) are the same as in (A) and (B) but for reverse Si II→Si I PT.

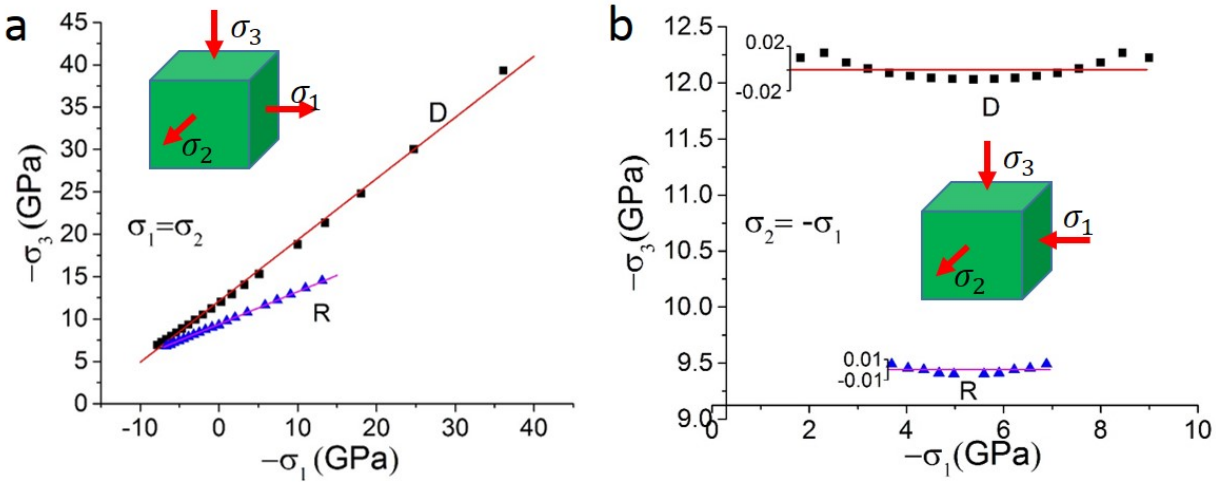

Figure 2.3 Relationships between stresses σ_2 and σ_3 corresponding to the lattice instability for direct (D) and reverse (R) Si I↔Si II PTs for (A) $\sigma_1 = \sigma_2$ and (B) $\sigma_1 = -\sigma_2$. Bars in (B) show relative error of the simulation results relatively theoretical prediction.

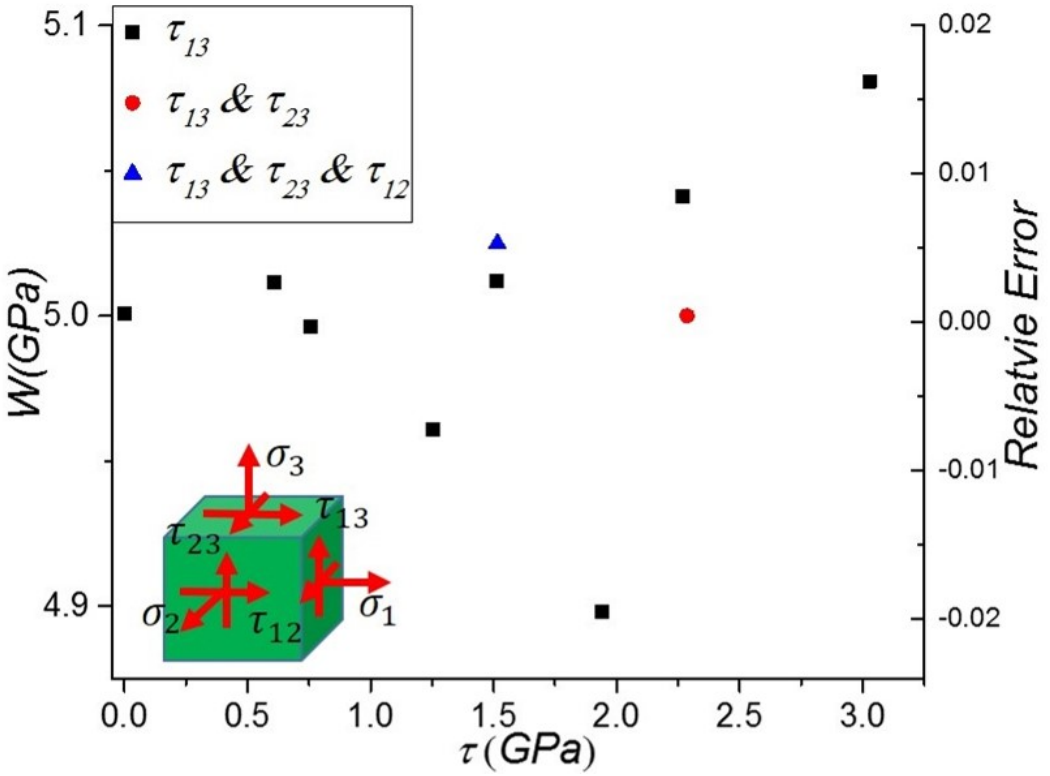

Figure 2.4 Modified transformation work in the instability criterion (2) versus maximum shear stress for normal stresses in the ranges $\sigma_1 = 1.50 - 2.17$, $\sigma_2 = 1.41 - 1.61$, and $\sigma_3 = 10.38 - 10.76\ GPa$.

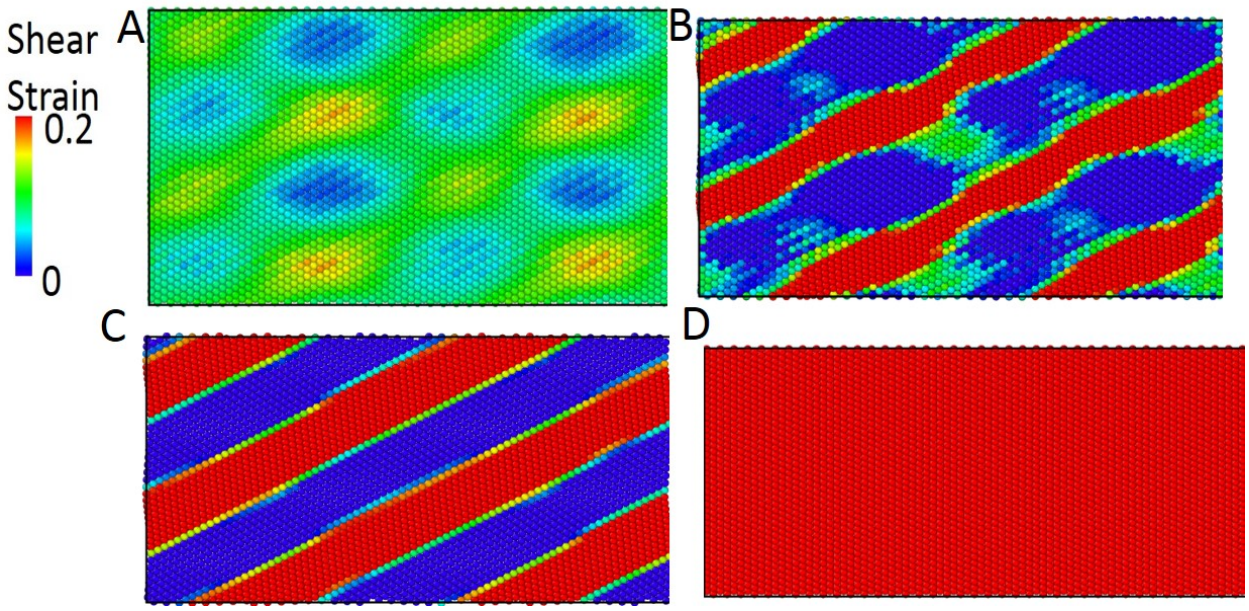

Figure 2.5 Phase transformation process for Si I→Si II under uniaxial loading. (A) heterogeneous nucleation of silicon II due to stress fluctuation. (B) and (C) due to internal stresses caused by the transformation strain, complete Si II and residual Si I reshape into bands. Note that Si I bands are formed through the reverse PT. (D) Final stable state of Si II.

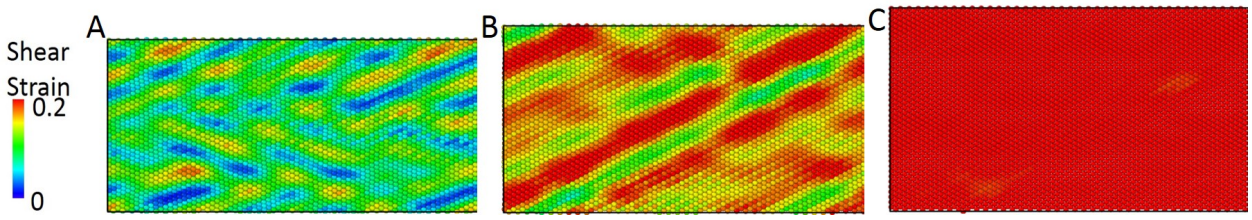

Figure 2.6 Phase transformation process for Si II→Si I under uniaxial unloading. (A) Heterogeneous nucleation of silicon I due to stress fluctuation. (B) Formation of band-like structure consisting of almost complete Si I and some intermediate phase, but without Si II. (C) Final stable state of Si I.

Bibliography

[32] R. Hill, F. Milstein. Principles of stability analysis of ideal crystals, Phys. Rev. B 15 (1977) 3087-3096.

[62] F. Milstein, J. Marschall, H. Fang. Theoretical bcc→fcc transitions in metals via bifurcations under uniaxial load, Phys. Rev. Lett. 74 (1995) 2977-2980.

[85] J. Wang, S. Yip, S.R. Phillpot, D. Wolf. Crystal instabilities at finite strain, Phys. Rev. Lett. 71 (1993) 4182-4185.

[1] P. Alippi, P.M. Marcus, M. Scheffler. Strained tetragonal states and bain paths in metals, Phys. Rev. Lett. 78 (1997) 3892-3895.

[56] J. Li et al. Atomistic mechanisms governing elastic limit and incipient plasticity in crystals, Nature 418 (2002) 307-310.

[57] J. Li, T. Zhu, S. Yip, K.J.V. Vliet, S. Suresh. Elastic criterion for dislocation nucleation, Mat. Sci. Eng. A 365 (2004) 25-30.

[7] M. T. Dove. Introduction to Lattice Dynamics. Cambridge University Press (1993).

[28] G. Grimvall, M.-K. Blanka, V. Ozolins, K.A. Persson. Lattice instabilities in metallic elements, Rev. Mod. Phys. 84 (2012) 945-986.

[70] J. Pokluda, M. Cerny, M. Sob, Y. Umeno. Ab initio calculations of mechanical properties: Methods and applications, Prog. Mater. Sci. 73 (2015) 127-158.

[22] R.S. Elliott, N. Triantafyllidis, J.A. Shaw. Reversible stress-induced martensitic phase transformations in a bi-atomic crystal, J. Mech. Phys. Solids 59 (2011) 216-236.

[23] K. Gaal-Nagy, M. Schmitt, P. Pavone, D. Strauch. Ab initio study of the high-pressure phase transition from the cubic-diamond to the beta-tin structure of Si, Comp. Mater. Sci. 22 (2001) 49-55.

[68] A. Planes, L. Manosa. Vibrational properties of shape memory alloys, Solid State Phys. 55 (2001) 159-267.

[1] V.D. Blank, E.I. Estrin. Phase Transitions in Solids under High Pressure. Boca Raton: CRC Press; (2014) 382-423.

[49] V.I. Levitas. Phase-field theory for martensitic phase transformations at large strains, Int. J. Plasticity 49 (2013) 85-118.

[11] V.I. Levitas. Phase field approach to martensitic phase transformations with large strains and interface stresses, J. Mech. Phys. Solids 70 (2014) 154-189.

[16] F. D. Fischer, T. Waitz, D. Vollath, N. K. Simha. On the role of surface energy and surface stress in phase-transforming nanoparticles, Prog. Mat. Sci. 53 (2008) 481-527.

[17] G.R. Barsch, J.A. Krumhansl. Twin Boundaries in Ferroelastic Media without Interface Dislocations, Phys. Rev. Lett. 53 (1984) 1069-1072.

[54] V.I. Levitas, M. Javanbakht. Phase transformations in nanograin materials under high pressure and plastic shear: nanoscale mechanisms, Nanoscale 6 (2014) 162-166.

[19] R. Abeyaratne, C. Chu, R.D. James. Kinetics of materials with wiggly energies: theory and application to the evolution of twinning microstructures in a Cu-Al-Ni shape memory alloy, Philos. Mag. A 73 (1996) 457-497.

[20] C.A. Schuh, A.C. Lund. Atomistic basis for the plastic yield criterion of metallic glass, Nat. Mater. 2 (2003) 449-452.

[6] V.I. Levitas, L.K. Shvedov. Low-pressure phase transformation from rhombohedral to cubic BN: Experiment and theory, Phys. Rev. B 65 (2002) 104109.

[7] C. Ji, V. I. Levitas, H. Zhu, J. Chaudhuri, A. Marathe, Y. Ma Shear-induced phase transition of nanocrystalline hexagonal boron nitride to wurtzitic structure at room temperature and lower pressure, P. Natl. Acad. Sci. USA 109 (2012) 19108-19112.

[49] V.I. Levitas. Phase-field theory for martensitic phase transformations at large strains, Int. J. Plasticity 49 (2013) 85-118.

[11] V.I. Levitas. Phase field approach to martensitic phase transformations with large strains and interface stresses, J. Mech. Phys. Solids 70 (2014) 154-189.

[15] P. Steve. Fast parallel algorithms for short-range molecular dynamics, J. Comput. Phys. 117 (1995) 1-19.

[23] H. Balamane. Comparative study of silicon empirical interatomic potentials, Phys. Rev. B 46 (1992) 2250.

[63] K. Mizushima. Ideal crystal stability and pressure-induced phase transition in silicon, Phys. Rev. B 50 (1994) 14952.

[28] V. Domnich, D. Ge, and Yu. Gogotsi. Indentation-Induced Phase Transformations in Semiconductors, In: High Pressure Surface Science and Engineering; Section 5.1, eds. Y. Gogotsi and V. Domnich, (Institute of Physics, Bristol, 2004), 381-442.

[28] H.J. Berendsen, J. V. Pstma, van Gunsteren, W. F. DiNola, and J. R. Haak. Molecular dynamics with coupling to an external bath J. Chem. Phys. 81 (1984) 3684.

[29] A. K. Suhramaniyan. Continuum interpretation of virial stress in molecular simulations, Int. J. Solids Struct. 45 (2008) 4040-6.

[31] M. Parrinello. Polymorphic transitions in single crystals: A new molecular dynamics method, J. Appl. Phys. 52 (1981) 7182-90.

[32] R. E. Miller, E. B. Tadmor, J. S. Gibson, J. S. Bernstein, and F. Pavia. Molecular dynamics at constant Cauchy stress. J. Chem. Phys. 144 (2016) 184107.

[30] A. Stukowsk. Visualization and analysis of atomistic simulation data with OVITO: the Open Visualization Tool, Model. Simul. Mater. Sc. 18 (2010) 015012.

CHAPTER 3. DEFORMATION, LATTICE INSTABILITY, AND METALLIZATION DURING STRUCTURAL PHASE TRANSFORMATIONS BETWEEN Si I AND Si II UNDER GENERAL STRESS TENSOR: THE FIRST-PRINCIPLES STUDIES

Reproduced from 'Zarkevich, Nikolai A., Hao Chen, Valery I. Levitas, and Duane D. Johnson. Lattice Instability during Solid-Solid Structural Transformations under a General Applied Stress Tensor: Example of Si I Si II with Metallization. Physical Review Letters 121, no. 16 (2018): 165701.'

3.1 Introduction

Phase transformations (PTs) in solids are traditionally characterized by the pressure-temperature phase diagram, each line of which corresponds to thermodynamic equilibrium (79). However, actually observed PTs occur under significant deviations from the equilibrium (99; 72; 76; 7), and most first-order PT are accompanied by a hysteresis. For example, the phase equilibrium pressure for graphite-diamond in carbon at room temperature is 2.45 GPa; however, due to hysteresis, the direct PT starts at 70 GPa in experiment (72). The high-pressure superhard cubic phase of boron nitride (BN) is stable at ambient conditions (76), however, highly disordered hexagonal BN does not transform even at 52.8 GPa (7). The reason for deviation of the actual PT pressure from the equilibrium one is the enthalpy barrier. When the effect of thermal fluctuations can be neglected, e.g., at low temperature and relatively short observation time, the PT criterion is related to disappearance of the enthalpy barrier, i.e., to the lattice instability. That is why lattice instability conditions are intensively studied under hydrostatic, uniaxial and multiaxial loadings (32; 62; 85; 28; 70; 52; 53). While phase equilibrium under stress tensor can be derived within con-

tinuum thermodynamic treatment for elastic (29) and elastoplastic (46) materials, lattice instability requires a separate consideration.

In experiments, there is a significant reduction in the PT pressure due to the deviatoric (non-hydrostatic) stresses and especially plastic strains (47; 1; 7; 20; 51). For example, a large plastic shear reduced PT from highly disordered to superhard wurtzitic BN from 52.8 to 6.7 GPa (7), i.e., by an order of magnitude. This phenomenon is extremely important from both fundamental and applied points of view, because it may reduce the PT pressure for numerous high-pressure phases with unique properties to a practical level. A physical mechanism responsible for this reduction was suggested in (47). Plastic strain produces dislocation pileups. Since all stresses at the tip of a dislocation pileup are proportional to the number of dislocations in a pileup, which can be as high as 10 to 100, local stresses exceed the lattice instability limit and cause barrierless nucleation of a high-pressure phase even at relatively small external pressure. This was rationalized in (47) based on analytical model and in (54; 35) using phase field approach. However, input in the phase field model – PT (instability) criteria for direct and reverse PTs for an ideal crystal under *general stress tensor* – was assumed hypothetically because such criteria are not known for any material. In addition, for many materials there is a significant difference between calculated instability pressure (e.g., 64-80 GPa for Si I→Si II PT (63; 23)) and experimentally determined PT pressure (e.g., 9-12 GPa for the same PT (19)). This reduction was qualitatively explained by presence of the local stress concentrators around defects (dislocations, grain boundaries, etc.) and the effect of the nonhydrostatic stresses. Quantitative solution of this problem requires knowledge of the lattice instability conditions under stress tensor, similar to the previous problem.

That is why the goal of the current paper is to perform the first DFT study of the deformation process, elastic instabilities, as well as metallization under general stress tensor that are responsible for the cubic-tetragonal Si I↔Si II PTs. While finding instability criteria under all six components of the stress tensor seems hopeless due to large number of their combinations, unexpected guidance came from the crystal lattice instability criterion formulated within the phase field approach (49; 52; 53; **?**). Due to technological importance of Si, there is huge literature related to PTs in it.

PT in Si I under hydrostatic and two-parametric nonhydrostatic loadings was studied with DFT in (63; 23). Lattice instability under two-parametric nonhydrostatic loadings of Si I was studied in (80; 13; 78; 70) but not related to a PT. Importantly, PT in Si under plastic deformations is utilized in ductile regime of machining of Si (65).

Tensors will be designated with boldface symbols; contractions of tensors $A = \{A_{ij}\}$ and $B = \{B_{ji}\}$ over one and two indices is designated as $A{\cdot}B = \{A_{ij}\, B_{jk}\}$ and $A{:}B = A_{ij}\, B_{ji}$; I is the unit tensor; the inverse and transpose of A are A^{-1} and A^T, respectively.

3.2 Simulation methods

We used DFT code VASP (43; 44; 42) with the projector augmented waves (PAW) basis (9; 45) and PBE exchange-correlation functional (66). The PAW-PBE pseudo-potential of Si had 4 valence electrons (s^2p^2) and the outmost cutoff radius of 1.9 Å. The energy cutoff for the plane-wave basis was increased to ENCUT=306.7 eV, while an augmentation charge cutoff was ENAUG=322.1 eV. We used the Davidson algorithm (IALGO=38) for the electronic energy minimization. Electronic structure was calculated with a fixed number of bands (NBANDS=16) in a 4-atom unit cell. The Brillouin zone integration was performed in k-space (LREAL=FALSE), using a dense Γ-centered Monkhorst-Pack mesh (64) containing from 55 to 110 k-points per inverse angstrom (less during atomic relaxation, more for the final energy calculation). Accelerated convergence of the self-consistent calculations was achieved using the modified Broyden's method (39).

Atomic relaxation in a fixed unit cell (ISIF=2) was performed using the conjugate gradient algorithm (IBRION=2), allowing symmetry breaking (ISYM=0). The transformation path was confirmed by the nudged elastic band (NEB) calculations, performed using the C2NEB code (101). We used DFT forces in *ab initio* molecular dynamics (MD) to verify stability of the relaxed atomic structures. Si atoms were assumed to have mass POMASS=28.085 atomic mass units (amu). The time step for the atomic motion was set to POTIM=0.5 fs.

The Tersoff potential (TP), which we use in classical MD simulations, is described in (23).

3.3 Stress-free phases and energy landscape

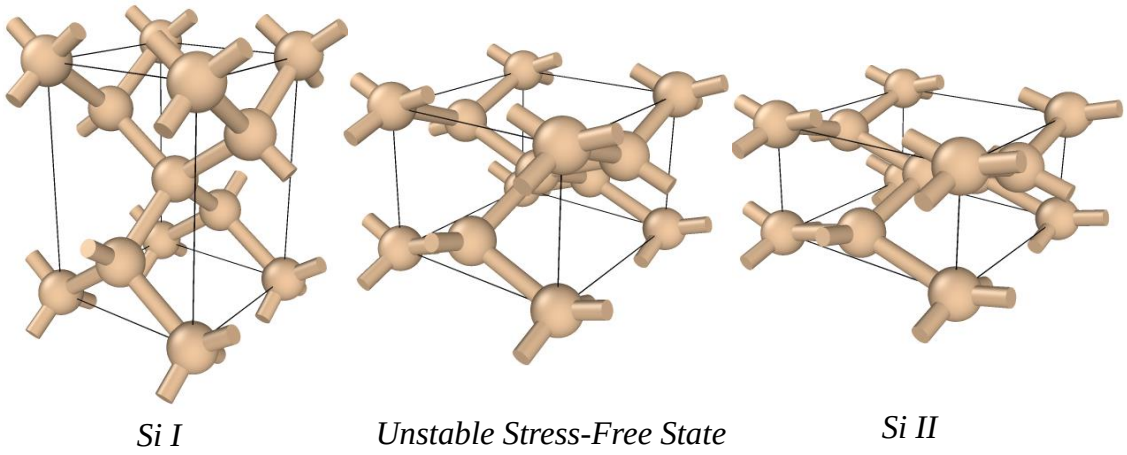

Figure 3.1 Si atoms and the nearest-neighbor bonds in tetragonal non-primitive unit cells for the stress-free Si I (left), intermediate unstable SP (middle), and Si II (right).

The fully relaxed in DFT crystal lattice of the stress-free Si I, Si II, and intermediate unstable state corresponding to the enthalpy barrier – a saddle point (SP) on the enthalpy vs. strain surface are shown in Fig. 3.1. The tetragonal cell of Si I is bounded by (110), (1$\bar{1}$0), and (001) planes. The calculated lattice parameters $a_i = b_i$ and c_i (note that $c_1 = \sqrt{2}a_1$) and corresponding relative energies are given in Tables 3.1. The calculated $c_1 = 5.4665\,\text{Å}$ is within 1% from the experimental $c_1^{exp} = 5.43\,\text{Å}$ (98). Energy landscape of Si versus lattice parameters c and a is shown in Fig. 3.2.

Table 3.1 Lattice parameters and energy E of the stress-free Si I, Si II, and intermediate unstable SP.

	a=b (Å)	c (Å)	E (eV/atom)
Si I	3.8653	5.4665	0
Si II	4.8030	2.6592	0.2949
SP	4.4847	3.4763	0.4192

3.4 Stress-strain curves

The deformation gradient $F = F_e \cdot U_t$, which maps initial undeformed state of a crystal into current deformed state, can be multiplicatively decomposed into elastic F_e and transformational U_t parts. Transformation deformation gradient U_t transforms the stress-free cell of Si I to the stress-free cell of Si II. It has components $U_{t1} = U_{t2} = a_2/a_1 = 1.243$ and $U_{t3} = c_2/c_1 = 0.486$. For comparison, the Tersoff potential in (52; 53) leads to $U_{t1} = U_{t2} = 1.175$ and $U_{t3} = 0.553$.

We will use the true Cauchy stress (force per unit deformed area) σ and the Lagrangian strain $E = 0.5(F^T \cdot F - I)$. Stress σ_3 – strain E_3 curves for compression or tension in c direction for various fixed lateral stresses $\sigma_1 = \sigma_2$ in a and b directions are presented in Fig. 6.1 along with corresponding transformation paths in $(F_1 = F_2, F_3)$ plane. The elastic instability occurs when determinant of the matrix of the elastic moduli modified by some geometrically nonlinear terms reduces to zero (32; 62; 85; 28; 70). This results in condition that some elastic moduli or their combinations reduce to zero. We will use an alternative condition, which is based on the following strict definition. Elastic lattice instability at prescribed true stress σ occurs at stresses above (or

below for the reverse PT) which crystal cannot be at equilibrium, i.e., at maximum (for direct PT) and minimum (for reverse PT) stresses at the stress-strain curves marked in Fig. 6.1. While we do not have a strict proof of the equivalency of both conditions in general case, for many particular cases they coincide.

In Fig. 6.1, a tetragonal stressed lattice of Si I transforms into a tetragonal stressed lattice of Si II, and the lattice instability does not change a lattice symmetry. The slope of the stress-strain curve is continuous and is zero at instability points. Under hydrostatic loading (dashed line in Fig. 6.1), a cubic lattice looses its stability under tetragonal perturbations, i.e., there is a bifurcation from a primary isotropic deformation to a secondary tetragonal deformation. That is why derivative at the hydrostatic instability point is discontinuous. Both under hydrostatic ($\sigma_1 = \sigma_2 = \sigma_3$) and uniaxial ($\sigma_1 = \sigma_2 = 0$) compression there are three stress-free states (Fig. 3.1): Si I, Si II (stable or metastable enthalpy minima) and an intermediate unstable state, corresponding to the saddle point (enthalpy barrier) on the enthalpy vs. strain surface. Existence of a stress-free metastable Si II was not discussed in the literature. Note that there is no phonon instability for a stress-free Si II (24; 25; 102). This surprising result leads to formulation of a problem on searching for a pressure-plastic shear path for arresting the metastable Si II, as it is suggested in (47) for any metastable phase. In experiments, Si II does not reverse to Si I, but transforms to Si XII and then to Si III under slow unloading, or to amorphous Si under fast unloading (19).

Stress σ_3 – strain E_3 curves for a uniaxial compression at $\sigma_1 = \sigma_2 = 0$, obtained with DFT and Tersoff potential-based simulations, are compared in Fig. 3.4. While the maximal stresses for Si I corresponding to the elastic lattice instability (see below) in both approaches are comparable, other features (including elastic rule for SI I, strain for the lattice instability of Si I, and transformation strain) differ significantly. In the TP-based simulations, stress-strain curve does not intersect zero-stress axis, i.e., stress-free Si II is unstable. The same is true for the Stillinger-Weber and modified Tersoff potentials (53).

3.5 Elastic lattice instability under two-parametric loading

Elastic lattice instability at $\sigma_1 = \sigma_2$ for direct (σ_{3d}) and reverse (σ_{3r}) PTs is shown in Fig. 5.3. Both instability conditions are approximated by linear relationships. TP-based results from (52; 53) for Si I→Si II PT are generally in good agreement with the current DFT results, however there is a difference for tensile and small compressive σ_1, where TP results are slightly higher and nonlinear; at a tensile stress $\sigma_1 > 8$ GPa they cross the instability line for the reverse PT. Also, under hydrostatic loading, PT pressure from DFT and Tersoff potential is 75.81 GPa and 79.58 GPa, respectively.

For uniaxial compression we obtained PT stress $\sigma_{3d} = -11.03\,\text{GPa}$ at $E_3 = -0.154$. In comparison, DFT simulations in (13) give $\sigma_{3d} = -10.6\,\text{GPa}$ and $E_3 = -0.16$ (recalculated from engineering strain in (13)); DFT results in (78) using two different methods suggest $\sigma_{3d} = -11.9$ (-12.7) GPa and $E_3 = -0.14$ (-0.16) (recalculated from logarithmic strain in (78)); and TP in (52; 53) gives $\sigma_{3d} = -12.03\,\text{GPa}$ and $E_3 = -0.232$. Note that pressure for uniaxial loading is $-\sigma_{3d}/3 = 3.68\,\text{GPa}$, which is $75.81/3.68 = 20.6$ times lower than under hydrostatic conditions. This characterizes very strong effect of nonhydrostatic stresses on PT pressure, which can partially explain significantly lower experimental PT pressure than the instability pressure and scatter in experimental data under quasi-hydrostatic conditions. The instability lines are described by $\sigma_{3d} = -10.9 + 1.20\sigma_1$ for $\sigma_1 \subset [-75.81; 17]$ and $\sigma_{3r} = 7.175 + 0.4209\sigma_1$ for $\sigma_1 \subset [-70; 17]$. Theoretical strength in (13) is approximated as $\sigma_{3d} = -10.6 + 0.77\sigma_1$ for $\sigma_1 \subset [-15; 12]$. Since it is close to our result, instability in (13) is related to Si I→Si II PT.

While instability line for direct PT in (52; 53) with TP-MD is quite close to our DFT results, for reverse PT the TP-MD results are completely different from DFT. Consequently none of the classical MD potentials in (52; 53) (Tersoff, modified Tersoff, and Stillinger-Weber potentials) are able to describe the reverse PT. This also means that phenomena related to coincidence of the direct and reverse PTs in some tensile lateral stress range predicted in (53) are not realistic for Si I. Still, they may be found in other materials.

3.6 Metallization under biaxial loading

Electronic structure in Si I had been studied under different combinations of σ_3 and fixed $\sigma_1 = \sigma_2$. Examples of the electronic band gap vs. compressive or tensile strain are given in Fig. 3.6. For each $\sigma_1 = \sigma_2$, there is a strain E_3 for which the band gap reaches its maximum, while change of strain E_3 in both directions reduces the band gap down to zero. The band gap maximum is observed at $\sigma_1 = \sigma_2 = -10\,\text{GPa}$ and $\sigma_3 = -10.5\,\text{GPa}$, see Fig. 3.6. The band gap disappears at the metallization curve, shown in Fig. 5.3.

It is well known that the structural PT from Si I to Si II is accompanied by an electronic transition from semiconducting to metallic phase. However, the relation between the structural and electronic properties was not established. Here, we found that electronic PT precedes the structural PT for all combinations of stresses. That means that under stresses there is metallic deformed Si I. Also, this electronic PT does not change smoothness of the stress-strain curves (Fig. 5.3); this differs from the stress discontinuity in magneto-structural phase transitions (e.g., in iron (100)). The metallization curve is closed in the (σ_3, σ_1) plane and can be approximated by two straight lines $\sigma_{3m} = -5.605 + 0.8417\sigma_1$ and $\sigma_{3m} = 13.04 + 1.396\sigma_1$, and parabolic section $\sigma_{3m} = 11.95 + 2.378\sigma_1 + 0.16\sigma_1^2$. Metallization can be caused by compressive and tensile stresses (or their combination). While one of the metallization lines is relatively close and approximately parallel to the Si I→Si II PT line, the semiconducting (non-metallic) region is compact and its closed boundary surrounds the stress-free Si I. According to Fig. 5.3, metallization occurs deeply in the region of stability of Si I. Under hydrostatic condition metallization occurs at compressive 36.82 GPa and tensile 13.91 GPa. Under uniaxial loading metallization takes place at compressive 5.4 GPa and tensile 12.78 GPa, i.e. the effect of nonhydrostatic stresses is extremely strong. Under biaxial loading at $\sigma_3 = 0$ electronic transition happens at compressive 6.69 GPa and tensile 8.792 GPa. Intersection of the metallization curve with line for elastic instability of Si II in the stress plane in Fig. 5.3 does not have any meaning because strains for metallization correspond to the region of stability of Si I (compare Figs. 6.1 and 3.6).

3.7 Elastic lattice instability under triaxial loading

Results for more general case $\sigma_1 \neq \sigma_2$ are presented in Fig. 4.4. Evidently, DFT results suggest that criterion for direct Si I→Si II PT with a reasonable accuracy can be described in 3D space of normal stresses by a plane

$$\sigma_3 = -9.911 + 0.4145(\sigma_1 + \sigma_2). \tag{1}$$

It is very surprising that the elastic lattice instability for a material with strong physical and geometric nonlinearities can be approximated by a linear criterion.

3.8 Lattice instability under stress tensor: the phase field approach

As it was shown in (49; 52; 53), a linear in normal stress PT condition can be derived within the phase field approach to martensitic PTs. Using several steps and assumptions, the following instability criterion for Si I→Si II PT was derived:

$$2W = \sigma{:}F_e^{T-1} \cdot \frac{d^2\bar{U}_t}{d\eta^2}\Big|_{\eta=0} \cdot F_e^T \geq 2A, \tag{2}$$

where the transformation strain $\bar{\varepsilon}_t(\eta)$, the transformation deformation gradient $\bar{U}_t(\eta) \equiv I + \bar{\varepsilon}_t(\eta)$, and other material parameters (e.g., thermal energy, elastic moduli, etc.) depend on the order parameter η, which changes during the transformation process from $\eta = 0$ for Si I [i.e., $\bar{U}_t(0) = I$ and $\bar{\varepsilon}_t(0) = 0$] to $\eta = 1$ for Si II [i.e., $\bar{U}_t(1) = U_t$ and $\bar{\varepsilon}_t(1) = \varepsilon_t = diag(\varepsilon_{t1}, \varepsilon_{t1}, \varepsilon_{t3})$]. W is called in (52) the modified transformation work, and A is the magnitude of the double-well barrier. For cubic to tetragonal transformation, $\frac{d^2\bar{U}_t}{d\eta^2}\Big|_{\eta=0} = 2diag(b_1\varepsilon_{t1}, b_1\varepsilon_{t1}, b_3\varepsilon_{t3})$, where b_i are the coefficients in the interpolation functions for $\bar{\varepsilon}_t(\eta)$ to be determined. For the loading by three stresses normal to the chosen above faces, all tensors in Eq. (2) are coaxial, tensors F_e^{T-1} and F_e^T eliminate each other, and Eq. (2) reduces to the linear modified transformation work criterion:

$$W = b_3\sigma_3\varepsilon_{t3} + b_1(\sigma_1 + \sigma_2)\varepsilon_{t1} = A. \tag{3}$$

We changed inequality to equality in order to describe combination of stress at the limit of stability and calibrate material parameters. W reduces to the transformation work for $b_1 = b_3 = 1$. The key

consequence of Eq.(3) for cubic to tetragonal PT is that since $\varepsilon_{t1} = \varepsilon_{t2}$, stresses σ_1 and σ_2 contribute to the instability criterion via $\sigma_1 + \sigma_2$, i.e., like in Eq.(1). Comparing Eqs. (3) and (1) with allowing for values of $\varepsilon_{t1} = U_{t1} - 1 = 0.243$ and $\varepsilon_{t3} = U_{t3} - 1 = -0.514$ leads to $A(\theta)/b_3 = 5.094\,\mathrm{GPa}$ and $b_3/b_1 = 1.141$.

When shear stresses τ_{ij} are applied, causing nonzero deformation gradients F_{21}, F_{31}, F_{32}, but rigid body rotations are excluded by imposing a constraint $F_{12} = F_{13} = F_{23} = 0$, Eq. (2) reduces to

$$W = b_3\sigma_3\varepsilon_{t3} + b_1(\sigma_1 + \sigma_2)\varepsilon_{t1} + \frac{b_1\varepsilon_{t1} - b_3\varepsilon_{t3}}{F^e_{11}F^e_{22}}\left[\tau_{32}F^e_{32}F^e_{11} + \tau_{31}(F^e_{31}F^e_{22} - F^e_{32}F^e_{21})\right] = A, \tag{4}$$

where $(b_1\varepsilon_{t1} - b_3\varepsilon_{t3})/A = 0.143$ and the terms proportional to $\varepsilon_{t2} - \varepsilon_{t1}$ are eliminated. Since transformation shears are absent in a cubic to tetragonal PT, the shear transformation work is absent. The terms proportional to the shear stresses are due to geometric nonlinearity (finite strains); they do not contain any additional material parameters. Shear stresses change geometry of the crystal, and this affects transformation work along the normal components of transformation strain.

Note that Eq. (4) is not invariant under exchange $1 \leftrightarrow 2$ because of imposed kinematic constraint. For the obtained parameters, and because $F^e_{ii} > 0$ and $\tau_{ij}F^e_{ij} > 0$, when τ_{32} and F^e_{32} or τ_{31} and F^e_{31} are applied alone, contribution of shear stresses to W is positive, i.e., they promote tetragonal instabilities. Shear stress τ_{21} (more exactly, elastic shear strain F^e_{21}) alone and with τ_{32} does not contribute to the instability condition. Shear stress τ_{21} contributes to the instability condition when two other stresses, τ_{31} and τ_{32}, are applied simultaneously, and depending on signs of all shear stresses, τ_{21} may promote or suppress tetragonal instability.

3.9 Shear stress-strain curves and shear lattice instability

Increasing simple shears F_{21}, F_{31}, F_{32} and their combinations were applied at various fixed $F_{11} = F_{22}$ ($2 - 3\%$ before and after tetragonal instability points) and F_{33}, for which stresses

$\sigma_1 = \sigma_2$ were equal to the shown in Fig. 3.8 value before shear loading. Typical shear stress τ_{31} – deformation gradient F_{31} curves are shown in Fig. 3.8. Shear instability starts at the maximum shear stress. This instability does not lead to Si II but rather to possible amorphization or hexagonal diamond Si IV, that is why we will not focus on it here. Our goal is to study the effect of shear stresses on the tetragonal mode of instability leading to the PT to Si II, which makes sense before shear instability is reached.

Under an initial (before shear) hydrostatic compression, shear stresses for any F_{31} in the cubic phase reduce with increasing volumetric strain and pressure (see curves for four lower combinations of F_3 and F_1 in the legend in Fig. 3.8 (a)), which is qualitatively consistent with the limited results in (80) for the $[11\bar{2}](111)$ slip system. After reaching the instability pressure for Si I to Si II PT and following the tetragonal branch of deformation gradient (see curves for three upper combinations of F_3 and F_1 in the legend in Fig. 3.8 (a)), a crossover is observed and a shear stress for any F_{31} increases with further growth of F_3 and volumetric strain, while the pressure reduces along the unstable branch of pressure – E_3 (or volumetric strain) curve. Shear instability at an infinitesimal shear starts at 72 GPa, i.e., below the tetragonal mode of lattice instability. This may explain amorphization in nanocrystalline Si I under increasing pressure when PT to Si II is kinetically suppressed (17). Amorphization may be caused by virtual melting (48) after crossing metastable continuation of the melting line, since melting temperature for Si reduces with pressure.

The effect of pressure on the $\tau_{21} - F_{21}$ curves is qualitatively similar to that for the $\tau_{31} - F_{31}$ curves. However, shear instability for any $F_{21} \leq 0.25$ starts after tetragonal instability only.

At a nonhydrostatic initial loading, physics is essentially different. At the initial stress $\sigma_1 = \sigma_2 = -69.61\,\text{GPa}$, shear instability for an infinitesimal F_{31} starts practically simultaneously with the tetragonal instability (see curve for the middle values of F_3 and F_1 in the legend in Fig. 3.8 (b)). Before tetragonal instability, the shear instability shifts to larger shears. Shear stress τ_{31} decreases with increasing $|E_3|$ monotonously, in contrast to hydrostatic loading. At the same time, shear instability occurs for $F_{21} > 0.2$ after tetragonal instability. Both τ_{31} and τ_{21} decrease with increasing $|E_3|$; for all $|E_3|$ and equal shears one has $\tau_{31} < \tau_{21}$. This tendency in stress-strain

curves is kept to $\sigma_1 = \sigma_2 = -39.63\,\text{GPa}$ with increasing shear instability strain F_{31} and without essential change in the instability strain F_{21}. Amplitude of both shear stresses increases with reducing $|\sigma_1| = |\sigma_2|$. Effect of lateral F_1 and corresponding axial F_3 compressions on both shear stress-strain curves reduces with decreasing $|\sigma_1| = |\sigma_2|$. At $|\sigma_1| = |\sigma_2| = 29.68\,\text{GPa}$ a crossover occurs, i.e., shear stresses slightly increase with $|E_3|$.

3.10 Effect of shear stresses on tetragonal instability

The $\sigma_3 - E_3$ curves [along the path in the $(F_1 = F_2, F_3)$ plane corresponding to $\sigma_1 = \sigma_2$ before shear] have been obtained for different fixed shears. The instability stress in Fig. 3.9 is determined as the local maximum of $|\sigma_3|$, see Fig. 3.4. While during shear $\sigma_1 \neq \sigma_2$ but their sum $\sigma_1 + \sigma_2$ practically does not change. That is why curves in Fig. 3.9 are given for the approximately fixed values of $(\sigma_1 + \sigma_2)/2$.

In addition, absolute and relative deviations between the actual instability stress σ_3 and σ_3^{an} based on the analytical prediction (4) are presented in Figs. 3.10 and 3.11. As we already discussed, shear stress τ_{21} alone does not contribute to the analytical instability condition (4) and the simplest linear Eq. (3) can be used. As can be seen, τ_{21} practically (within the relative error of 6%) does not affect the instability stress σ_3 in a broad range of shear stress τ_{21} below the shear instability, which is approximately described by $\tau_{21}^{in} = 11.09 + 0.1470\sigma_1$. Shear instability stress τ_{21} varies from 11.09 GPa at $\sigma_1 = 0$ to 0 at $\sigma_1 \simeq -75.44\,\text{GPa}$.

An increasing shear stress τ_{31} causes some reduction in the instability stress σ_3 (Fig. 3.9). The relative error of the instability stress with respect to the analytical prediction Eq.(4) for most combinations of of τ_{31} and $(\sigma_1 + \sigma_2)/2$ is between $+4\%$ and -6%. However, there are three points outside this range for a large shear stress $\tau_{31} > 8.5\,\text{GPa}$. At these points, stresses $-(\sigma_1 + \sigma_2)/2$ are small (from to -2 to $10GPa$) and the corresponding instability stress $-\sigma_3$ is also small (10–18 GPa); a ratio of smaller numbers with finite absolute errors has a larger relative error. The absolute error $\sigma_3 - \sigma_3^{an}$ for these points is just within $\pm 1\,\text{GPa}$, see Fig. 3.11. A larger error of $\pm 2\,\text{GPa}$ appears

for small shear stresses but large $-\sigma_1$ and consequently $-\sigma_3$ (from 50 to 75 GPa), i.e., close to the shear instability. A relative error there remains within $\pm 4\%$.

Thus, the main effect of a shear stress τ_{31} on the instability stress σ_3 is due to the theoretically predicted geometric nonlinearity with zero linear term. The combined effect of two and three shear stresses on the instability stress σ_3 is smaller than the effect of τ_{31} alone (a) because of smaller averaged shear stress that causes shear instability and (b) because of small contribution of τ_{21} for two shear stresses and opposite contribution of τ_{21} for three stresses, according to Eq. 4 for all positive shear stresses. Deviation from the prediction (4) does not exceed $\pm 4\%$. Thus, tetragonal lattice instability under action of all six components of the stress tensor can be described by the critical value of the modified transformation work, namely, by Eq. (4), which (a) is linear in normal stresses, depends on $\sigma_1 + \sigma_2$, and has only two adjustable coefficients (b_1 and b_3); (b) is independent of $\sigma_1 - \sigma_2$ and shear stress τ_{21} acting alone or with one more shear stress; (c) contains a geometric nonlinear term describing contribution of all shear stresses without any additional adjustable parameters.

Note that for a neglected effect of shear stresses, an absolute deviation of σ_3 from the linear expression (3) is within 2 GPa for $\tau_{31} < 5$ GPa and within 3 GPa for $\tau_{31} < 8$ GPa. The relative deviation of σ_3 from the linear expression (3) is within 10% for $\tau_{31} < 8$ GPa.

3.11 Summary

We performed a comprehensive DFT study of the phase transition between semiconducting Si I and metallic Si II under *all six components* of the stress tensor with normal stresses along $\langle 110 \rangle$, $\langle 1\bar{1}0 \rangle$, and $\langle 001 \rangle$ directions. We investigated the stress-strain curves, elastic lattice instabilities, the electronic band gap, and metallization. The key result is that Si I→Si II PT can be described by the critical value of the modified transformation work (Eq. (4)), obtained within a phase field formalism. Thus, with normal stress σ_3 in $\langle 001 \rangle$ direction, the PT criterion is linear in normal stresses, depends on $\sigma_1 + \sigma_2$; is independent of $\sigma_1 - \sigma_2$ and shear stress τ_{21} acting alone or with one more shear stress; contribution of all shear stresses can be described through the theoretically predicted geometric

nonlinear term (without any additional adjustable constants). The PT criterion contains just two adjustable parameters, which can be calibrated by instability stresses at two different stress states without shears. Those parameters can be fitted to DFT results or experiment. Then our criterion accurately describes instability in a broad range of variations of all six components of the stress tensor.

While Si I→Si II PT occurs due to elastic instability, the modified transformation work criterion (2), simplified in Eq. (4), is based on completely different principles and assumptions. In particular, it considers the entire dissipative PT process described by the transformation strain tensor and does not include the terms with a discontinuity in elastic moduli, in order to avoid nonlinearity in normal stresses. Using these paradoxical results, we formulate a problem of finding a fundamental relationship between the elastic instability and the modified transformation work criterion, which will be studied in future works. The elastic instability analysis for the simplest model with quadratic in E energy qualitatively reproduces our main results (50) for relatively low stresses.

The PT pressure under hydrostatic condition is $\approx$20 times larger than under uniaxial loading. Such a strong effect of nonhydrostaticity at least partially explains the significant difference between the experimental PT pressure (9-12 GPa) and the instability pressure of 75.81 GPa, as well as a scatter in the experimental data under quasi-hydrostatic conditions.

Although the stress-strain curve is continuous, the electronic PT precedes the structural PT. That means that under stresses there is a metallic Si I. Metallization can be caused by compressive or tensile stresses, and the effect of nonhydrostatic stresses is extremely strong. In the (σ_1, σ_3) plane in Fig. 5.3 it is described by a closed contour, which can be approximated by two straight lines and a parabolic cap. Only one of the metallization lines is relatively close and approximately parallel to the Si I→Si II PT line. Interestingly, metallization occurs deeply in the region of stability of Si I and is not causing the Si I→Si II structural PT.

Surprisingly, a stress-free Si II is metastable in DFT. Although at zero pressure Si II has a higher enthalpy than Si I, both Si I and Si II correspond to local enthalpy minima (Fig. 3.2) and both have stable phonons (24; 25; 102).

In addition, shear stress-strain curves are obtained for different simple shears and their combinations at different normal stresses. A shear instability competes with a tetragonal instability, which does not lead to Si II, but rather to possible amorphization or hexagonal diamond Si IV. Pressure and compressive normal stresses reduce shear stresses below and at the shear instability strain. Under hydrostatic or near-hydrostatic conditions, shear instability in Si I occurs earlier than tetragonal instability, which may result in amorphization. This may explain amorphization in nanocrystalline Si I under increasing pressure when PT to Si II is kinetically suppressed (17). Amorphization may be caused by virtual melting (48) after crossing metastable continuation of the melting line, since melting temperature for Si reduces with pressure. Competition of the instability stresses rather than the relative energy minima can serve as a basis for phase selection. Instability criteria can be used for developing methods for search for new phases under complex loading.

Obtained results can be used for significant advancing and calibrating large-strain phase field models, e.g., in (49; 52). Then they can be utilized for quantitative studies of the interaction between crystal defects and PTs, as it was done in (54; 35) for a model material. This will enable finding the ways to reduce PT pressure due to nonhydrostatic stresses and plastic strains by an order of magnitude and more (47; 1; 7; 20). Such a reduction is crucial for synthesis of known and new high-pressure phases at practically achievable pressure level, suitable for discovery of novel materials and transformation of science into technologies. This also will quantitatively rationalize connection between PT conditions for ideal and real (defective) crystals.

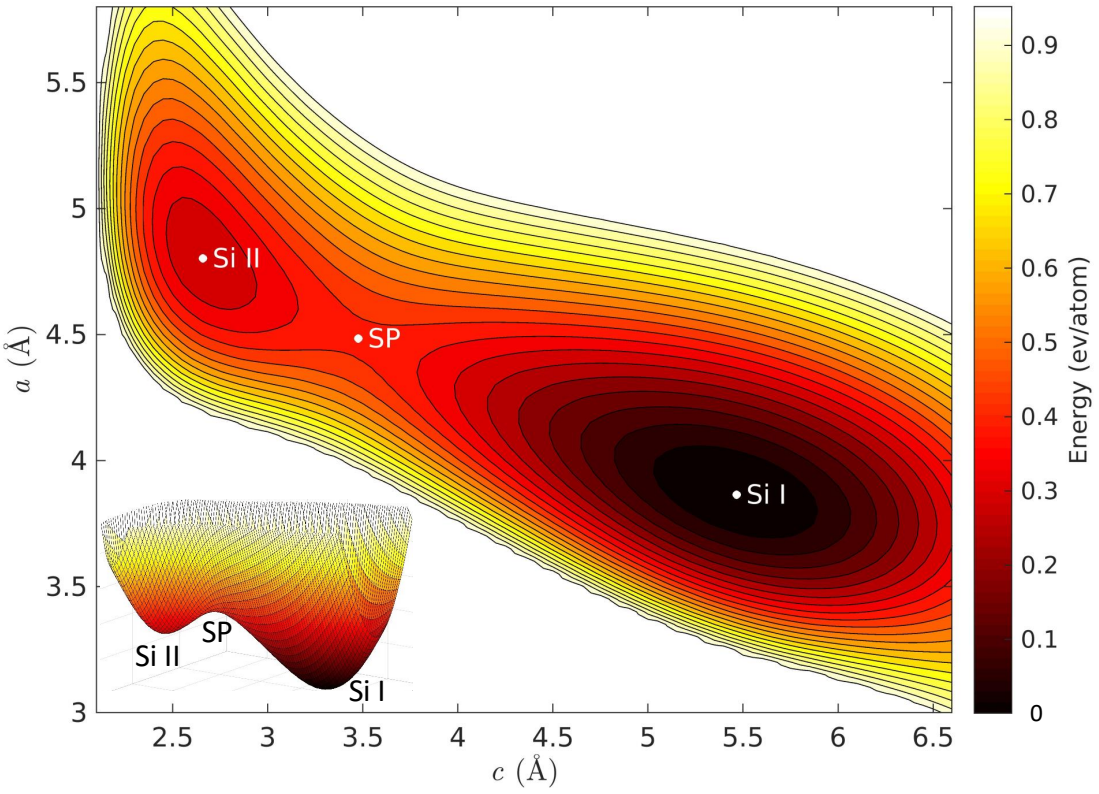

Figure 3.2 Energy landscape of Si versus lattice parameters c and a, calculated using DFT.

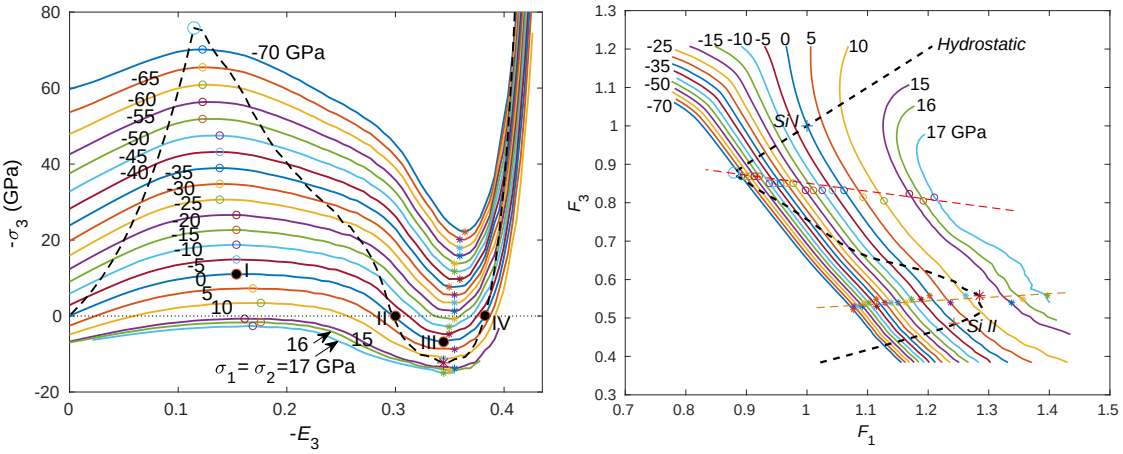

Figure 3.3 (a) True (Cauchy) stress σ_3 - Lagrangian strain E_3 curves for compression/tension in c direction for various fixed lateral stresses $\sigma_1 = \sigma_2$ in a and b directions for Si I↔Si II PTs and (b) corresponding transformation paths in $(F_1 = F_2, F_3)$ plane. Hollow symbols mark elastic instability points for direct PT and solid points designate elastic instability for reverse PT. Dashed line is stress-strain curve for hydrostatic loading.

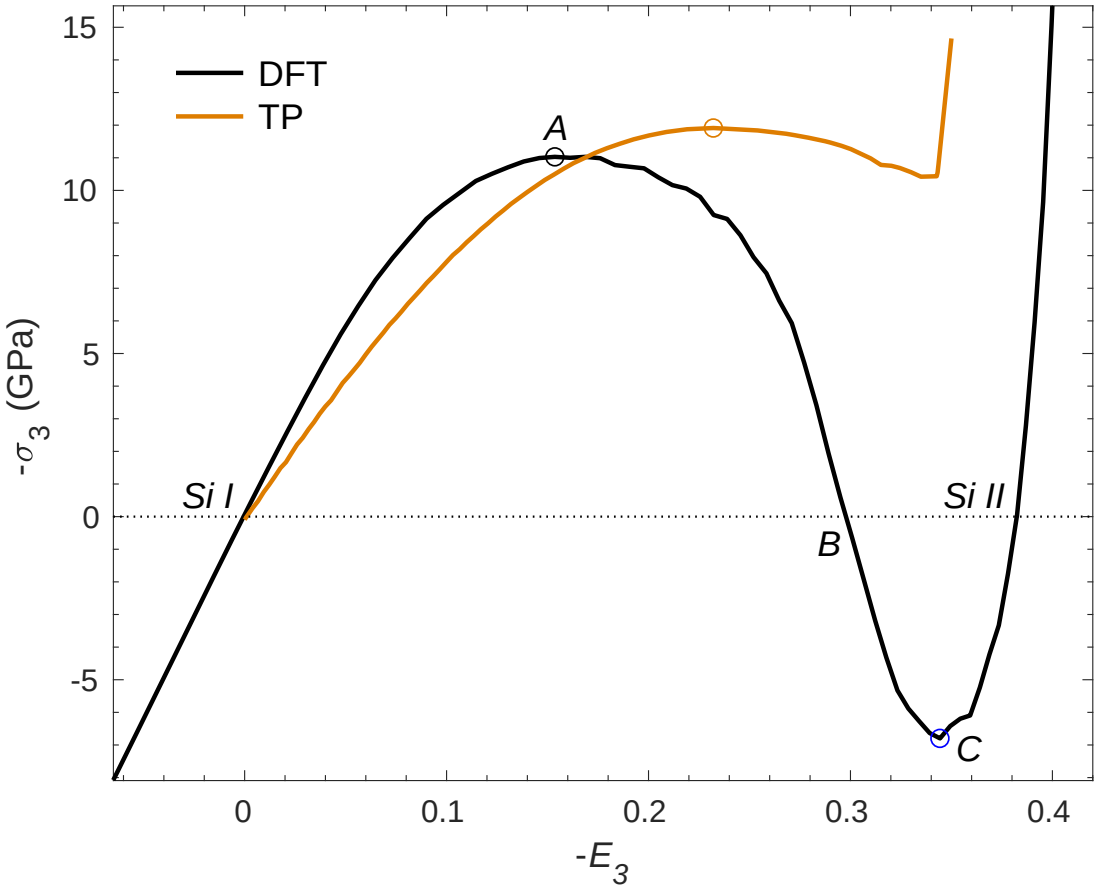

Figure 3.4 Comparison of the Cauchy stress σ_3 - Lagrangian strain E_3 curves for a uniaxial compression in c direction at fixed lateral stresses $\sigma_1 = \sigma_2 = 0$ for Si I↔Si II PTs, obtained from DFT and TP-based simulations.

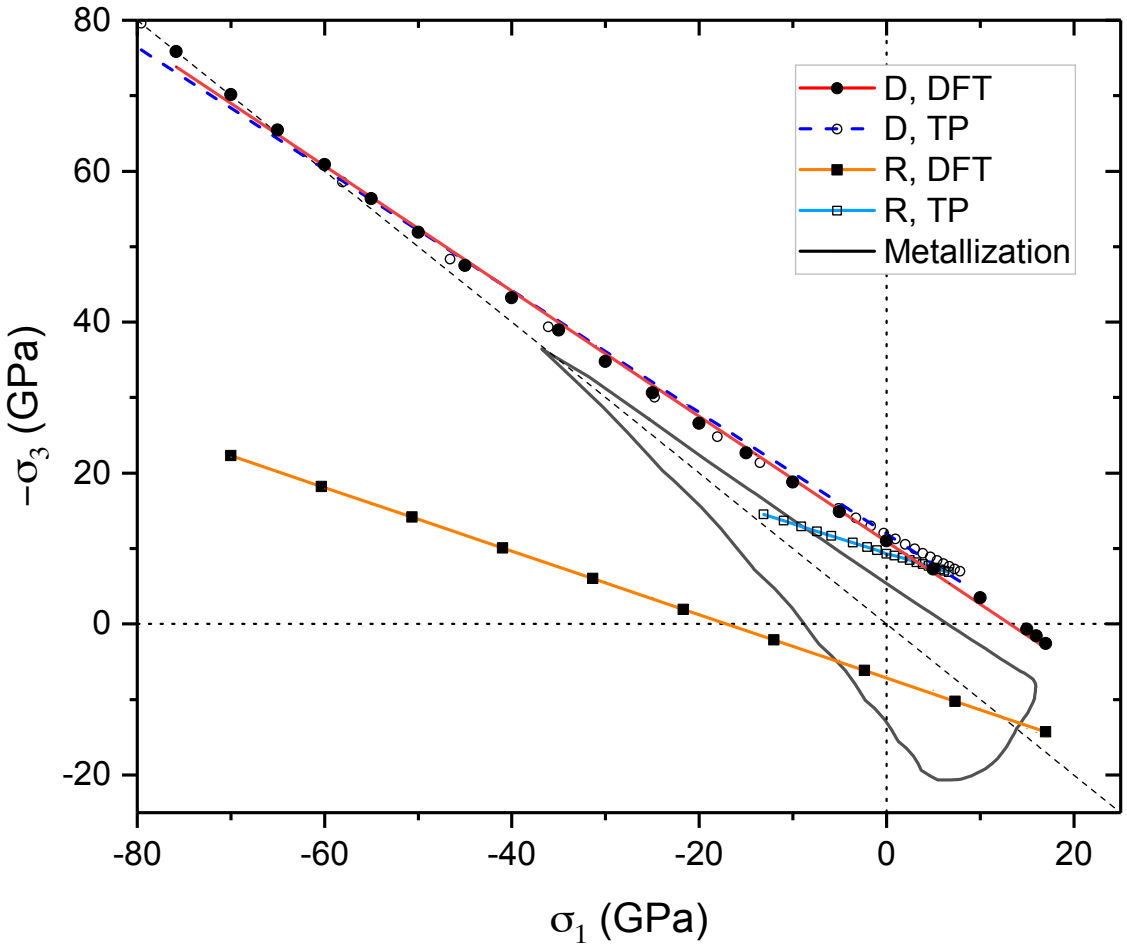

Figure 3.5 Elastic lattice instability in terms of stresses σ_3 and $\sigma_1 = \sigma_2$ for direct (D) Si I→Si II and reverse (R) Si II→Si I PTs from DFT and TP-based results (52; 53), and metallization curve from DFT. The hydrostatic condition $\sigma_1 = \sigma_2 = \sigma_3$ is shown by diagonal dashed black line.

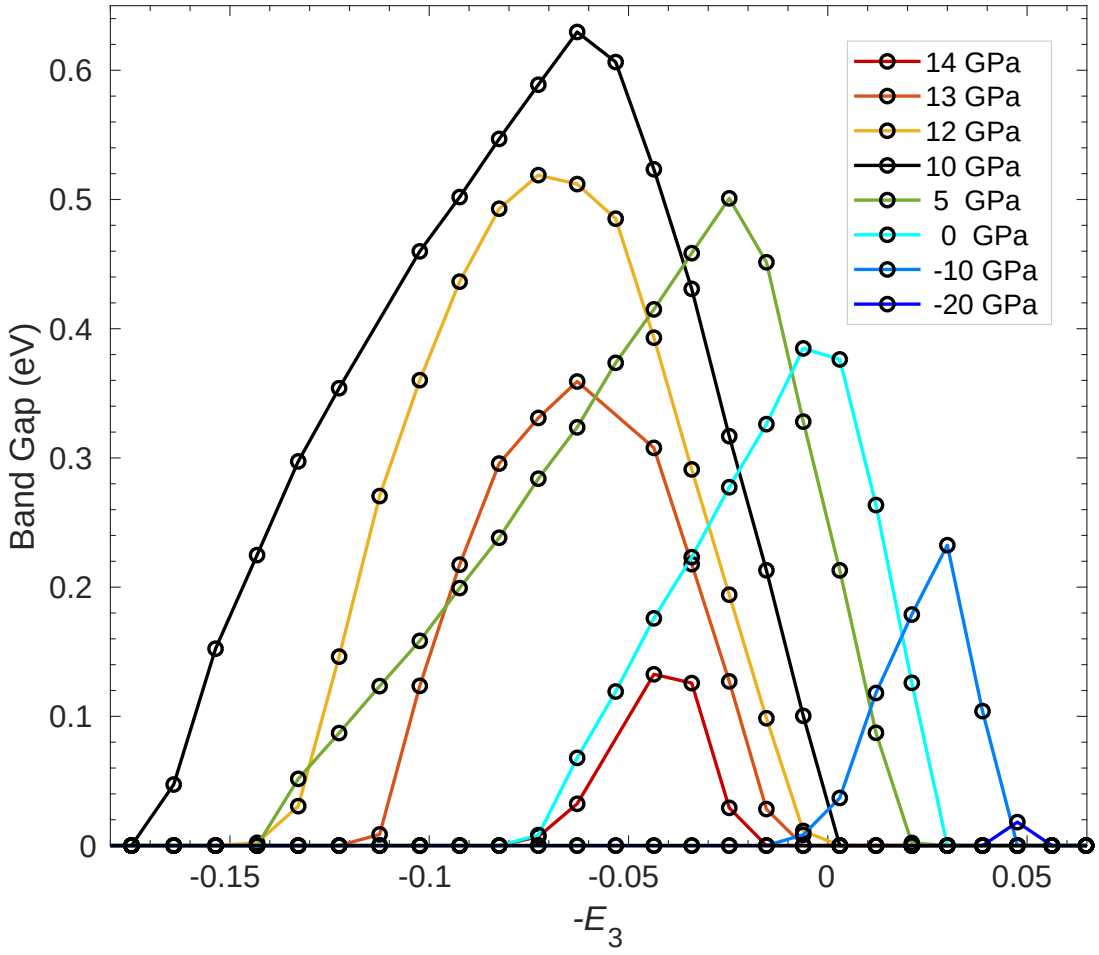

Figure 3.6 Electronic band gap width in deformed Si I vs. strain E_3 at various fixed $\sigma_1 = \sigma_2$, ranging from -14 to $+20$ GPa.

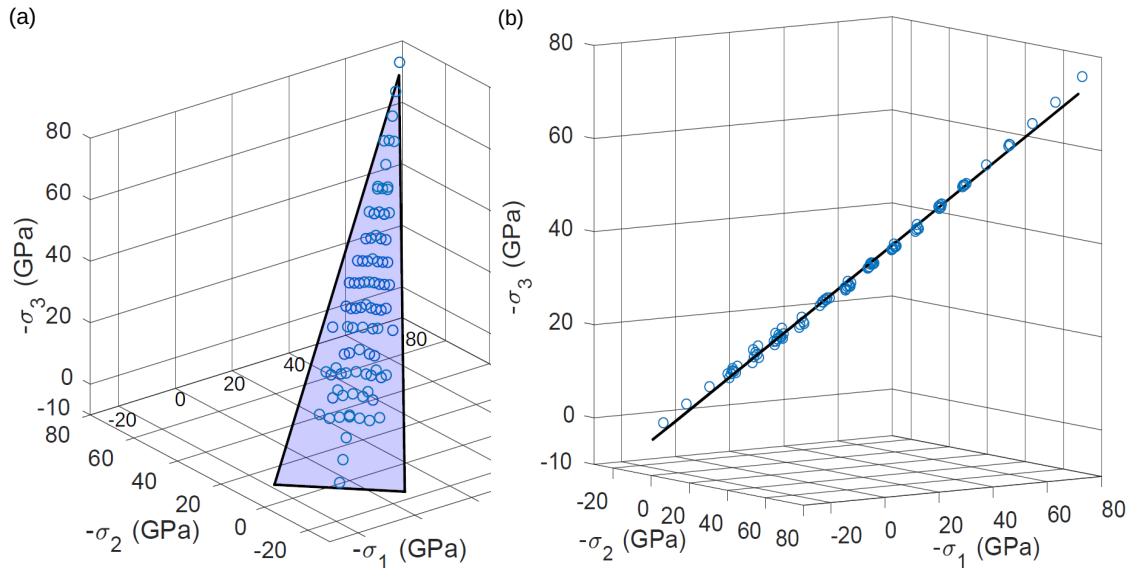

Figure 3.7 Criterion for Si I→Si II PT in the space of three normal stresses. (A) Points are obtained using DFT simulations and plane is the best fit, which corresponds to the constant value of the modified transformation work Eq. (2). (B) The same results like in (A) but plot is rotated until approximating plane is visible as a line. It is clear that DFT points are very close to the modified transformation work plane.

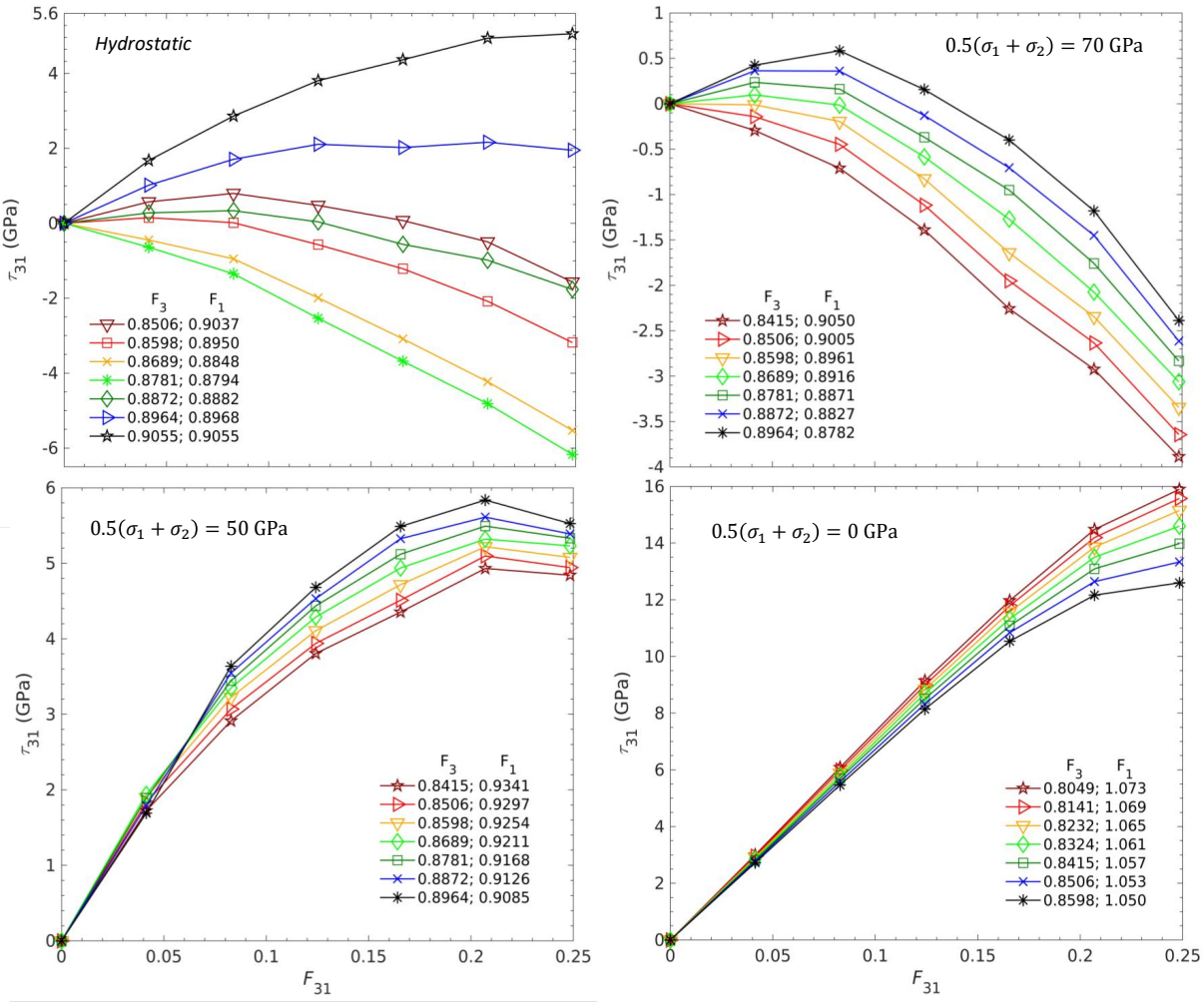

Figure 3.8 Shear stress τ_{31} - deformation gradient F_{31} curves at various fixed $F_1 = F_2$ ($2-3\%$ before and after tetragonal instability points) and F_3. Plots are for initially hydrostatic loading and for loading with stresses $\sigma_1 = \sigma_2$, which were equal to the shown in plot values, both before shear loading. Due to geometric nonlinearity, normal stresses vary with increasing shears but $0.5(\sigma_1 + \sigma_2) \simeq const$. In the legends: middle values of F_3 and F_1 correspond to the tetragonal instability points without shear stresses; three values of F_3 and F_1 below the middle value correspond to the Si I before tetragonal instability point; three values of F_3 and F_1 above the middle value are after the tetragonal instability point.

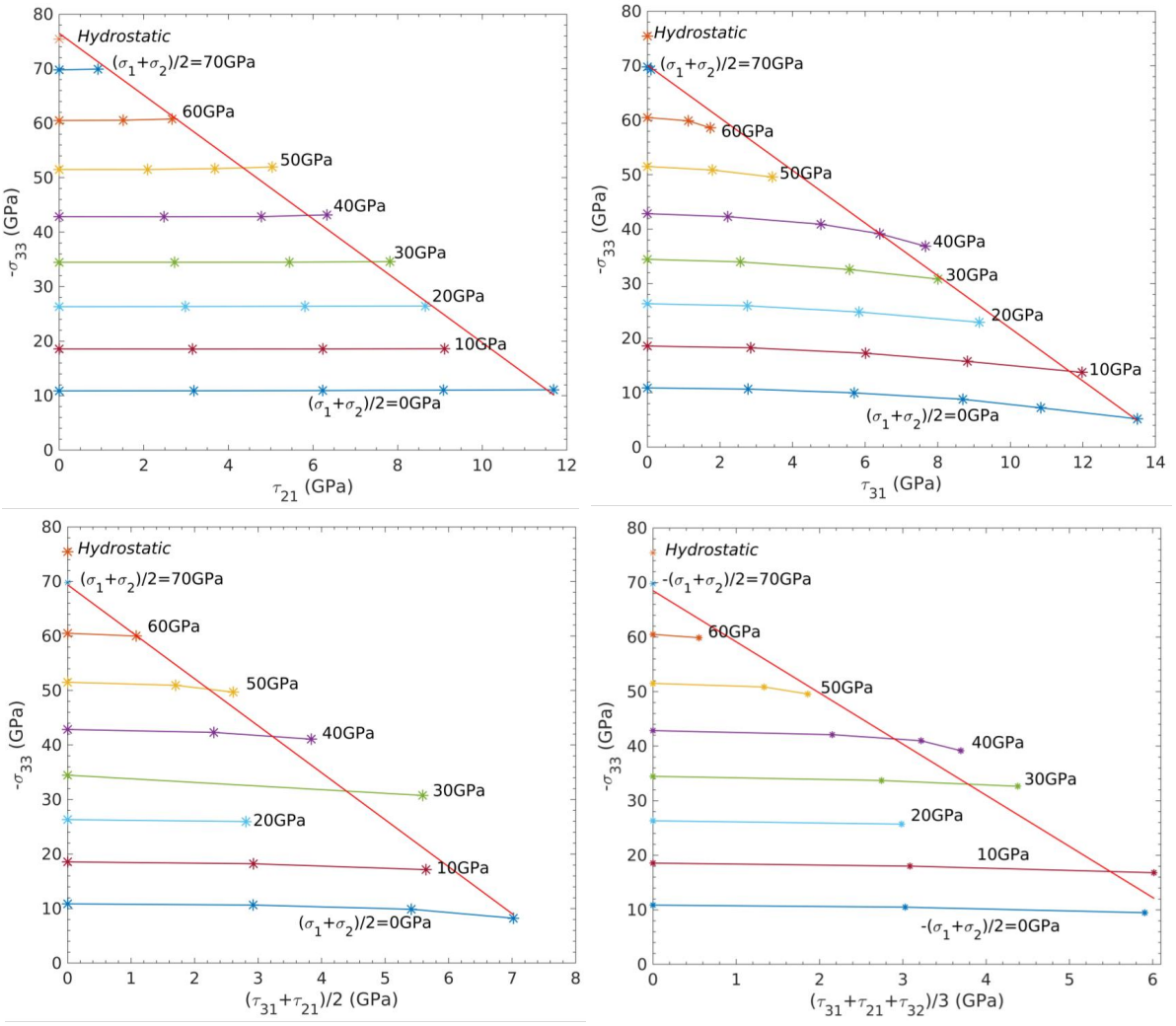

Figure 3.9 The effect of various combinations of shear stresses on the tetragonal instability stress σ_3 for different $\sigma_1 = \sigma_2$. Points with largest shear stress approximately correspond to shear instability. Straight inclined lines are linear approximations of the relationship between σ_3 and shear stresses for shear instability.

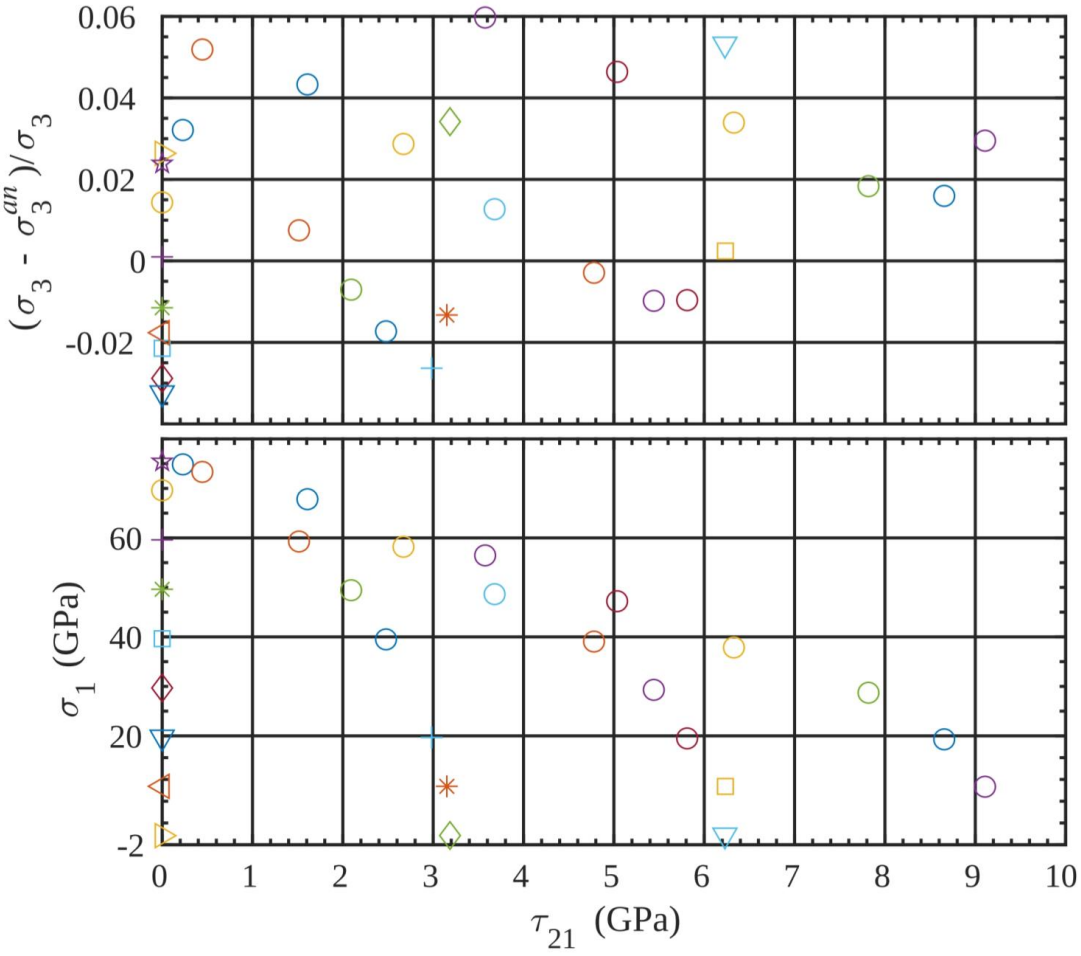

Figure 3.10 Relative difference between the actual instability stress σ_3 and the instability stress σ_3^{an} based on analytical prediction Eq.(4) and corresponding values of $-(\sigma_1 + \sigma_2)/2$ versus shear stress τ_{21}.

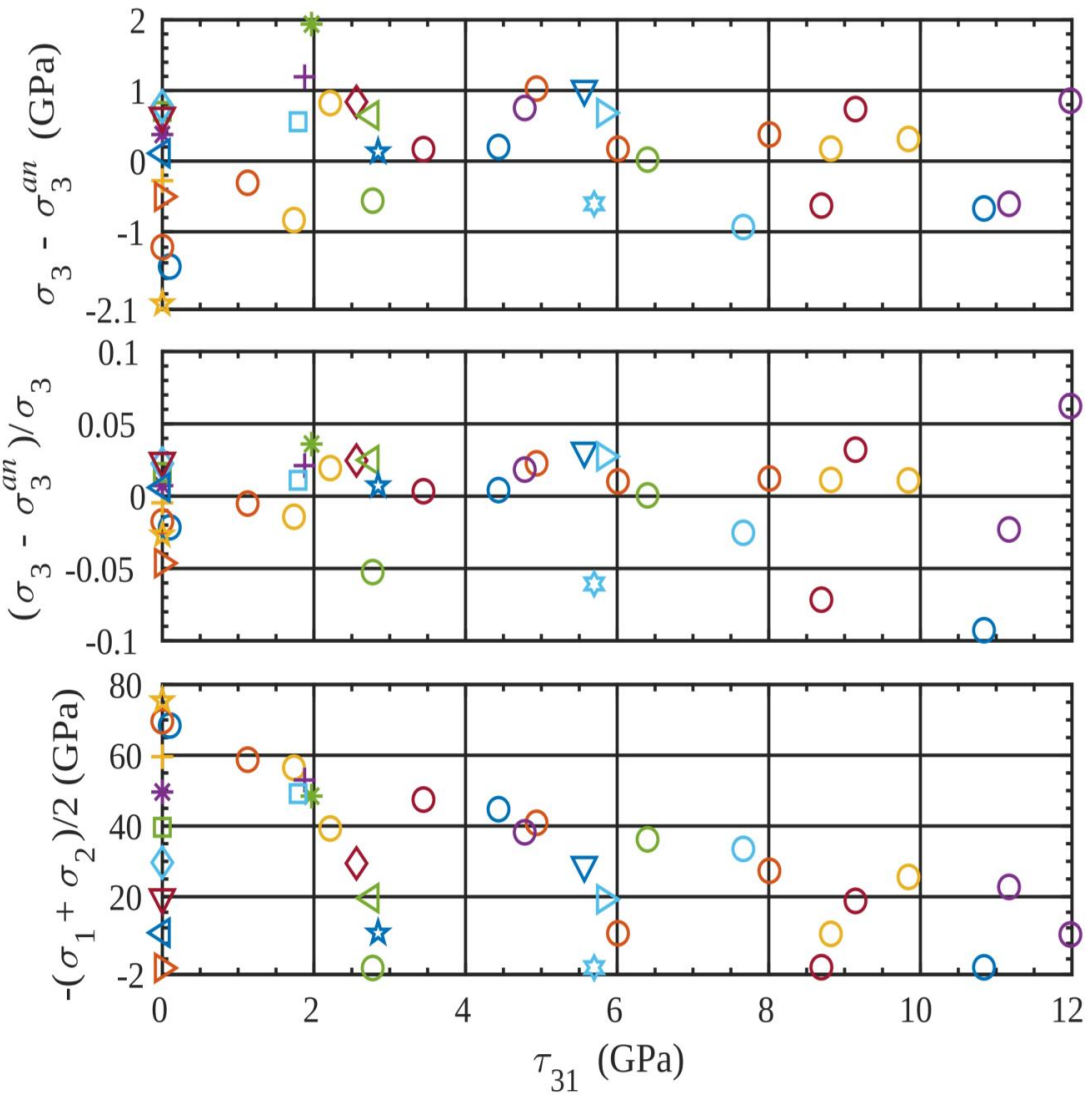

Figure 3.11 Absolute and relative difference between the actual instability stress σ_3 and the instability stress σ_3^{an} based on analytical prediction Eq.(4) and corresponding values of $-(\sigma_1 + \sigma_2)/2$ versus shear stress τ_{31}.

Bibliography

[1] Alippi, P., Marcus, P., and Scheffler, M. (1997). Strained tetragonal states and bain paths in metals. *Physical review letters*, 78(20):3892.

[2] Amodeo, R. and Ghoniem, N. (1990a). Dislocation dynamics. ii. applications to the formation of persistent slip bands, planar arrays, and dislocation cells. *Physical Review B*, 41(10):6968.

[3] Amodeo, R. J. and Ghoniem, N. M. (1990b). Dislocation dynamics. i. a proposed methodology for deformation micromechanics. *Physical Review B*, 41(10):6958.

[4] Atwater, H. A. and Brown, W. L. (1990). Grain boundary mediated amorphization in silicon during ion irradiation. *Applied Physics Letters*, 56(1):30–32.

[5] Baillin, X., Pelissier, J., Bacmann, J., Jacques, A., and George, A. (1987). Dislocation transmission through= 9 symmetrical tilt boundaries in silicon and germanium: I. in situ observations by synchrotron x-ray topography and high-voltage electron microscopy. *Philosophical Magazine A*, 55(2):143–164.

[23] Balamane, H., Halicioglu, T., and Tiller, W. (1992). Comparative study of silicon empirical interatomic potentials. *Physical Review B*, 46(4):2250.

[7] Biyikli, E. and To, A. C. (2017). Multiresolution molecular mechanics: Implementation and efficiency. *Journal of Computational Physics*, 328:27–45.

[1] Blank, V. D. and Estrin, E. I. (2013). *Phase transitions in solids under high pressure*. CRC Press.

[9] Blöchl, P. E. (1994). Projector augmented-wave method. *Physical review B*, 50(24):17953.

[10] Broughton, J. Q., Abraham, F. F., Bernstein, N., and Kaxiras, E. (1999). Concurrent coupling of length scales: methodology and application. *Physical review B*, 60(4):2391.

[14] Cai, W., Bulatov, V. V., Chang, J., Li, J., and Yip, S. (2004). Dislocation core effects on mobility. *Dislocations in solids*, 12:1–80.

[12] Cai, W., de Koning, M., Bulatov, V. V., and Yip, S. (2000). Minimizing boundary reflections in coupled-domain simulations. *Physical Review Letters*, 85(15):3213.

[13] Černỳ, M., Řehák, P., Umeno, Y., and Pokluda, J. (2012). Stability and strength of covalent crystals under uniaxial and triaxial loading from first principles. *Journal of Physics: Condensed Matter*, 25(3):035401.

[6] Chen, X., Xiong, L., Chernatynskiy, A., and Chen, Y. (2014). A molecular dynamics study of tilt grain boundary resistance to slip and heat transfer in nanocrystalline silicon. *Journal of Applied Physics*, 116(24):244309.

[15] Chen, Y. (2006). Local stress and heat flux in atomistic systems involving three-body forces. *The Journal of chemical physics*, 124(5):054113.

[16] Chen, Y. (2009). Reformulation of microscopic balance equations for multiscale materials modeling. *The Journal of chemical physics*, 130(13):134706.

[17] Deb, S. K., Wilding, M., Somayazulu, M., and McMillan, P. F. (2001). Pressure-induced amorphization and an amorphous–amorphous transition in densified porous silicon. *Nature*, 414(6863):528.

[18] Deng, Q. and Chen, Y. (2013). A coarse-grained atomistic method for 3d dynamic fracture simulation. *International Journal for Multiscale Computational Engineering*, 11(3).

[19] Domnich, V., Ge, D., and Gogotsi, Y. (2004). Indentation-induced phase transformations in semiconductors. *High Pressure Surface Science and Engineering*, pages 381–442.

[20] Edalati, K. and Horita, Z. (2016). A review on high-pressure torsion (hpt) from 1935 to 1988. *Materials Science and Engineering: A*, 652:325–352.

[21] Einarsdotter, K., Sadigh, B., Grimvall, G., and Ozoliņš, V. (1997). Phonon instabilities in fcc and bcc tungsten. *Physical review letters*, 79(11):2073.

[22] Elliott, R. S., Triantafyllidis, N., and Shaw, J. A. (2011). Reversible stress-induced martensitic phase transformations in a bi-atomic crystal. *Journal of the Mechanics and Physics of Solids*, 59(2):216–236.

[23] Gaál-Nagy, K., Schmitt, M., Pavone, P., and Strauch, D. (2001a). Ab initio study of the high-pressure phase transition from the cubic-diamond to the β-tin structure of si. *Computational materials science*, 22(1-2):49–55.

[24] Gaál-Nagy, K., Schmitt, M., Pavone, P., and Strauch, D. (2001b). Ab initio study of the high-pressure phase transition from the cubic-diamond to the β-tin structure of si. *Computational materials science*, 22(1-2):49–55.

[25] Gaál-Nagy, K. and Strauch, D. (2006). Phonons in the β-tin, i m m a, and sh phases of silicon from ab initio calculations. *Physical Review B*, 73(1):014117.

[26] Ge, D., Domnich, V., and Gogotsi, Y. (2003). High-resolution transmission electron microscopy study of metastable silicon phases produced by nanoindentation. *Journal of applied physics*, 93(5):2418–2423.

[27] Grimvall, G., Magyari-Köpe, B., Ozoliņš, V., and Persson, K. A. (2012a). Lattice instabilities in metallic elements. *Reviews of Modern Physics*, 84(2):945.

[28] Grimvall, G., Magyari-Köpe, B., Ozoliņš, V., and Persson, K. A. (2012b). Lattice instabilities in metallic elements. *Reviews of Modern Physics*, 84(2):945.

[29] Grinfeld, M. (1991). *Thermodynamic Methods in the Theory of Heterogeneus Systems*. Longman Scientific and Technical.

[26] Hahn, E., Zhao, S., Bringa, E., and Meyers, M. (2016). Supersonic dislocation bursts in silicon. *Scientific reports*, 6:26977.

[31] He, Y., Zhong, L., Fan, F., Wang, C., Zhu, T., and Mao, S. X. (2016). In situ observation of shear-driven amorphization in silicon crystals. *Nature nanotechnology*.

[32] Hill, R. and Milstein, F. (1977). Principles of stability analysis of ideal crystals. *Physical Review B*, 15(6):3087.

[15] Hull, D. and Bacon, D. J. (2001). *Introduction to dislocations*. Butterworth-Heinemann.

[10] Javanbakht, M. and Levitas, V. I. (2016a). Phase field approach to dislocation evolution at large strains: Computational aspects. *International Journal of Solids and Structures*, 82:95–110.

[35] Javanbakht, M. and Levitas, V. I. (2016b). Phase field simulations of plastic strain-induced phase transformations under high pressure and large shear. *Physical Review B*, 94(21):214104.

[7] Ji, C., Levitas, V. I., Zhu, H., Chaudhuri, J., Marathe, A., and Ma, Y. (2012). Shear-induced phase transition of nanocrystalline hexagonal boron nitride to wurtzitic structure at room temperature and lower pressure. *Proceedings of the National Academy of Sciences*, 109(47):19108–19112.

[8] Jin, Z.-H., Gumbsch, P., Albe, K., Ma, E., Lu, K., Gleiter, H., and Hahn, H. (2008). Interactions between non-screw lattice dislocations and coherent twin boundaries in face-centered cubic metals. *Acta Materialia*, 56(5):1126–1135.

[7] Jin, Z.-H., Gumbsch, P., Ma, E., Albe, K., Lu, K., Hahn, H., and Gleiter, H. (2006). The interaction mechanism of screw dislocations with coherent twin boundaries in different face-centred cubic metals. *Scripta Materialia*, 54(6):1163–1168.

[39] Johnson, D. D. (1988). Modified broydens method for accelerating convergence in self-consistent calculations. *Physical Review B*, 38(18):12807.

[40] Klein, P. A. and Zimmerman, J. A. (2006). Coupled atomistic–continuum simulations using arbitrary overlapping domains. *Journal of Computational Physics*, 213(1):86–116.

[12] Kohyama, M., Yamamoto, R., and Doyama, M. (1986). Structures and energies of symmetrical¡ 011¿ tilt grain boundaries in silicon. *physica status solidi (b)*, 137(1):11–20.

[42] Kresse, G. and Furthmüller, J. (1996). Efficiency of ab-initio total energy calculations for metals and semiconductors using a plane-wave basis set. *Computational materials science*, 6(1):15–50.

[43] Kresse, G. and Hafner, J. (1993). Ab initio molecular dynamics for liquid metals. *Physical Review B*, 47(1):558.

[44] Kresse, G. and Hafner, J. (1994). Ab initio molecular-dynamics simulation of the liquid-metal–amorphous-semiconductor transition in germanium. *Physical Review B*, 49(20):14251.

[45] Kresse, G. and Joubert, D. (1999). From ultrasoft pseudopotentials to the projector augmented-wave method. *Physical Review B*, 59(3):1758.

[46] Levitas, V. I. (1998). Thermomechanical theory of martensitic phase transformations in inelastic materials. *International Journal of Solids and Structures*, 35(9-10):889–940.

[47] Levitas, V. I. (2004). High-pressure mechanochemistry: conceptual multiscale theory and interpretation of experiments. *Physical Review B*, 70(18):184118.

[48] Levitas, V. I. (2005). Crystal-amorphous and crystal-crystal phase transformations via virtual melting. *Physical review letters*, 95(7):075701.

[49] Levitas, V. I. (2013). Phase-field theory for martensitic phase transformations at large strains. *International Journal of Plasticity*, 49:85–118.

[50] Levitas, V. I. (2017). Elastic model for stress–tensor-induced martensitic transformation and lattice instability in silicon under large strains. *Materials Research Letters*, 5(8):554–561.

[51] Levitas, V. I. (2018). High pressure phase transformations revisited. *Journal of Physics: Condensed Matter*, 30(16):163001.

[52] Levitas, V. I., Chen, H., and Xiong, L. (2017a). Lattice instability during phase transformations under multiaxial stress: Modified transformation work criterion. *Physical Review B*, 96(5):054118.

[53] Levitas, V. I., Chen, H., and Xiong, L. (2017b). Triaxial-stress-induced homogeneous hysteresis-free first-order phase transformations with stable intermediate phases. *Physical review letters*, 118(2):025701.

[54] Levitas, V. I. and Javanbakht, M. (2014a). Phase transformations in nanograin materials under high pressure and plastic shear: nanoscale mechanisms. *Nanoscale*, 6(1):162–166.

[9] Levitas, V. I. and Javanbakht, M. (2014b). Phase transformations in nanograin materials under high pressure and plastic shear: nanoscale mechanisms. *Nanoscale*, 6(1):162–166.

[56] Li, J., Van Vliet, K. J., Zhu, T., Yip, S., and Suresh, S. (2002). Atomistic mechanisms governing elastic limit and incipient plasticity in crystals. *Nature*, 418(6895):307.

[57] Li, J., Zhu, T., Yip, S., Van Vliet, K. J., and Suresh, S. (2004). Elastic criterion for dislocation nucleation. *Materials Science and Engineering: A*, 365(1-2):25–30.

[3] Martinez-Hernandez, M., Kirchner, H., Korner, A., George, A., and Michel, J. (1987). Dislocations at grain boundaries in deformed silicon. *Philosophical Magazine A*, 56(5):641–658.

[59] Miller, R. E., Shilkrot, L., and Curtin, W. A. (2004). A coupled atomistics and discrete dislocation plasticity simulation of nanoindentation into single crystal thin films. *Acta Materialia*, 52(2):271–284.

[60] Miller, R. E. and Tadmor, E. B. (2007). Hybrid continuum mechanics and atomistic methods for simulating materials deformation and failure. *MRS bulletin*, 32(11):920–926.

[61] Miller, R. E. and Tadmor, E. B. (2009). A unified framework and performance benchmark of fourteen multiscale atomistic/continuum coupling methods. *Modelling and Simulation in Materials Science and Engineering*, 17(5):053001.

[62] Milstein, F., Marschall, J., and Fang, H. E. (1995). Theoretical bcc fcc transitions in metals via bifurcations under uniaxial load. *Physical review letters*, 74(15):2977.

[63] Mizushima, K., Yip, S., and Kaxiras, E. (1994). Ideal crystal stability and pressure-induced phase transition in silicon. *Physical Review B*, 50(20):14952.

[64] Monkhorst, H. J. and Pack, J. D. (1976). Special points for brillouin-zone integrations. *Physical review B*, 13(12):5188.

[65] Patten, J. (2004). Ductile regime machining of semiconductors and ceramics. *High Pressure Surface Science and Engineering*.

[66] Perdew, J. P., Burke, K., and Ernzerhof, M. (1996). Generalized gradient approximation made simple. *Physical review letters*, 77(18):3865.

[17] Pizzagalli, L., Godet, J., Guénolé, J., Brochard, S., Holmstrom, E., Nordlund, K., and Albaret, T. (2013). A new parametrization of the stillinger–weber potential for an improved description of defects and plasticity of silicon. *Journal of Physics: Condensed Matter*, 25(5):055801.

[68] Planes, A. and Mañosa, L. (2001). Vibrational properties of shape-memory alloys. In *Solid state physics*, volume 55, pages 159–267. Elsevier.

[18] Plimpton, S. (1995). Fast parallel algorithms for short-range molecular dynamics. *Journal of computational physics*, 117(1):1–19.

[70] Pokluda, J., Černỳ, M., Šob, M., and Umeno, Y. (2015). Ab initio calculations of mechanical properties: Methods and applications. *Progress in Materials Science*, 73:127–158.

[13] Ratanaphan, S., Yoon, Y., and Rohrer, G. S. (2014). The five parameter grain boundary character distribution of polycrystalline silicon. *Journal of materials science*, 49(14):4938–4945.

[72] Schindler, T. and Vohra, Y. K. (1995). A micro-raman investigation of high-pressure quenched graphite. *Journal of Physics: Condensed Matter*, 7(47):L637.

[73] Shilkrot, L., Curtin, W. A., and Miller, R. E. (2002a). A coupled atomistic/continuum model of defects in solids. *Journal of the Mechanics and Physics of Solids*, 50(10):2085–2106.

[74] Shilkrot, L., Miller, R., and Curtin, W. (2002b). Coupled atomistic and discrete dislocation plasticity. *Physical review letters*, 89(2):025501.

[75] Shilkrot, L., Miller, R. E., and Curtin, W. A. (2004). Multiscale plasticity modeling: coupled atomistics and discrete dislocation mechanics. *Journal of the Mechanics and Physics of Solids*, 52(4):755–787.

[76] Solozhenko, V. L. (1995). Boron nitride phase diagram. state of the art. *International Journal of High Pressure Research*, 13(4):199–214.

[19] Stukowski, A. (2009). Visualization and analysis of atomistic simulation data with ovito–the open visualization tool. *Modelling and Simulation in Materials Science and Engineering*, 18(1):015012.

[78] Telyatnik, R., Osipov, A., and Kukushkin, S. (2016). Ab initio modelling of nonlinear elasto-plastic properties of diamond-like c, sic, si, ge crystals upon large strains. *Materials Physics & Mechanics*, 29(1).

[79] Tonkov, E. Y. and Ponyatovsky, E. (2004). *Phase transformations of elements under high pressure*, volume 4. CRC press.

[80] Umeno, Y. and Černỳ, M. (2008). Effect of normal stress on the ideal shear strength in covalent crystals. *Physical Review B*, 77(10):100101.

[81] Van der Giessen, E. and Needleman, A. (1995). Discrete dislocation plasticity: a simple planar model. *Modelling and Simulation in Materials Science and Engineering*, 3(5):689.

[82] Varlamov, S., Dore, J., Evans, R., Ong, D., Eggleston, B., Kunz, O., Schubert, U., Young, T., Huang, J., Soderstrom, T., et al. (2013). Polycrystalline silicon on glass thin-film solar cells: A

transition from solid-phase to liquid-phase crystallised silicon. *Solar Energy Materials and Solar Cells*, 119:246–255.

[83] Wagner, G. J. and Liu, W. K. (2003). Coupling of atomistic and continuum simulations using a bridging scale decomposition. *Journal of Computational Physics*, 190(1):249–274.

[84] Wallin, M., Curtin, W., Ristinmaa, M., and Needleman, A. (2008). Multi-scale plasticity modeling: Coupled discrete dislocation and continuum crystal plasticity. *Journal of the Mechanics and Physics of Solids*, 56(11):3167–3180.

[85] Wang, J., Yip, S., Phillpot, S., and Wolf, D. (1993). Crystal instabilities at finite strain. *Physical Review Letters*, 71(25):4182.

[86] Wang, Y.-C., Zhang, W., Wang, L.-Y., Zhuang, Z., Ma, E., Li, J., and Shan, Z.-W. (2016). In situ tem study of deformation-induced crystalline-to-amorphous transition in silicon. *NPG Asia Materials*, 8(7):e291.

[87] Wu, Y., Huang, H., Zou, J., and Dell, J. (2009). Nanoscratch-induced deformation of single crystal silicon. *Journal of Vacuum Science & Technology B: Microelectronics and Nanometer Structures Processing, Measurement, and Phenomena*, 27(3):1374–1377.

[88] Xiao, S. and Belytschko, T. (2004). A bridging domain method for coupling continua with molecular dynamics. *Computer methods in applied mechanics and engineering*, 193(17-20):1645–1669.

[89] Xiong, L., Chen, X., Zhang, N., McDowell, D. L., and Chen, Y. (2014). Prediction of phonon properties of 1d polyatomic systems using concurrent atomistic–continuum simulation. *Archive of Applied Mechanics*, 84(9-11):1665–1675.

[90] Xiong, L., Rigelesaiyin, J., Chen, X., Xu, S., McDowell, D. L., and Chen, Y. (2016). Coarse-grained elastodynamics of fast moving dislocations. *Acta Materialia*, 104:143–155.

[91] Xiong, L., Tucker, G., McDowell, D. L., and Chen, Y. (2011). Coarse-grained atomistic simulation of dislocations. *Journal of the Mechanics and Physics of Solids*, 59(2):160–177.

[92] Xiong, L., Xu, S., McDowell, D. L., and Chen, Y. (2015). Concurrent atomistic–continuum simulations of dislocation–void interactions in fcc crystals. *International Journal of Plasticity*, 65:33–42.

[93] Xu, S., Che, R., Xiong, L., Chen, Y., and McDowell, D. L. (2015). A quasistatic implementation of the concurrent atomistic-continuum method for fcc crystals. *International Journal of Plasticity*, 72:91–126.

[94] Xu, S., Xiong, L., Chen, Y., and McDowell, D. L. (2016a). An analysis of key characteristics of the frank-read source process in fcc metals. *Journal of the Mechanics and Physics of Solids*, 96:460–476.

[95] Xu, S., Xiong, L., Chen, Y., and McDowell, D. L. (2016b). Sequential slip transfer of mixed-character dislocations across $\sigma 3$ coherent twin boundary in fcc metals: a concurrent atomistic-continuum study. *npj Computational Materials*, 2:15016.

[96] Yang, S. and Chen, Y. (2015). Concurrent atomistic and continuum simulation of bi-crystal strontium titanate with tilt grain boundary. *Proc. R. Soc. A*, 471(2175):20140758.

[97] Yang, S., Xiong, L., Deng, Q., and Chen, Y. (2013). Concurrent atomistic and continuum simulation of strontium titanate. *Acta Materialia*, 61(1):89–102.

[98] Yim, W. and Paff, R. (1974). Thermal expansion of aln, sapphire, and silicon. *Journal of Applied Physics*, 45(3):1456–1457.

[99] Zarkevich, N. A. and Johnson, D. D. (2015a). Coexistence pressure for a martensitic transformation from theory and experiment: Revisiting the bcc-hcp transition of iron under pressure. *Phys. Rev. B*, 91:174104.

[100] Zarkevich, N. A. and Johnson, D. D. (2015b). Magneto-structural transformations via a solid-state nudged elastic band method: Application to iron under pressure. *J. Chem. Phys.*, 143(6):064707.

[101] Zarkevich, N. A. and Johnson, D. D. (2015c). Nudged-elastic band method with two climbing images: finding transition states in complex energy landscapes. *The Journal of chemical physics*, 142(2):024106.

[102] Zarkevich, N. A., Levitas, V. I., Chen, H., and Johnson, D. D. (2018). *to be published*.

[103] Zhou, M. and McDowell, D. L. (2002). Equivalent continuum for dynamically deforming atomistic particle systems. *Philosophical Magazine A*, 82(13):2547–2574.

CHAPTER 4. TRIAXIAL STRESS INDUCED HOMOGENEOUS HYSTERESIS-FREE FIRST ORDER PHASE TRANSFORMATIONS WITH STABLE MEDIATE PHASES

Reproduced from 'Levitas, Valery I., Hao Chen, and Liming Xiong. Triaxial-stress-induced homogeneous hysteresis-free first-order phase transformations with stable mediate phases. Physical review letters 118, no. 2 (2017): 025701.'

Starting with thermodynamic predictions and following with molecular dynamics (MD) simulations, special triaxial compression-tension states were found for which the stresses for the instability of the crystal lattice of silicon (Si) are the same for direct and reverse phase transformations (PTs) between semiconducting Si I and metallic Si II phases. This leads to unique homogeneous and hysteresis-free first-order PTs, for which each intermediate crystal lattice along the transformation path is in indifferent thermodynamic equilibrium and can be arrested and studied by fixing the strain in one direction. By approaching these stress states, a traditional two-phase system continuously transforms to homogenous intermediate phases. Zero hysteresis and homogeneous transformations are the optimal property for various PT applications, which reduce damage and energy dissipation.

4.1 Introduction

First-order displacive stress-induced PTs under normal and high pressure are of great fundamental and applied interest for the synthesis and application of new phases and materials (2; 3; 4; 5; 1; 6; 7). PTs start when the crystal lattice of a parent phase loses its stability (1; 8). Stresses for direct and reverse PTs are located on different sides of the phase equilibrium stress (see

(8) and Fig. 6.1), and their difference represents stress hysteresis, which can be quite large. Any intermediate homogeneous state of the crystal lattice along the transformation path is unstable under prescribed stresses. If strain is prescribed or fixed during transformation in an attempt to stabilize intermediate state, the material transforms into heterogeneous two-phase system (similar to Fig. 5.2A) with interfaces between the phases (nucleation), and further growth of the product phase occurs via interface motion. In real materials, defects produce stress concentrations and instabilities start locally near defects at smaller deviation from the equilibrium stresses. Due to lattice mismatch, interfaces generate significant elastic stresses, that propagate together with interfaces through the entire sample during cyclic direct-reverse PTs and cause damage while passing through material defects. Stress hysteresis for growth is determined by interfacial friction and energy (9; 2). On the applied side, stress hysteresis and the corresponding energy dissipation, as well as interfacial stresses should be reduced for many PT-related applications, like for shape memory alloys for actuation or medical applications (2; 3; 4) or caloric materials (4; 5).

4.2 Lattice instability of Si I to Si II transformation

On the fundamental side, it is of interest to stabilize intermediate structures along the transformation path and study their properties (10), with the expectation that they may be unique. Also, significant reduction of the PT pressure by applying nonhydrostatic stresses is of basic and applied interests (1; 6; 7), but it is still not connected to lattice instabilities.

Let us consider as an example a cubic crystal lattice under action of three stresses normal to cubic faces, σ_i, and for compactness assume $\sigma_1 = \sigma_2 \neq \sigma_3$. Let lattice instability lines in the plane $\sigma_1 - \sigma_3$ have different slopes for direct and reverse first-order PTs, see the example for Si I$\leftrightarrow$Si II PTs in Fig. 6.1. Instability lines correspond to the disappearance of the respective minimum of the Gibbs energy G (Fig. 6.1), where the order parameter is related to the transformation strain that transforms the crystal lattice of the parent phase to that of the product phase (8; 11). Since instability lines have different slopes, they should have a common point. They cannot intersect, i.e., be continued beyond the common point, because this would mean that the low stress (pres-

sure) phase transforms to the high pressure phase at a stress reduction, which is contradictory. We exclude the cases where the common point represents transition from the first- to second-order PT or critical point, beyond which phases are not distinguishable. Then the lattice instability lines should merge for some range of stresses (Fig. 6.1). The phase equilibrium line (corresponding to the equality of the Gibbs energy of phases (Fig. 6.1)) is between instability lines, and consequently, it should also coincide with the merged lines. Stress hysteresis, which is defined as the difference in values of σ_3 between instability stresses for direct and reverse PTs for the same σ_1, decreases to zero when σ_1 tends toward the merged region. Within the merged region, the energy barrier between phases disappears and Gibbs energy possess a flat portion (Fig. 6.1) with constant energy between strains corresponding to each of the phases. Consequently, each intermediate phase along the transformation path has the same Gibbs energy as both phases and is by definition in a neutral or indifferent (i.e., intermediate between stable and unstable) thermodynamic equilibrium state. This should lead to unique homogeneous and hysteresis-free first-order PTs. Each of the states can be considered as a separate intermediate phase since it has distinct lattice parameters and the transformation between any of these states is accompanied by a change in strain and latent heat. Thus, there is an infinite number (continuum) of intermediate phases with homogeneous (without interfaces) transformations between them. These intermediate homogeneous phases and the entire transformation process can be arrested and studied by fixing strain in one direction; they may possess exceptional properties. When starting with a two-phase structure, stresses change toward the merged region, the energy barrier between phases at equilibrium, $A \to 0$. In continuum Ginzburg-Landau-type theory (8; 11), the interface energy is $\sim \sqrt{A}$, and the width is $\sim 1/\sqrt{A}$. Thus, when approaching the merged region, the interface energy tends to zero but width diverges. This means the two-phase structure should continuously transform to a homogenous intermediate phase. Before reaching homogeneous states, unique heterogeneous intermediate structures with very broad interfaces with controllable width can also be stabilized at a prescribed strain. These structures may possess unexpected properties. Due to homogeneous transformation and lack of interfaces, internal stresses are absent and damage will be minimal as well, despite the possibility

of large transformation strains. Zero hysteresis results in zero energy dissipation. Both these properties are of great fundamental interest and applied importance for various PT-related applications (2; 3; 4; 5). These phenomena should occur for any known or specially designed material for which stresses for the instability of crystal lattice can be made the same for direct and reverse PTs.

4.3 Simulation results

The above hypothetical scenario is purely thermodynamic and is not related to any specific atomic structure. The goal of the current letter is to find a proof of concept for the above described behavior. This can be done using phase field or atomistic simulations. For a small sample consisting of a dozen lattice cells under strain-controlled condition, transformation is always homogeneous even when there is a barrier between phases (12; 13; 14). This is a well-known size effect, which does not allow heterogeneous microstructure in a small sample because of interfacial and elastic energy. Thus, a sample should have large enough size and size-independence of the observed phenomena should be proven. First principle simulations are prohibitively expensive for such simulations, so we chose MD. In principle, any interatomic potential would be sufficient for the proof of concept, even Lennard-Jones. To make it more realistic, we consider here Si I↔Si II PTs using Tersoff potential (see supplementary material).

MD simulations at 1 K were utilized to study PTs Si I↔Si II under various combinations of compressive true (Cauchy) stress (i.e., force per unit deformed area) σ_3 and two normal stresses $\sigma_1 = \sigma_2$, all along cubic axes (Fig. 6.1); positive stresses are tensile. Lattice instability and initiation of PT correspond to stresses at which the initial crystal lattice cannot be stabilized. It is found that in the $\sigma_3 - \sigma_1$ plane initiation of both direct and reverse PTs occurs at straight lines (Fig. 6.1), described by equations $\sigma_3^d = -11.8286 + 0.6240\sigma_1$ and $\sigma_3^r = -9.3888 + 0.3840\sigma_1$. Because instability lines possess different slopes, they should intersect at the point $\sigma_1 = 10.1658$ and $\sigma_3 = -5.4851$. Instead, the instability line for the Si I→Si II PT bends and merges with the line for the Si II→Si II PT within a broad stress range, in agreement with our predictions. When stresses $\sigma_1 = \sigma_2 = 11GPa$ were fixed at a value corresponding to the zero-barrier region, an increase

in compressive Lagrangian strain E_3 (i.e., increase of the displacement at the boundary) leads to the homogeneous transformation process from Si I to Si II, and an intermediate crystal structure can be arrested (see Fig. 5.2 B and videos 1 and 3-5). Away from the merged region, when Si I loses its stability, transformation occurs through nucleation of Si II followed by formation of Si II bands (like in Fig. 5.2A and video 2) and their growth until completing the PT. This happens both under prescribed stresses and prescribed and changing strains, i.e., homogeneous intermediate structures are not observed and cannot be stabilized away from the zero-barrier region.

When we start with a two-phase structure under fixed strain E_3 and increase tensile stresses $\sigma_1 = \sigma_2$ toward the merged region, the two-phase Si I-Si II structure continuously transforms with increasing σ_1 to the intermediate homogenous phase (Fig. 5.2A and movie 3) that is determined by E_3. When starting with a homogeneous intermediate phase and reducing tensile stress $\sigma_1 = \sigma_2$, the same structures are observed at the same stresses (movie 4), i.e., the transformation process is fully reversible without hysteresis. Presence of two-phase structure and continuous transition to and from it from and to homogeneous intermediate structures, the same for sample sizes from 5 to 40 nm, prove that the homogeneous transformation is not caused by small sample size and/or periodic boundary conditions. Thus, all our thermodynamic predictions have been confirmed for Si I↔Si II PTs, which occur at large elastic and transformational strains.

An additional insight can be obtained by analyzing stress-strain curves for Si I↔Si II PTs in Fig. 5.3, which are the same for increasing and decreasing strains E_3. In the stress σ_1 range $10-13GPa$, some small differences between instability stresses for direct and reverse PTs are observed, but they are within $\pm 1\%$, which is below the simulation error. That is why we claim that both instability lines in Fig. 6.1 merge within a finite stress σ_1 range. Strain distribution within the instability region is homogeneous for $\sigma_1 \geq 10GPa$ and for each E_3 describes intermediate homogeneous phase.

With increasing stress σ_1, the difference in strain for initiation of the direct and reverse PTs reduces and reaches zero at $14GPa$, which substitutes the first-order PT with the second order PT (Fig. 5.3 and movie 6). In contrast to known second-order PTs, which are related to the shift of intracell atoms and corresponding change in symmetry and occur at small strains, here there are

no intracell atomic displacements (Fig. 4.4A) and changes in symmetry, and strains are very large. This second-order PT only represents a large jump in elastic modulus. A further increase in σ_1 leads to disordered phase, which will be discussed elsewhere.

The possibility of arresting intermediate homogeneous phases, if confirmed by experiments, opens unprecedented opportunities to study their properties and the entire transformation process. For example, how do semiconducting properties change to metallic ones and at what stage? What are the structures with intermediate semiconducting-metallic states? What are the thermodynamic and mechanical properties of intermediate states that participate in Landau-type theory for stress-induced displacive PTs (8; 11)? There was never a way to determine them directly experimentally. Intermediate homogeneous phases may exhibit some unknown and extraordinary properties, which could find corresponding applications.

Note that homogeneous strain was also observed for $\sigma_1 = 9GPa$ (video 5) and the stress-strain curve shown in Fig. 5.3 is the same for sample sizes from 5 to 40 nm. Since there is a small but finite Gibbs energy barrier between Si I and Si II, these intermediate homogeneous phases are not in indifferent equilibrium. Even better, it shows the possibility to stabilize intermediate locally unstable homogeneous phases, including the phase corresponding to the local energy maximum. The alternative two-phase structure is suppressed due to interfacial energy and energy of internal elastic stresses. At the lower stress $\sigma_1 = 8GPa$ the intermediate heterogeneous nanostructure is stabilized (video 2), in which strain oscillates with the magnitude of 5% without clear phases and interfaces. At $\sigma_1 = 6.9GPa$, intermediate low-strain phase is (almost) homogeneous but the high-strain phase region is much thinner than the interface region and does not possess homogenous-strain portion. Again, our thermodynamic prediction of slightly heterogeneous intermediate structures and structures with broad interfaces is confirmed with MD simulations. Stabilized intermediate heterogeneous states may also possess interesting properties.

Fig. 4.4 presents some properties of intermediate homogeneous phases. Components of the deformation gradients $F_3 = c/c_0$ and $F_1 = a/a_0$, where c and a are the lattice parameters of the deformed tetragonal cell and subscript 0 corresponds to the unstrained initial lattice ($a_0 = c_0$), are

presented in Fig. 4.4A. Interestingly, that linear relationship for F_1 for intermediate phases is just a smooth linear continuation of the curve for Si I, despite the large strains and nonlinear elasticity. When F_1 and F_3 were calculated based on the intracell atoms, results were the same. That means that the Cauchy-Born hypothesis is met, i.e., intracell atoms do not have independent degrees of freedom; consequently, they cannot cause instability for first- and second-order PTs. The potential energy of the system vs. strain E_3 is presented in Fig. 4.4B. While for $\sigma_1 = 0GPa$ this is the energy of the mixture of Si I and Si II, for $\sigma_1 = 9GPa$ this is the energy of the locally unstable intermediate homogeneous phases. Linear energy vs. E_3 corresponds to constant energetic stress.

We also found that if one varies $\sigma_2 \neq \sigma_1$ keeping $\sigma_2 + \sigma_1 = const$, this practically does not affect σ_3^d or σ_3^r. This significantly broadens the stress states for which intermediate homogeneous phases and hysteresis-free PT can occur.

To summarize, we predicted thermodynamically and proved with MD simulations for Si I↔Si II PTs new phenomenon of homogeneous and hysteresis-free first-order PT. A broad range of special triaxial compression-tension states were found for which the stresses for the lattice instability for direct and reverse PTs were the same. Since the energy barrier between two phases disappears, and the Gibbs energy landscape has a constant flat region, each intermediate state along the transformation path is in a neutral thermodynamic equilibrium and can be considered as a separate intermediate phase. Thus, there is a continuum of the intermediate phases with homogeneous and hysteresis-free transformations between them. Each intermediate phase can be arrested and studied by fixing the strain in one direction. By approaching these stress states, the interface width in a traditional two-phase system increases and diverges, interface energy tends to zero, and a two-phase structure continuously transforms to homogenous intermediate phases. This also allows for the stabilization of unique slightly heterogeneous intermediate structures with broad and controlled interface widths, which may possess unexpected properties. Zero hysteresis and homogeneous transformations are the optimal property for various PT-related applications (2; 3; 4; 4; 5), which reduce damage and energy dissipation. Further increases in stresses substitute the first-order PT

with the unusual second-order PT, without intracell atomic displacements and change in symmetry, and at large strains.

While it is well-known that utilization of first principle simulations instead of MD would deliver more reliable results for Si and other materials, our results are sufficient for conceptual proof. Similar phenomena and phases may be found in many other materials. Since there is no fundamental reason for collinearity of the instability lines, they should intersect for many material systems. The practical problem is whether this region is achievable before fracture or plastic flow occurs. Materials in which homogenous PTs may occur could be designed by proper multicomponent alloying, as was done for shape memory alloys (2; 3; 4) or caloric materials (4; 5). Multiaxial loading can be combined with other stimuli, like temperature and magnetic field, which will increase the chances to find zero-hysteresis transformations and intermediate homogeneous phases for economically realistic external stimuli. If confirmed by experiments, these results will allow one to control/reduce the stress hysteresis, interface energy and dissipation and reduce damage by controlling multiaxial stress state and other fields, which may revolutionize field of transforming materials, in particular, for elastocaloric and smart material applications.

Simulation Method. In this work, classical molecular dynamics simulations were performed using the LAMMPS package(15). Initially, the five most popular potentials for silicon (REAXFF(16; 17; 18; 19), MEAM(20), Stillinger-Weber(SW)(21), modified Tersoff(22) and Tersoff(23)) are compared for their capability to describe phase transformation from Si I to Si II in silicon. Comparison was performed for uniaxial loading, i.e., compressive Cauchy stress σ_3 was applied at $\sigma_1 = \sigma_2 = 0$. The stress-strain curves for all potentials are shown in Figure S1.

For MEAM and REAXFF potentials, no phase transformations were detected up to 16 and 20 GPa, respectively. Thus, simulations were stopped for these cases at the respective stresses. For the Stillinger-Weber potential, phase transformation starts at the maximum stress of 15 GPa; however, resultant phases are mixtures of amorphous silicon(24) and silicon II. Occurrence of two phase transformations simultaneously does not correspond to the goal of the current study. For the modified Tersoff potential, transformation starts at the maximum stress of 15GPa, but Si I

transforms to the Imma phase, which is consistent with results in (25). However, in experiments under indentation or uniaxial loading(26), Si I first transforms to Si II and then to Imma phase. For the Tersoff potential(23), phase transformation starts at the peak stress of 12GPa, which is close to both the experimental values in (26) and the first principle calculation result in (27). Based on this study, the Tersoff potential(23) is the best option from the point of view of accuracy and correspondence to our goal. It is used in the present study. The majority of simulations have been performed for a Si sample containing 64,000 atoms. To prove a size-independence of the results, simulations under uniaxial loading were performed for varying sample sizes of 5nm to 40nm, which contained 8,000 to 4,096,000 atoms. A time step of 1 fs was used in all simulations. The system temperature is set as $T = 1K$ to eliminate the possibility of the occurrence of thermally activated PTs. Effects of the free surfaces on the PTs were excluded by employing periodic boundary conditions along all three cubic directions. Simulations were conducted under (a) a specified Cauchy stress and (b) mixed loading, which is a strain-controlled along axis 3 and Cauchy-stress-controlled along two other directions with $\sigma_1 = \sigma_2$. The Cauchy stress was applied to the system using the Berendsen algorithm (28), in which the instantaneous stress of the system was calculated using the virial formula and controlled in two steps. First, a Cauchy stress increment of 0.01 GPa was applied to the simulation cell; this was then followed by an equilibration of the entire specimen for 10 ps. In order to ensure that a desired Cauchy stress has been achieved, the system virial stress at the end of each loading increment was calculated and was checked against the prescribed stress, assuming that the averaged Cauchy stress coincides with the virial stress (29). For the strain-controlled loading, the fix deform method in LAMMPS was employed. That is, each time after the simulation box size along the main loading direction was changed at a value of 0.2 angstrom, the system was equilibrated for 100 ps. This equilibration process occurred with a fixed box size along the loading direction and prescribed stresses $\sigma_1 = \sigma_2$ along the other directions.

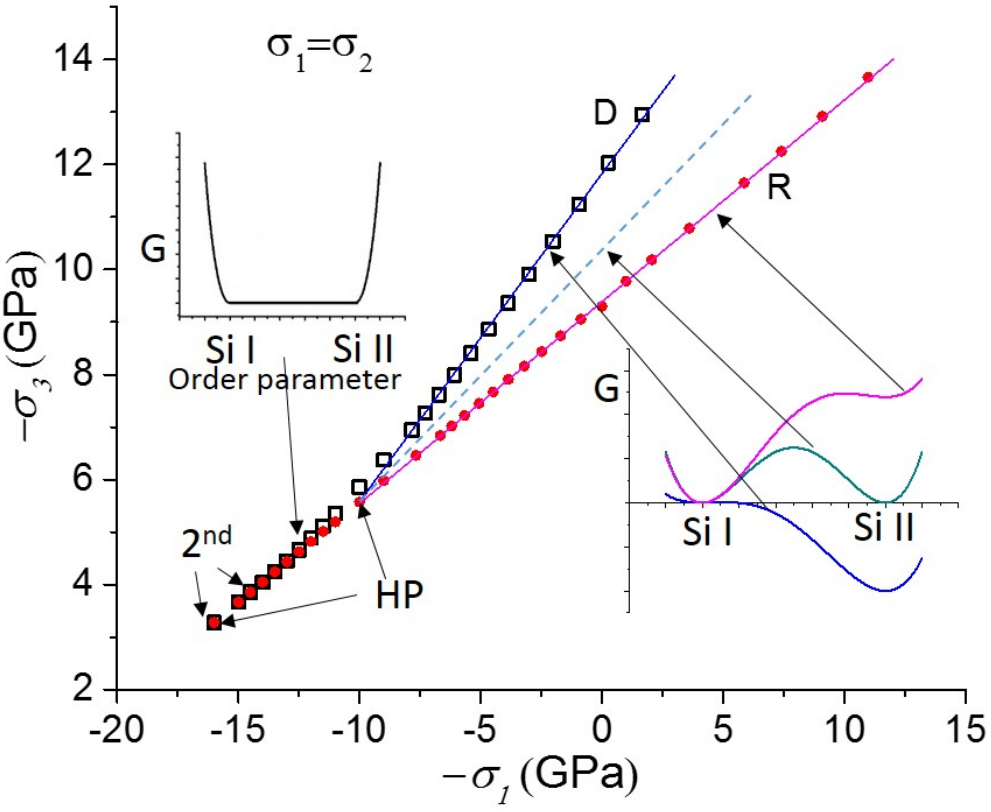

Figure 4.1 Relationships between stresses σ_3 and $\sigma_1 = \sigma_2$ for crystal lattice instability for direct and reverse Si I↔Si II PTs and the existence of the continuum of homogenous intermediate phases. Each instability line is related to the disappearance of the minimum in the Gibbs energy G plot for the corresponding phase. The dashed line is the tentative phase equilibrium line corresponding to equality of the Gibbs energy G of phases. For stress states at the merge of two instability lines, Gibbs energy has a plateau with constant value leading to an unique homogeneous and hysteresis-free first-order Si I↔Si II PT, with a continuum of intermediate homogeneous phases (HP), which are in indifferent thermodynamic equilibrium. With a further increase in σ_1, the first-order transformation changes to the second-order transition (designated as 2^{nd}) and then (not shown) to a disordered phase.

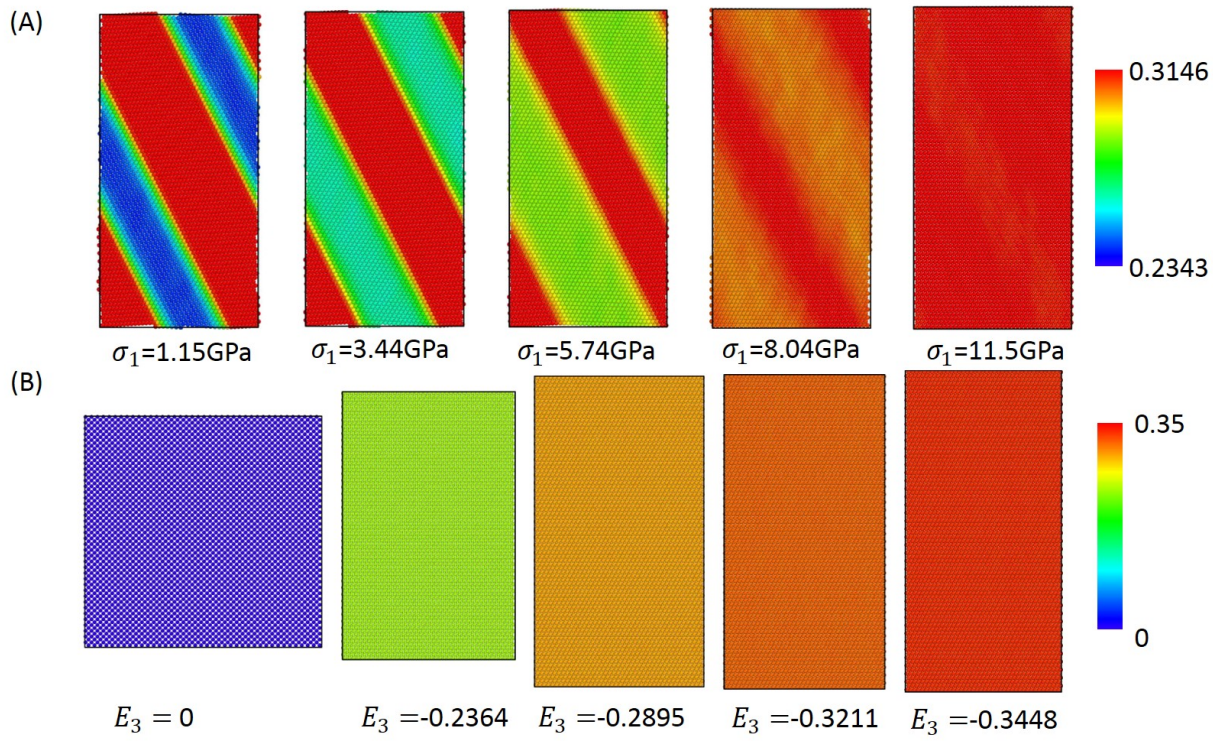

Figure 4.2 Nanostructure evolution in silicon during phase transformation. (A) Transformation of two-phase Si I-Si II mixture into intermediate homogeneous phases at prescribed compressive Lagrangian strain $E_3 = -0.31$ and increasing tensile stresses $\sigma_1 = \sigma_2$. (B) Homogeneous transformation process from Si I to Si II through continuum of homogeneous phases with increasing strain E_3 at fixed stresses $\sigma_1 = \sigma_2 = 11GPa$. Colors characterize the local von-Mises shear strain.

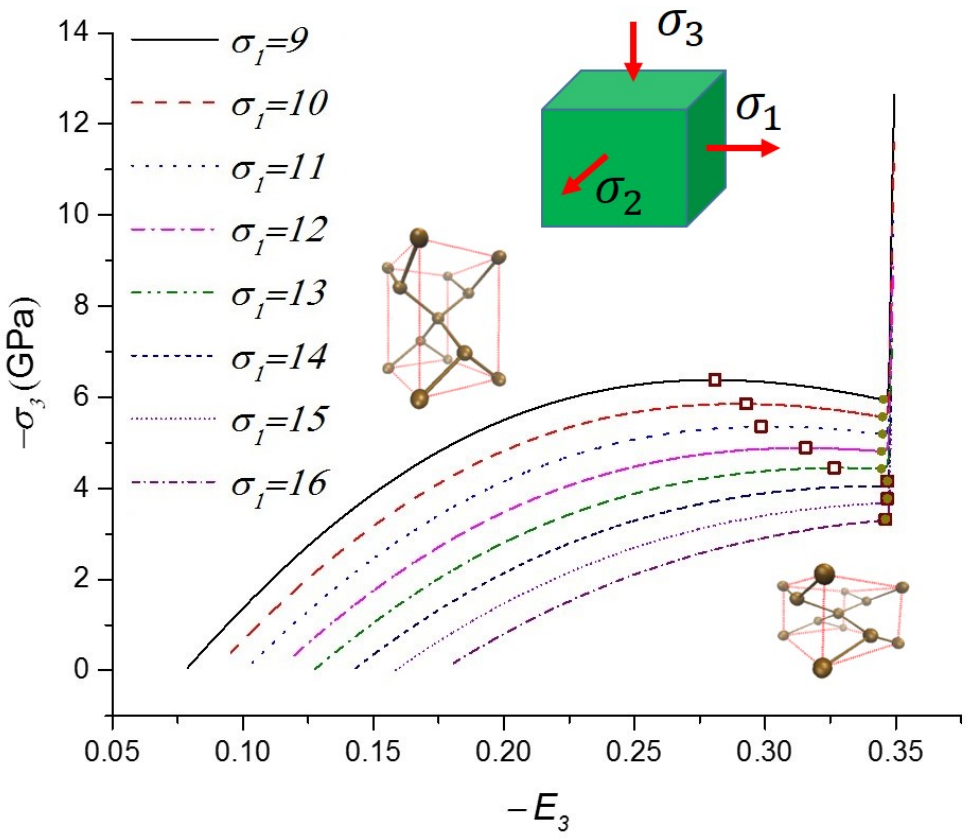

Figure 4.3 True stress σ_3 versus Lagrangian strain E_3 for various fixed stresses $\sigma_1 = \sigma_2$ and increasing/decreasing E_3 during Si I↔Si II PT. Lattice instability points for Si I→Si II PT correspond to the local maxima of stresses while for Si II→Si I PT they correspond to the local minima. Between them, transformation path passes through continuum of intermediate homogeneous phases.

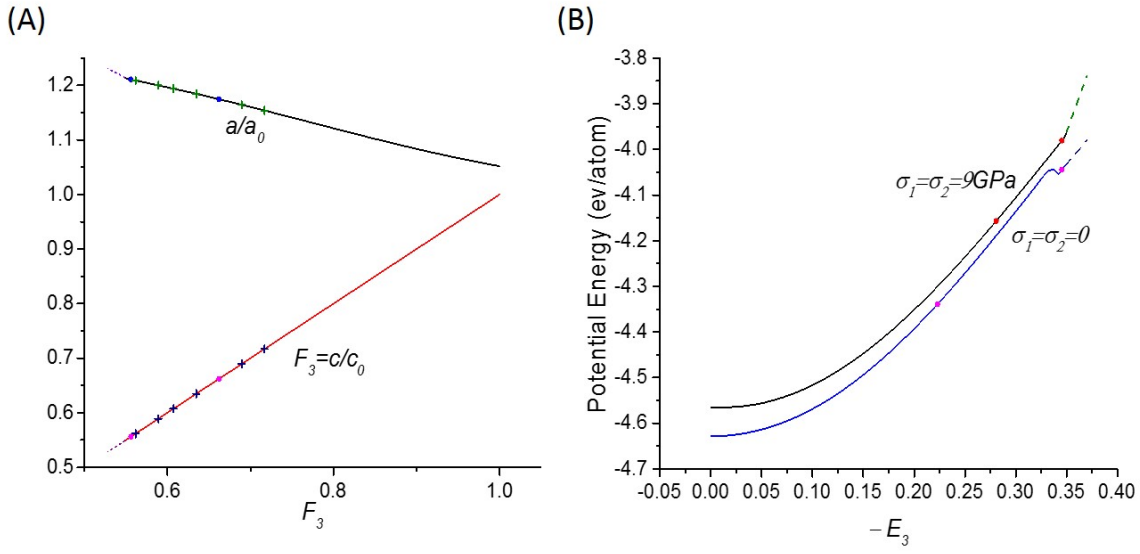

Figure 4.4 Properties of locally unstable intermediate homogeneous phases. Bold dots designate instability points. (A) Components of deformation gradient $F_3 = c/c_0$ and $F_1 = a/a_0$ for $\sigma = 9GPa$ vs. F_3. Lines are based on crystal cell parameters and symbols are calculated based on the intracell atoms. (B) Potential energy versus F_3 for two different stresses σ_1.

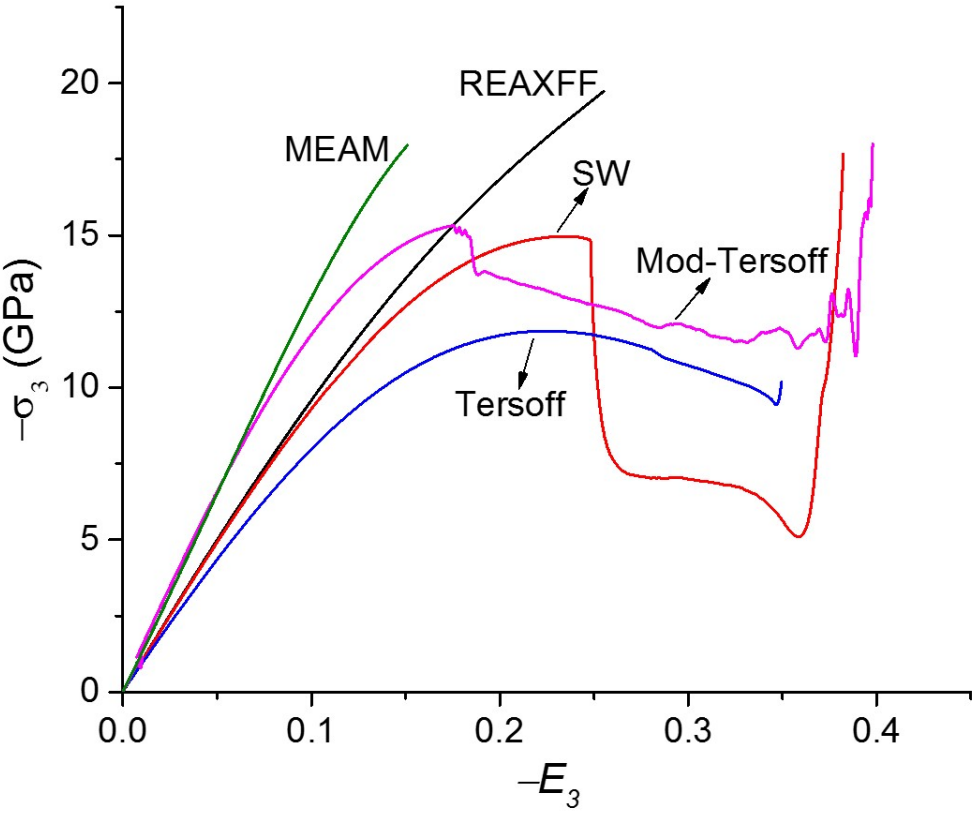

Figure 4.5 True stress σ_3 versus Lagrangian strain E_3 for $\sigma_1 = \sigma_2 = 0$ for various interatomic potentials.

Bibliography

[1] V.D. Blank and E.I. Estrin, (CRC Press, Boca Raton, 2014), pp. 382-423.

[2] J. Cui *et al., Nat. Mater.* **5**, 286-290 (2006).

[3] C. Chluba *et al., Science* **348**, 1004-1007 (2015).

[4] S. Yintao, C. Xian, V. Dabade, T.W. Shield, R.D. James, *Nature* **502**,85-88 (2013).

[5] I. Takeuchi, K. Sandeman, *Physics Today* **68**, 48-54 (2015).

[6] V.I. Levitas, L.K. Shvedov, *Phys. Rev. B* **65**, 104109 (2002).

[7] C. Ji, V.I. Levitas, H. Zhu, J. Chaudhuri, A. Marathe, Y. Ma, *P. Natl. Acad. Sci. USA* **109**, 19108-19112 (2012).

[8] V. I. Levitas, D.L. Preston, *Phys. Rev. B* **74**, 134207 (2002).

[9] G. Ghosh, G.B. Olson, *Acta Metall. Mater.* **42**, 3361-3370 (1994).

[10] A. van de Walle, Q. Hong, S. Kadkhodaei, R. Sun, *Nat. Com.* **6**, 7559 (2015).

[11] V.I. Levitas, *J. Mech. Phys. Solids* **70**, 154-189 (2014).

[12] S. Sorella, M. Casula, L. Spanu and A. Dal Corso, *Phys. Rev. B* **83**, 075119 (2011).

[13] R. Maezono, ND. Drummond, A. Ma, R.J. Needs, *Phys. Rev. B* **82**, 184108 (2010).

[14] S.L. Qiu, P.M. Markus, *J. Phys. Condens. Matter* **24**, 225501 (2012).

[15] P. Steve, *J. Comput. Phys.* **117**, 1-19 (1995).

[16] M.J. Buehler, A. C. van Duin and W.A. Goddard III, *Phys. Rev. Lett.* **96**, 095505 (2006).

[17] M.J. Buehler, H. Tang, A.C. van Duin, and W.A. Goddard III, *Phys. Rev. Lett.* **99**, 165502 (2007).

[18] U. Khalilov, E.C. Neyts, G. Pourtois and A.C. van Duin, *J. Phys. Chem. C* **115**, 24839-48 (2011).

[19] S., Dumpala, S.R. Broderick, U. Khalilov, E.C. Neyts, A.C. van Duin, J. Provine, R.T. Howe, and K. Rajan, *Appl. Phys. Lett.* **106**, 011602 (2015).

[20] M.I. Baskes, *Phys. Rev. B* **46**, 2727 (1992).

[21] F. H. Stillinger and T.A. Weber, *Phys. Rev. B* **31**, 5262 (1985).

[22] P. Erhart and K. Albe, *Phys. Rev. B* **71**, 035211 (2005).

[23] H. Balamane, *Phys. Rev. B* **46**, 2250 (1992).

[24] M.D. Kluge, J.R. Ray and A. Rahman, *Phys. Rev. B* **36**, 4234 (1987).

[25] G. Mogni, A. Higginbotham, K. Gal-Nagy, N. Park and J.S. Wark, *Phys. Rev. B* **89**, 064104 (2014).

[26] V. Domnich, D. Ge, and Yu. Gogotsi. Indentation-Induced Phase Transformations in Semiconductors, In: High Pressure Surface Science and Engineering; Section 5.1, eds. Y. Gogotsi and V. Domnich, (Institute of Physics, Bristol, 2004), 381-442.

[27] M. Durandurdu, *J. Phys. Condese. Matter* **20**, 325232 (2008).

[28] H.J. Berendsen, J. V. Pstma, van Gunsteren, W. F. DiNola, and J. R. Haak, *J. Chem. Phys.* **81**, 3684(1984).

[29] A. K. Suhramaniyan, *Int. J. Solids Struct.* **45**, 4040-6(2008).

[30] A. Stukowski, *Model. Simul. Mater. Sc.* **18**, 015012 (2010).

CHAPTER 5. SLIP OF SHUFFLE SCREW DISLOCATIONS THROUGH TILT GRAIN BOUNDARIES IN SILICON

Reproduced from 'Chen, H., Levitas, V. and Xiong, L., 2019. Slip of shuffle screw dislocations through tilt grain boundaries in silicon. Computational Materials Science, 157, pp.132-135.'

5.1 Abstract

In this paper, molecular dynamics (MD) simulations of the interaction between tilt grain boundaries (GBs) and a shuffle screw dislocation in silicon are performed. Results show that dislocations transmit into the neighboring grain for all GBs in silicon. For $\Sigma 3$, $\Sigma 9$ and $\Sigma 19$ GBs, when a dislocation interacts with a heptagon site, it transmits the GB directly. In contrast, when interacting with a pentagon site, it first cross slips to a plane on the heptagon site and then transmits the GB. The energy barrier is also quantified using the climbing image nudged elastic band (CINEB) method. Results show that $\Sigma 3$ GB provides a barrier for dislocation at the same level of the Peierls barrier. For both $\Sigma 9$ and $\Sigma 19$ GBs, the barrier from the heptagon sites is much larger than the pentagon sites. Since the energy barrier for crossing all the GBs at the heptagon sites is only slightly larger than the Peierls barrier, perfect screw dislocations cannot pile up against these GBs. Furthermore, the critical shear stress averaged over the whole sample for the transmission through the $\Sigma 9$ and $\Sigma 19$ GBs is almost twice on heptagon site for initially equilibrium dislocation comparing with dislocations moving at a constant velocity.

5.2 Introduction

Along with other applications, polycrystalline silicon has been widely used for photovoltaic solar cells. Tremendous efforts have been made to reduce the cost and improve the energy efficiency of polycrystalline Si photovoltaic cells (1; 2) due to the vast demand for renewable solar power. The

strength and ductility of polycrystalline silicon depend not only on the interaction and multiplication of dislocations, but also are determined by the interaction between dislocations and grain boundaries (GBs). However, many details of the dislocation-GB interactions in silicon are not fully understood. Experiments have shown that dislocations in silicon can either pile-up or transmit the GBs (3). Atwater and Brown found that amorphous silicon nucleates heterogeneously at the GBs during the irradiation of polycrystalline Si thin films (4). Using the in-situ high-voltage electron microscopy, Ballin et al.observed that dislocation with a common Burgers vector 1/2[011] transmitted from one grain to the neighboring grain (5). Chen et al. has investigated the interaction between shuffle dislocation loops with $\Sigma 3$, $\Sigma 9$ and $\Sigma 19$ GBs (6). They found that $\Sigma 3$ GB exhibits significantly higher resistance to dislocation transmission than $\Sigma 9$ and $\Sigma 19$ GBs. However unlike the atomistic simulations for metals(7; 8), non-periodic boundary condition along the dislocation line have been applied, which exhibits the free surface effect(6). In order to isolate the free surface effect and the interactions between dislocations and GBs, periodic boundary condition is applied in this paper.

Also, the dislocation pile up against grain boundary was considered as a key contributors for the drastic reduction of the phase transformation pressure in materials under a large plastic shear (9; 10). It is important to find out whether screw dislocations can pileup against GBs in Si.

This paper aims to provide a fundamental understanding on the interaction between shuffle screw dislocation and ($\Sigma 3$, $\Sigma 9$ and $\Sigma 19$) GBs. Our next paper would present results on interaction between 60^o shuffle dislocations with GBs(11).

5.3 The computational set-up

Figure 6.1 shows the computer models of bi-crystalline silicon, with $\Sigma 3$, $\Sigma 9$ and $\Sigma 19$ GBs in (a), (b) and (c), respectively. These are three most stable GBs among all $< 110 >$ tilt GBs and make up more than 70% of all possible GBs (6; 12; 13). As shown in Figs. 6.1(a-c), grain-I in all the three models have the same crystallographic orientation with xy plane on the (111) glide plane. Periodic boundary conditions were applied in x direction with a periodicity length, $L_x \approx 4nm$.

Lengths of L_x has been varied from $4nm$ to $30nm$ and results are independent of this length due to periodic boundary conditions. Along the other two directions, $L_y \approx 60nm$ and $L_z \approx 40nm$. Several layers of atoms at the two surfaces perpendicular to the y-direction are fixed. The model consists of $\sim 400,000$ atoms. Additional computer models for large samples were also constructed and it was shown that the results observed in this paper did not change with the size. To create perfect screw dislocations, e.g., with the Burgers vector $b = 1/2[1\bar{1}0]$ (14), a constant ramped velocity v along x direction is applied on the several layers of atoms at the left boundary above and below the central glide plane and in opposite directions, as shown in Fig. 6.1 (a) (7; 8; 15). In all simulations, $v = 0.001nm/ps$ and the central glide plane is put between the shuffle set to generate a perfect screw dislocation. To study the effect of dislocation velocity of the GB resistance, shear stress was applied immediately after dislocation generation near the right side of the sample. Under prescribed shear stress, dislocation in silicon reaches a stationary velocity(16) before it reaches GB. This procedure was repeated with increasing shear strain until dislocation passes through GB. Alternatively, the static screw dislocation is inserted by applying the displacement field of a screw dislocation(15) near the GB, for example, near the heptagon defects in the first grain. The system is relaxed for $100ps$ to get the stable dislocation structure. Then shear stress is gradually increased until the dislocation transmits into the neighboring grain.

Simulations were performed at a constant temperature of $300K$ using Nosé-Hoover thermostat. Displacement corresponding to a constant shear strain (ϵ_{appl}) is applied homogeneously to the external surface of the MD cell in the $x - z$ shear plane. The atomic interactions are described by the Stillinger-Weber (SW) potential (17), which is capable to capture undissociated shuffle dislocations in silicon. The time step for all simulations is 1fs. All simulations were conducted using the Large-scale Atomic/Molecular Massively Parallel Simulator (LAMMPS) (18).

5.4 The Interaction between Shuffle Screw Dislocations and Grain Boundaries in Silicon

In this section, we present how perfect screw shuffle dislocations interact with different GBs. The trajectories of dislocations are tracked using the von-Mises shear strain in OVITO(19; 20; 21).

Fig. 5.2a shows how a shuffle screw dislocation transmits the Σ3 GB directly. In our simulations, as long as the screw dislocation migrates in grain I, it can transmit the GB into grain II, which indicates that the Σ3 GB also imposes no barrier for a screw dislocation motion. This is consistent with the screw dislocation behavior in bi-crystalline F.C.C. metallic materials (7). In F.C.C. metals, the full screw dislocation dissociates into two partial dislocations. When the screw dislocations interact with twin boundaries in metal, the dissociated screw dislocations first constrict into a full screw dislocation and then transmit the GB. During the transmission procedure, the constricting process imposes the main energy barrier (7). However, in silicon, since the screw dislocation on the shuffle set is already a full dislocation, the constricting process is not needed, consequently, Σ3 GB acts as a low energy barrier to shuffle dislocations in silicon.

Fig. 5.2b presents the process of the interaction between a perfect screw dislocation with Σ19 GB, which is composed of continuous pentagon-heptagon defects as shown in Fig. 6.1 (12; 6). The perfect screw dislocation can have two different interaction sites with Σ19 GB, i.e., the pentagon site (designated p_5 site below) and the heptagon site (designated p_7). When a dislocation interact with Σ19 GB at p_7 site as shown on the left side of Fig. 5.2b, the dislocation switches the glide plane to the (111) plane in the neighboring grain directly, which is similar to a cross-slip behavior. However, when the dislocation interacts with the p_5 site, as shown in the right side of Fig. 5.2b, the dislocation first cross slips into the neighboring plane on the p_7 site in grain I and then transmits the GB. This results show that the heptagon sites act as higher energy barrier for dislocation motion than the pentagon site does. This can also be seen in the process of an interaction process between perfect screw dislocations and Σ9 GB shown in Fig. 5.2c since Σ9 is also composed of continuous pentagon-heptagons (Fig. 6.1). For the heptagon sites, the dislocation transmits the GB directly through a similar cross-slip behavior which is similar to that in Σ19 GB. However,

for a pentagon site, the dislocation first cross slips to the plane on the heptagon site. Then the dislocation transmits the GB to the neighboring grain to a plane with 71.3^0 inclination angle as shown on the right 5.2c. Thereafter, due to the large critical shear stress, it has another cross-slip in grain II to a plane with the lower critical shear stress and inclination angle (15). This again demonstrates that the pentagon site imposes a higher energy barrier for the dislocation migration than the heptagon site does.

The climbing image nudged elastic band (CINEB) method was used to determine the energy barrier of the dislocation motion across a stress-free GB (22; 23). In the CINEB calculations, the dislocation was created by adding the screw dislocation displacement into the sample. It can be seen that the energy barrier imposed by $\Sigma 3$ is almost the same as the Peierls barrier for dislocation motion (Fig. 5.3). For both $\Sigma 9$ and $\Sigma 19$ GBs, the pentagon sites generate an energy barrier of $1.9ev/nm$ while the heptagon sites produce an energy barrier around $0.6ev/nm$. This explains why the screw dislocation always transmit the GB at the heptagon sites rather than the pentagon sites. Since the energy barrier for crossing all the GBs at the heptagon sites is only slightly larger than the Peierls barrier for the dislocation motion in bulk, perfect screw dislocations cannot pile up against these GBs and cannot reduce phase transformation pressure during plastic deformations (9; 10). At the same time, all GBs produces 60^o dislocation pile-up, which essentially reduces the transformation pressure from Si I to Si II under shear (24; 25).

In addition, the velocity of a dislocation is also found to play an important role in the process of a dislocation-GB interaction. Here we found that the critical shear stress needed for dislocation transmission through the GB is different for moving and static dislocation. For static dislocation the critical shear stress averaged over sample is $\tau_s = 5.3$ GPa and for moving dislocation it is $\tau_d = 2.9$ GPa for $\Sigma 19$ GB and $\tau_s = 5.4$ GPa and τ_d=2.9 GPa for $\Sigma 9$ GB on heptagon defects. Here, the dislocation reaches a stationary speed $v = 3065m/s$ when it meets the GB under shear stress $2.9GPa$, which is far below the elastic wave speed in silicon(26). Interestingly, τ_d and τ_s are almost the same for $\Sigma 19$ and $\Sigma 9$ GBs, which demonstrates that the energy barrier is determined by the local structure of the GB. Thus, the energy barrier is the same for heptagon sites in $\Sigma 19$ and $\Sigma 9$

GBs and it is independent of the misorientation angle of the GBs under stress-free state (15; 7), which is similar to the screw dislocation behavior in F.C.C. metals.

5.5 Conclusions

In the paper, the interactions between tilt GBs and a shuffle screw dislocation in silicon are investigated using molecular dynamics. Results show that the dislocation transmits into the neighboring grain for all GBs. For $\Sigma 3$ GB, the dislocation goes through the GB directly. For $\Sigma 9$ and $\Sigma 19$ GBs, when the dislocation is on heptagon site, the dislocation transmits the GB directly as well. However, when the dislocation is on the pentagon site, it first cross slips to a plane on the heptagon site and then transmits the GB. The energy barrier was calculated using the climbing image nudged elastic band method. Results show that $\Sigma 3$ GB generates the barrier at the level of the Peierls barrier. For both $\Sigma 9$ and $\Sigma 19$ GBs, the barrier for dislocation transmission of heptagon sites is $0.6 ev/nm$, while it is $1.9 ev/nm$ for pentagon defects. Furthermore, we found that the critical shear stress for the transmission is lowered from $5.3 GPa$ to $2.9 GPa$ for moving dislocation versus the static dislocation. Since energy barrier for crossing the $\Sigma 3$ is equal to the Peierls barrier for dislocation motion in bulk, and for $\Sigma 9$ and $\Sigma 19$ GBs at the heptagon defects it is only slightly larger than the Peierls barrier, perfect screw dislocations cannot pile up against these GBs and cannot reduce phase transformation pressure during plastic deformations (9; 10).

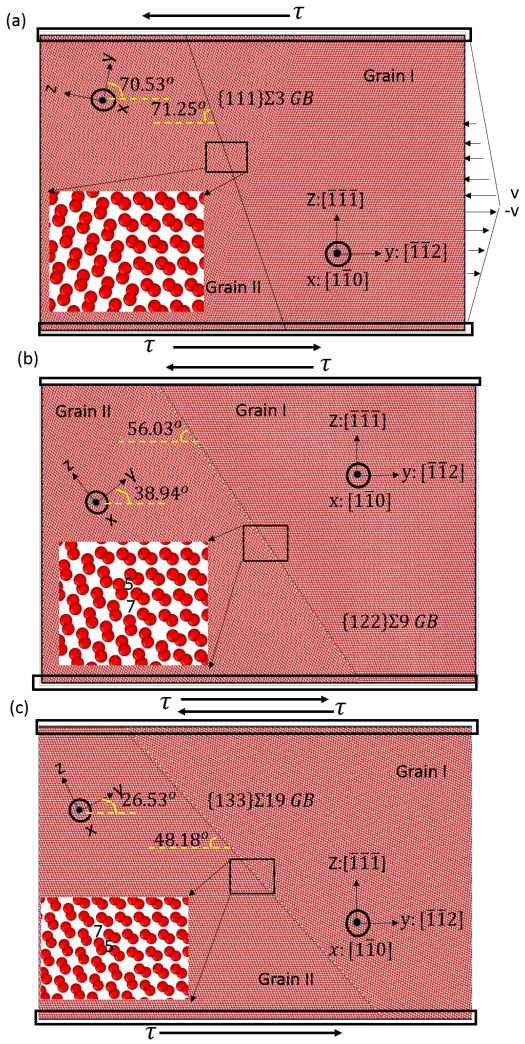

Figure 5.1 Computational models of bicrystalline silicon with (a) Σ3, (b) Σ9, and (c) Σ19 grain boundaries.

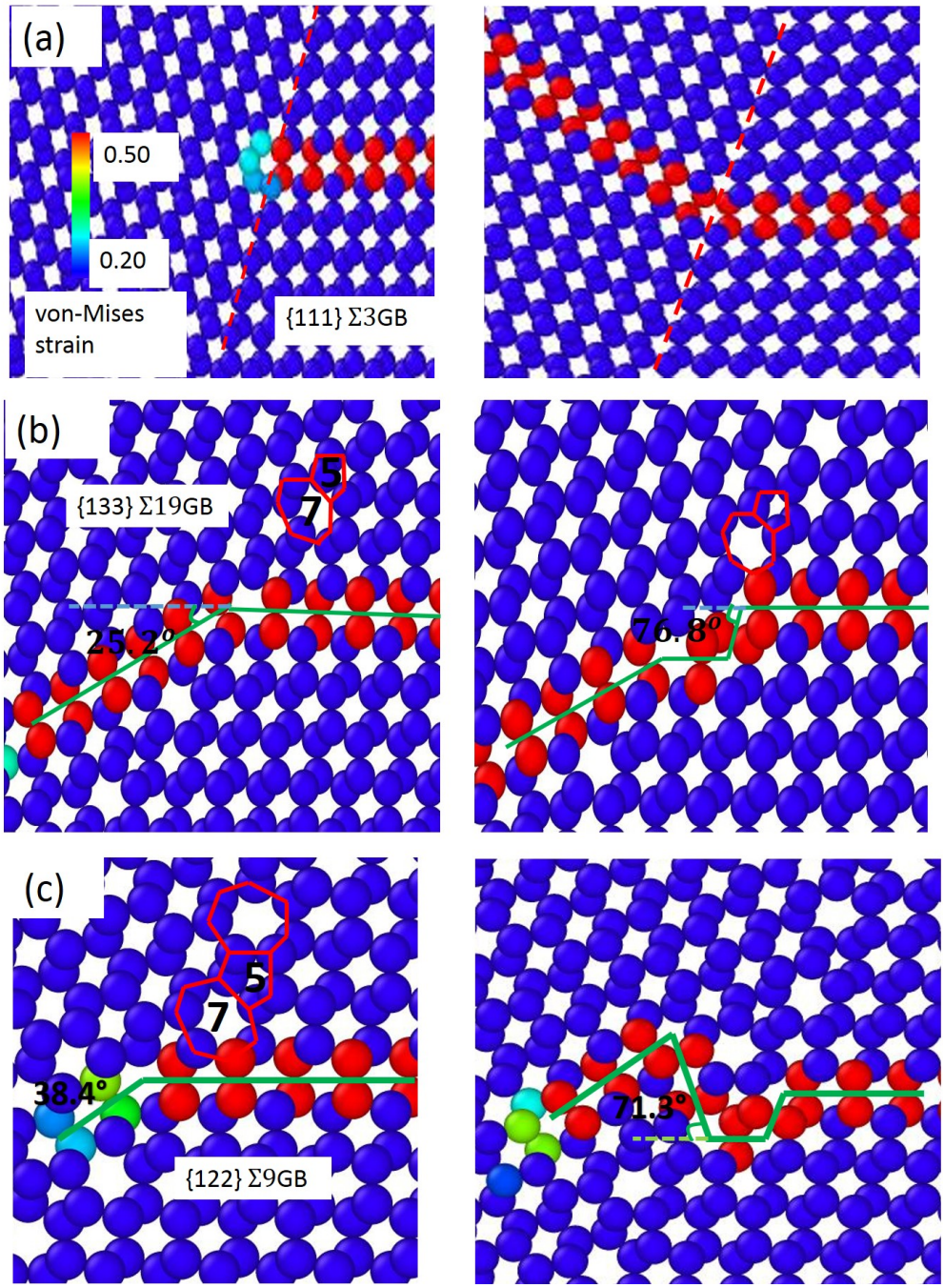

Figure 5.2 The atomistic process for the interactions between perfect screw dislocations and Σ3, Σ9, and Σ19 GBs. (a) The direct transmission process of a shuffle screw dislocation through the Σ3GB. (b) The transmission of a shuffle screw dislocation through the Σ19 GB. The dislocations interact with the heptogon site on the right side and the pentagon site on the left side. (c) The transmission of a shuffle screw dislocation through the Σ9 GB. The dislocation interact with the heptogon site (right) and the pentagon site (left), respectively.

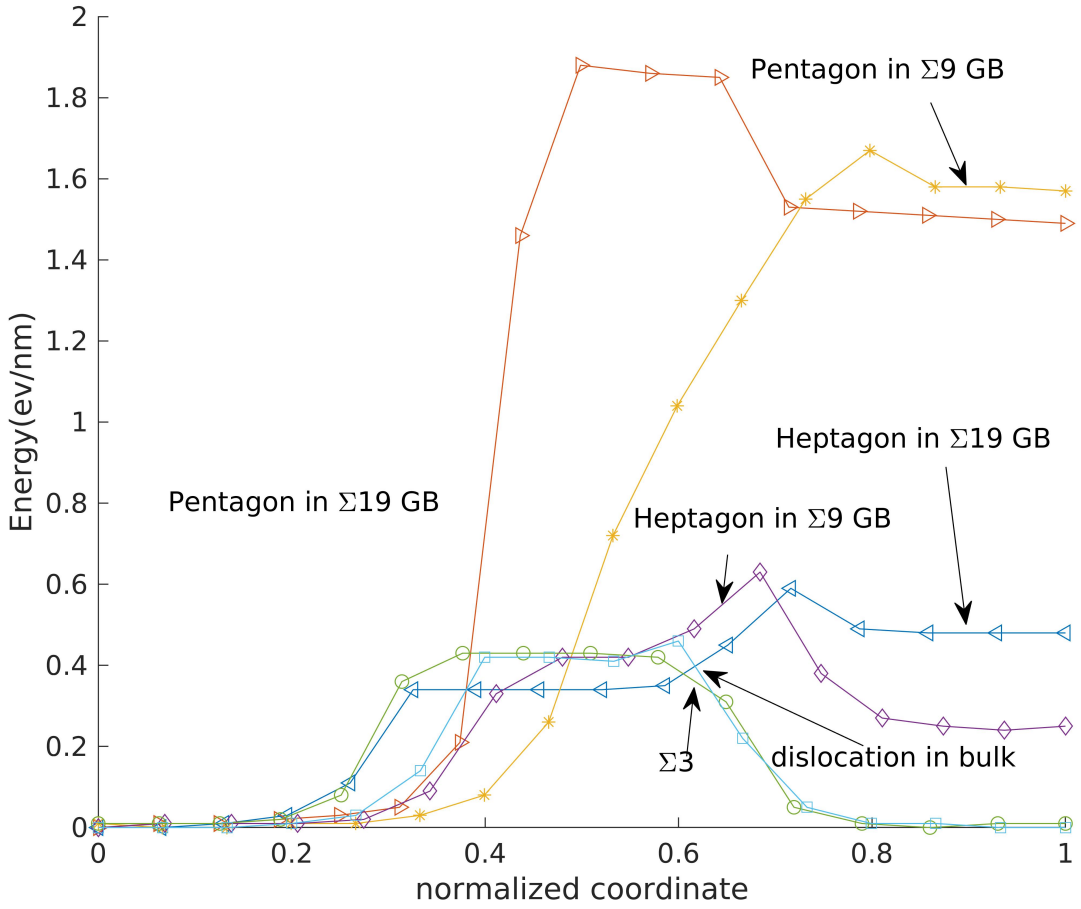

Figure 5.3 The energy barrier calculated by the CINEB method for Σ3, Σ9, and Σ19 GBs in silicon under stress-free state. For comparison, energy barrier for dislocation motion in bulk (without GB) is shown.

Bibliography

[1] Shah, A., Torres, P., Tscharner, R., Wyrsch, N. and Keppner, H., 1999. Photovoltaic technology: the case for thin-film solar cells. science, 285(5428), pp.692-698.

[2] Tanaka, M., 2013. Recent progress in crystalline silicon solar cells. IEICE Electronics Express, 10(16), pp.20132006-20132006.

[3] Martinez-Hernandez, M., Kirchner, H.O.K., Korner, A., George, A. and Michel, J.P., 1987. Dislocations at grain boundaries in deformed silicon. Philosophical Magazine A, 56(5), pp.641-658.

[4] Atwater, H.A. and Brown, W.L., 1990. Grain boundary mediated amorphization in silicon during ion irradiation. Applied Physics Letters, 56(1), pp.30-32.

[5] Baillin, X., Pelissier, J., Bacmann, J.J., Jacques, A. and George, A., 1987. Dislocation transmission through $\Sigma = 9$ symmetrical tilt boundaries in silicon and germanium: I. In situ observations by synchrotron X-ray topography and high-voltage electron microscopy. Philosophical Magazine A, 55(2), pp.143-164.

[6] Chen, X., Xiong, L., Chernatynskiy, A. and Chen, Y., 2014. A molecular dynamics study of tilt grain boundary resistance to slip and heat transfer in nanocrystalline silicon. Journal of Applied Physics, 116(24), p.244309.

[7] Jin, Z.H., Gumbsch, P., Ma, E., Albe, K., Lu, K., Hahn, H. and Gleiter, H., 2006. The interaction mechanism of screw dislocations with coherent twin boundaries in different face-centred cubic metals. Scripta Materialia, 54(6), pp.1163-1168.

[8] Jin, Z.H., Gumbsch, P., Albe, K., Ma, E., Lu, K., Gleiter, H. and Hahn, H., 2008. Interactions between non-screw lattice dislocations and coherent twin boundaries in face-centered cubic metals. Acta Materialia, 56(5), pp.1126-1135.

[9] Levitas, V.I. and Javanbakht, M., 2014. Phase transformations in nanograin materials under high pressure and plastic shear: nanoscale mechanisms. Nanoscale, 6(1), pp.162-166.

[10] Javanbakht, M. and Levitas, V.I., 2016. Phase field simulations of plastic strain-induced phase transformations under high pressure and large shear. Physical Review B, 94(21), p.214104.

[11] Chen, H., Levitas, V.I. and Xiong, L., Amorphous Phase in Silicon Induced by 60^o Dislocations Pile-up against Different Grain Boundaries. to be published

[12] Kohyama, M., Yamamoto, R. and Doyama, M., 1986. Structures and energies of symmetrical¡ 011¿ tilt grain boundaries in silicon. physica status solidi (b), 137(1), pp.11-20.

[13] Ratanaphan, S., Yoon, Y. and Rohrer, G.S., 2014. The five parameter grain boundary character distribution of polycrystalline silicon. Journal of materials science, 49(14), pp.4938-4945.

[14] Cai, W., Bulatov, V.V., Chang, J., Li, J. and Yip, S., 2004. Dislocation core effects on mobility. Dislocations in solids, 12, pp.1-80.

[15] Hull, D. and Bacon, D.J., 2001. Introduction to dislocations. Butterworth-Heinemann.

[16] Li, C.X., Meng, Q.Y., Li, G. and Yang, L.J., 2006. Atomistic simulation of the 60 dislocation mobility in silicon crystal. Superlattices and Microstructures, 40(2), pp.113-118.

[17] Pizzagalli, L., Godet, J., Gunol, J., Brochard, S., Holmstrom, E., Nordlund, K. and Albaret, T., 2013. A new parametrization of the StillingerWeber potential for an improved description of defects and plasticity of silicon. Journal of Physics: Condensed Matter, 25(5), p.055801.

[18] Plimpton, S., 1995. Fast parallel algorithms for short-range molecular dynamics. Journal of computational physics, 117(1), pp.1-19.

[19] Stukowski, A., 2009. Visualization and analysis of atomistic simulation data with OVITOthe Open Visualization Tool. Modelling and Simulation in Materials Science and Engineering, 18(1), p.015012.

[20] Falk, M.L. and Langer, J.S., 1998. Dynamics of viscoplastic deformation in amorphous solids. Physical Review E, 57(6), p.7192.

[21] Shimizu, F., Ogata, S. and Li, J., 2007. Theory of shear banding in metallic glasses and molecular dynamics calculations. Materials transactions, 48(11), pp.2923-2927.

[22] Henkelman, G. and Jnsson, H., 2000. Improved tangent estimate in the nudged elastic band method for finding minimum energy paths and saddle points. The Journal of chemical physics, 113(22), pp.9978-9985.

[23] Henkelman, G., Uberuaga, B.P. and Jnsson, H., 2000. A climbing image nudged elastic band method for finding saddle points and minimum energy paths. The Journal of chemical physics, 113(22), pp.9901-9904.

[24] Levitas, V.I., 2018. Phase Transformations Under High Pressure and Large Plastic Deformations: Multiscale Theory and Interpretation of Experiments. In Proceedings of the International Conference on Martensitic Transformations: Chicago (pp. 3-10). Springer, Cham.

[25] Levitas, V.I., Chen, H. and Xiong, L., 2018. Phase Transitions and Their Interaction with Dislocations in Silicon. In Proceedings of the International Conference on Martensitic Transformations: Chicago (pp. 83-87). Springer, Cham.

[26] Hahn, E.N., Zhao, S., Bringa, E.M. and Meyers, M.A., 2016. Supersonic dislocation bursts in silicon. Scientific reports, 6, p.26977.

CHAPTER 6. A SPATIAL DECOMPOSITION PARALLEL ALGORITHM FOR A CONCURRENT ATOMISTIC-CONTINUUM SIMULATOR AND ITS PRELIMINARY APPLICATIONS

Reproduced from 'Chen, H., Xu, S., Li, W., Ji, R., Phan, T. and Xiong, L., 2018. A spatial decomposition parallel algorithm for a concurrent atomistic-continuum simulator and its preliminary applications. Computational Materials Science, 144, pp.1-10.'

6.1 Abstract

This paper presents the development of a spatial decomposition parallel algorithm and its implementation into a concurrent atomistic-continuum (CAC) method simulator for multiscale modeling of dislocations in metallic materials. The scalability and parallel efficiency of the parallelized CAC are tested using up to 512 processors. With a modest computational resource, a single crystalline f.c.c. sample containing 10.6 billion atoms is modeled using only $4,809,108$ finite elements in a CAC model at a fraction of the cost of full molecular dynamics (MD). The simulation demonstrates a nearly ideal scalability of the newly parallelized CAC simulator. The parallel efficiency of the newly parallelized CAC is shown to be higher than 90% when using 512 processors in the high performance computing cluster at Iowa State University. This parallel efficiency is comparable to the state-of-the-art atomistic simulator. Moreover, the newly parallelized CAC simulator employing a uniform coarse mesh is capable of capturing important atomistic features of dislocations, including dislocation nucleation, migration, stacking faults as well as the formation of Lomer-Cottrell locks, in a billion-atom system. The spatial decomposition-based parallelization algorithm developed in this work is general and can be transferable to many other existing concurrent multiscale simulation tools.

6.2 Introduction

Many material behaviors and engineering processes are multiscale in nature. Understanding those behaviors and processes across a broad range of length scales are important for the development of novel engineering structures and materials. For example, the plastic deformation of metallic materials spans a wide range of lengths scales ranging from dislocation nucleation at the atomic scale to the formation of multiple slip bands, planar dislocation arrays, and dislocation cells at the microscale, and to the observable effect of permanent deformation at the macroscopic level [1]. It is believed that the multiscale nature of plasticity precludes direct simulations using a formulation appropriate only for one single length scale [2]. For instance, a fully atomistic simulation can provide atomistic details of plastic deformation, such as dislocation interactions, dislocation networks [3,4]. However, it requires a formidable computational cost if a prediction of the macroscopic-level plastic deformation is desired. By contrast, the continuum-level theoretical and computational framework, such as crystal plasticity finite element method (CPFEM), are applicable to simulating the plastic behavior in materials at the macroscopic level. Nevertheless, these approaches lack a predictive capability from the bottom up because they ignore the atomistic discrete nature of materials. In the past decades, taking the advantage of atomistic simulations and continuum-level methods, extensive efforts have been dedicated to the development of multiscale methods for modeling plasticity [5]. Existing multiscale methods generally fall into two categories: sequential and concurrent approaches. In sequential methods, MD simulations are deployed to calibrate the constitutive models and parameters for higher order models. For example, to simulate material plasticity, information about dislocation nucleation, the strength of dislocation junctions, dislocation mobility, and dislocation interactions from atomistic modelling are used to develop short-range interaction rules. These rules are then feed into continuum-level models such as dislocation dynamics [6-8]. One major challenge of such sequential approach is how to average the fine scale information and how to input the averaged information into the higher scale models. In contrast, concurrent methods directly combine a fine-scale description of materials with a higher order material description within one computer model [9-14]. Examples of such concurrent methods for multiscale plasticity include

the coupled atomistic and discrete dislocation formulation [15-19], coupled discrete dislocation and continuum crystal plasticity [2], and the multiresolution molecular mechanics [20]. A comprehensive review of concurrent multiscale methods can be found in Refs. [21, 22].

A direct combination of a fine-scale model, e.g., MD, with a higher order model, such as finite element (FE), within one computational framework introduces an unrealistic numerical interface into the computational model. Due to the mismatch of material descriptions between MD and FE, an atomistic/continuum interface needs to be constructed through a careful numerical implementation. Most of the efforts are then devoted to construct such numerical interface by matching or bridging the atomistic and continuum descriptions such that defects can pass from MD to FE. Different from other concurrent multiscale methods which directly combines MD and FE, the recently developed concurrent atomistic-continuum (CAC) method is based on a new atomistic field formalism that unifies the atomistic and continuum description of materials within one theoretical framework [23]. The coarse-grained (CG) domain in CAC admits dislocation nucleation and migration on the boundaries within the gaps between elements without the need of adaptive mesh refinement [23]. CAC has been successfully applied to simulate a variety of material behaviors, such as slip transfer of dislocations across grain boundaries [24,25], dislocations bowing out from Frank-Read sources [26], dislocation-void interaction [27], dislocations and fracture in strontium titanate [28,29], dynamic crack propagation [30], fast moving dislocations [31], and phonon dynamics in a 1-D polyatomic chain [32]. It is noted that, because the original version of the CAC simulator was not massively parallelized, those applications were mainly limited to material behavior from the atomistic to the nanoscale.

In order to perform large-scale CAC simulation of material behaviors using hundreds of processors, this work aims to develop a massively parallelized CAC simulator that can be applied to predict dislocation activities in a submicron-sized specimen without smearing out its atomistic nature. A spatial decomposition (SD) algorithm is developed and implemented. This algorithm takes full advantage of the local nature of the SD procedure and shows a good parallel efficiency without any limitation on the number of processors. The remainder of this paper is organized as follows. In

section 2, the formulation and the algorithm of the CAC method are briefly reviewed. In section 3, the SD algorithm as well as its efficiency and scalability are presented in details. In section 4, simulations of dislocation activities in a single-crystalline face-centered cubic (f.c.c.) sample with the same computational set-up as that in Ref. [23] is presented to benchmark the newly parallelized CAC. In section 5, the scalability of the algorithm is demonstrated and compared against the fully atomistic simulator, the Large-scale Atomic/Molecular Massively Parallel Simulator (LAMMPS) [33]. In section 6, CAC simulations of the activities of submicron-long dislocation lines in a sample containing billions of atoms are presented. This paper ends with a brief summary and discussion.

6.3 A brief review of the CAC method

The theoretical foundation of CAC is an atomistic field formalism proposed by Chen [34,35], in which a crystalline material is viewed as a continuous collection of lattice points, while embedded within each point is a unit cell containing a group of discrete atoms [36]. Chen [34,35] defined the continuum-level physical quantities from the atomic scale and formulated the microscopic balance equations of the physical quantities including mass density, linear momentum density, and the internal energy density.

It is noted that, the continuum description of those physical quantities is by means of continuous functions in terms of x and t in the physical space. Microscopic dynamic quantities in classical N-body dynamics, on the other hand, are functions of (r, p), i.e., the positions and momenta of atoms, in phase space:

$$r = \left\{ R^k, k = 1, 2, 3, \ldots, n \right\},$$
$$p = \left\{ m^k V^k,\ k = 1, 2, 3, \ldots, n \right\}. \tag{1}$$

where R^k is the position vector and V^k is the velocity of the kth atom, m^k is the atomic mass, and n is the total number of atoms in the system. In the atomistic field formalism, the quantities in the phase space and the physical space descriptions can be linked through utilizing the localization

function δ[34-36], i.e.,

$$\rho(x) = \sum_{k=1}^{n} m^k \delta(R^k - x), \tag{2}$$

$$\rho(x)\, v(x) = \sum_{k=1}^{n} m^k V^k \delta(R^k - x), \tag{3}$$

where ρ is the microscopic local mass density and ρv is the momentum density in physical coordinate. Taking the time derivatives of Eqs. [2-3], Chen [34,35] formulated the microscopic balance equations of the mass and linear momentum. In particular, for a monoatomic crystal under no external forces, the balance equation of linear momentum can be re-written as [23]

$$\rho \ddot{x} = f_{int}(x) \tag{4}$$

where

$$f_{int} = \sum_{k=1}^{n} \sum_{i} \delta\left(R^k - x\right) F_{ik} \tag{5}$$

is the internal force density, F_{ik} is the atomic force acting on atom k by atom i and δ is a Dirac δ-function.

It is daunting to directly compute F_{ik} for all the atomic pairs. Thus, one critical step in numerical implementation of the atomistic field formalism is to efficiently and accurately calculate the internal force density f_{int} in equation [5]. Xiong et al. [23] performed a FE implementation of the atomistic field formalism and the numerical procedure was coined as CAC, which discretizes the computational domain into piecewise elements. Gaussian quadrature was deployed to perform the spatial integration to calculate the internal force density [23]. Later, Yang et al. [28] and Xu et al. [24] modified the quadrature rules and demonstrated that the generalized stacking fault energy, core structure and the stress field around a mixed dislocation in CAC models are comparable with that from MD. In this paper, the integration scheme in Ref. [24] is employed. A computational domain is discretized into piecewise elements (Fig. 1). Each element is in a rhombohedral shape and contains a collection of lattice cells. The displacement within the element is approximated by

$$u = \Phi_\xi(x)\, U_\xi \tag{6}$$

where U_ξ are finite element nodal displacements, $\Phi_\xi(x)$is the standard tri-linear shape function. In the numerical integration scheme, the internal force on node ξ is calculated as follows [23, 24]:

$$f_{int}^{\xi} = \frac{\sum_\mu \omega_\mu \Phi_{\xi\mu} F^\mu}{\sum_\mu \omega_\mu \Phi_{\xi\mu}} \tag{7}$$

where F^μ is the force on the integration point μ, ω_μ is the weight, and $\Phi_{\xi\mu}$ is the value of the shape function Φ_ξ at the integration point μ. The weight ω_μ is determined by the number of atoms that the integration point represents. In details, for those integration points located on nodal sites, $\omega_\mu = 1$; for those on the element edges, $\omega_\mu = N_l - 2$; for those on the surface, $\omega_\mu = (N_l - 2)^2$; and for those within the interior of the elements, $\omega_\mu = (N_l - 2)^3$. Here, N_l is the number of atoms along the edge of each coarse element. It is clear that the CAC model will degenerate into full MD simulations when $N_l = 2$ *and* $\mu = 8$. Such an atomic-scale mesh is referred as the finest mesh in CAC method and will function as a fully atomistic domain. In this paper, uniform coarse elements are used to discretize the material sample and the number of integration points within each element is set as $\mu = 27$, which corresponds to the '1NN' case in Ref. [24]. For $N_l \leq 3$, a collocation integration procedure is used and $\mu = 8$.

6.4 Parallelization Algorithm

The CAC simulator is parallelized through the Message Passing Interface (MPI) using the spatial decomposition algorithm. The main idea of this algorithm is to evenly divide the total volume of the system into small boxes with equal volume, e.g., the red solid box in Fig. 1. Each small box is assigned to a processor. Specifically, we use a regular 3-dimensional meshing topology [33] in which the simulation box is divided into D_α parts along α ($\alpha = x, y, z$) direction. The total number of processors is $p = D_x D_y D_z$ and each processor is indexed as$d = d_x D_y D_z + d_y D_z + d_z$. The sub-box owned by the d-th processor is indexed as d_α along the α direction . Element i with the center position $r_{ic} = (r_{ix},\ r_{iy}, r_{iz}) = \frac{1}{m}\Sigma r_{in}$ is mapped to processor $d(r_i)$ in an array. The computational

domain along each direction is subdivided into D_x,D_y and D_z in an equal size

$$\begin{cases} d\left(r_{ic}\right) = d_x\left(r_{ix}\right) D_y D_z + d_y\left(r_{iy}\right) D_z + d_z\left(r_{iz}\right), \\ d_\alpha\left(r_{i\alpha}\right) = \left[\frac{r_{i\alpha} D_\alpha}{L_\alpha}\right] \qquad\qquad (\alpha = x, y, z), \end{cases} \tag{8}$$

in which L_α is the simulation box size along the α direction. The box belonging to each processor is called the "local box" of that processor in comparison with the enlarged "ghost box" introduced later.

Each processor computes and updates the forces, positions and velocities of FE nodes within its own domain at each time step. Elements moving outside of the box will be assigned to the new box during the simulations. The information of elements in the neighboring boxes is sent to the local box through MPI_Send and MPI_Irecv command, i.e., the information of some elements in the red dotted box inside the nearby processors is sent to the local processor for computing the force on the nodes of the local elements. Here an enlarged box is defined and referred as a "ghost box" [33] which has all dimensions larger than the local box of l_c (Fig. 1). It should be pointed out that the data structure and the communication in the spatial decomposition is local in nature. This will in principle lead to a high parallel efficiency if each processor contains a similar number of elements. In contrast, in other parallel algorithms, such as the force decomposition method [33, 37, 38], globalized vectors are used and the communication of the globalized vectors (all-to-all) is required. As a consequence, the simulation employing such force decomposition becomes significantly slow when the number of degree of freedom increases. This leads to a decrease of the parallel efficiency in large-scale simulations [33].

In each processor, three dimensional arrays are constructed for storing the positions, velocities and forces of FE nodes. The first dimension of each array is the number of elements, the second is the number of nodes per element (8 for $3D$ and 4 for $2D$), and the third is 3 for 3D or 2 for 2D, respectively. Nodal positions of elements with their center positions falling into the ghost box are sent from the neighboring processors and updated at each time step. Those nodal positions received from neighboring boxes are directly inserted at the end of the local vectors without sorting. The lists of elements received from the nearby processors are recorded in the following several time

steps. The neighbor lists will be only updated when any of the FE nodal displacement is larger than a skin parameter. Such a technique has been employed in the MD simulator LAMMPS [33]. The positions of the atoms within each element are interpolated using the shape functions in Eq. 3 [23-24].

The parallelization starts with reading the input data file. Figure 2 shows that the FE nodal coordinates are read by the master processor, noted as CPU_0, step by step to avoid creating global data structures in all of processors. At each step, CPU_0 reads a fixed number of element coordinates: l_n. In this work, we choose l_n as 1024 in order to balance the input reading and the information communication between processors. Thereafter, CPU_0 will broadcast the data to all the other processors, noted as $CPUs$, in the communication *world* using the MPI_Bcast command. In each processor, a vector of the same size of l_n is allocated in order to receive data broadcasted by CPU_0. With this information, each processor will determine whether the position of the element center, r_{ic} , falls into its own local box. Those elements falling into the local box will be assigned to the processor and the information associated with them is stored at the end of the existing position vectors. In this way, only local data structures will be needed. The same strategy is applied to the output of results during the simulation.

Figure 3 shows the communication scheme between processors [33]. This strategy is the same as what has been implemented in LAMMPS because each element can be considered as a "coarse atom" [39]. Here the elements received from nearby processors are noted as ghost elements. The cutoff for ghost elements is set as $r_s = r_c + \max(l_c)$. Firstly, the positions of FE nodes falling within the cutoff length r_s of CPU_1's box is sent to CPU_2 as shown in Fig. 3a followed by the reverse communication. The same procedure is repeated along the north/south direction in Fig. 3b. The only difference is that messages sent to the adjacent CPU now contain not only local elements but also ghost elements received from previous communications. This process is then repeated along the up/down dimension. When $r_s > L_\alpha/D_\alpha$, here L_α and D_α have the same meaning as that in Eq.8, those elements in $\left[\frac{r_s D_\alpha}{L_\alpha}\right]+1$ neighboring boxes are needed. Thus the communication procedure will be performed for $\left[\frac{r_s D_\alpha}{L_\alpha}\right]+1$ times. The advantage of this scheme is to minimize the communication

data [33] although the coding process becomes tedious. That is, each processor acquires only the elements that are within a distance r_s of its "local box". All the received elements are placed as contiguous data into the local data structure without rearranging. During the communication, a full scan of the data structure is only conducted when there is a need to decide the information of which element should be sent. Such a scan creates a list of elements that compose of each message. During all the other timesteps, the lists can be used to directly sort the referenced elements and buffer up the messages in an efficient manner.

Then the neighbor list of integration points is constructed for the evaluation of the internal force density. Once the neighbor list is constructed, the internal force density associated with each integration point can be calculated. The neighbor list construction in CAC is mainly divided into two steps. The first step is to build the element neighbor list using a link-cell scheme. The cutoff for the element neighbor list is the same as that used for communication: r_s. The bin size used here is $r_s/2$ which maximizes the efficiency of the neighbor list construction [33]. The second step is to build the neighbor list of integration points through searching the atoms interpolated from the neighboring elements. Since each element contains several thousands of atoms, interpolation of all atoms inside all elements will be demanding. Here, instead of performing a full-domain interpolation, the second step is further divided into two sub steps. Before going into details, we introduce one parameter: $I = r_c + l_c/2$, referred as the influence radius of an element (Fig. 1). The distance between the atoms outside this radius and the atoms interpolated from this element is larger than r_c and thus there will be no interaction between them. The process for finding the integration point i in Fig. 1 is described as following. Firstly, the distance between i and the center position of each neighboring element will be calculated. If the distance is larger than I, the atoms inside this element will not be interpolated. For example, the distance between the centroid of element 1 and the integration point p in Fig. 1 is larger than I. This means that the distance between any of atoms within element 1 and the integration point p will be larger than r_c. In this situation, all the atoms within element 1 will not be in the neighbor list of point p and will not be interpolated. Under this treatment, only the positions of the atoms falling into the elements in

yellow (Fig. 1) will be interpolated for constructing the neighbor list of the integration point p . The next sub-step is to further subdivide each yellow element in Fig. 1 into n equal-sized segments along each direction and n^2 (n^3 for 3D problems) smaller sub-elements in total. Each sub-element has an influential radius: $I_{sub} = r_c + l_c/(2n)$. When the distance between the sub-elements and the integration points is smaller than I_{sub} , the positions of the atoms will be interpolated for neighbor list construction. As such, the interpolation in the neighbor elements will be only performed in those sub-elements in green. Figure. 4 shows that the neighbor list construction time, t_n , changes with the splitting number n along each direction. The testing computer model used to produce the data in Fig. 4 contains 10.6 billion atoms and is discretized into 3,145,963 coarse elements [23]. Each element contains $3,375$ atoms. Using 512 processors, the minimum neighbor building time is 2.1 seconds for this model. It is found that t_n first decreases at an order of 3 , which is the same as the number of elements to be interpolated, and then increases slightly with the increase of the splitting number n. The increase of the neighbor list construction time is due to the time spent for checking the distances between integration points and sub-elements when the splitting number n become larger. With this information, an optimized value for element splitting can be determined for the neighbor list construction.

6.5 Scalability of the massively parallelized CAC simulator

To investigate the scalability of the newly developed parallel algorithm, CAC models for cubic f.c.c. samples with a dimension of $0.1\mu m \times 0.1\mu m \times 0.1\mu m$ and $0.5\mu m \times 0.5\mu m \times 0.5\mu m$ are tested. The CAC model for a cuboid sample ensures that each processor contains similar number of coarse elements and avoids unequal workload among different processors. The $0.5\mu m \times 0.5\mu m \times 0.5\mu m$ sample as shown in Fig. 5 is the largest computer model explored in this work. This model contains 10.566 billion atoms and is discretized into $4,809,108$ coarse elements. Each element contains 2197 atoms. The timestep is set as 5fs. Figure. 6 shows the relationship between the number of processors and the averaged time cost for each timestep in different models containing different

number of elements. The time cost is averaged over the total simulation time which includes the reading, initialization, the neighbor list construction and also the FE nodal force calculation. The computing timing of CAC using a single processor is taken as a reference point for calculating the parallel efficiency when memory for single processor is large enough to store all global vectors. It should be noted that, for problems when nel (number of elements) $= 4,809,108$, the memory associated with one single processor is not enough and simulations should start with a certain number of processors (for example, 16 for $nel = 310,425$). The reference points are then the timings of the starting number of processors. While the number of processors p increases, the size of the domain covered by the "local box" decreases. This leads to a higher volume ratio between the ghost box and the local box. That is, the ratio between the number of the elements containing in the ghost box and that in local box: R, increases. For example, for $nel = 38,064$ in Fig. 6, $R = 1$ when $P = 32$ and $R = 10$ when $P = 512$. This will induce a small decrease of the parallel efficiency. However, the spatial domain decomposition algorithm still retains a parallel efficiency of 85% when $P = 512$. When $nel \geq 310,425$ in Fig. 6, a parallel efficiency of 92% can be achieved when 512 processors are used. This is the maximum number of processors we can access using our computing resource. Nevertheless, since all data sets and communications are localized in the SD algorithm, the parallel efficiency remains high when $P > 512$ and will be comparable to that in MD simulations using LAMMPS [33].

Figure 7 presents the linear relationship between nel and the total CPU time, $p * t_{su}$. Here t_{su} is the time spent by each processor. This linear relationship means that the total computational time is determined by the total number of elements. For all the cases in Fig. 7, the communication time doesn't exceed 8% of the total simulation time and more than 90% of the simulation time is spent in the interpolation of the integration points, calculation of nodal force and updating nodal positions. This implies that there will be no limit of the size of models as long as we can have access to a large number of processors [33]. The high parallel efficiencies ensures that the SD algorithm presented in this work can be at the same level as that in many existing massively parallelized MD simulator [33].

6.6 Comparison with LAMMPS

In addition to the CAC computer model, the algorithm can also be applied to perform MD simulations when the coarse mesh in the CAC model is reduced to the atomic scale [23]. In this situation, a comparison between the CAC simulation time and LAMMPS [33] using exactly the same hardware [40] is carried out. In a 1000-timestep simulation of a $(0.1\mu m)^3$ cubic sample containing $83,626,608$ atoms using 16 nodes in the Condo cluster at Iowa State University [41], LAMMPS took 454.8s and the CAC took 480.2s. For a uniform coarse mesh in CAC, the computational workload ratio between the coarse-grained model and MD simulations can be defined as below

$$R_{up} = \frac{total\ number\ of\ integration\ points}{total\ nmber\ of\ atoms} \tag{8}$$

Here the theoretical speed-up is defined as $S_{theory} = 1/R_{up}$. The actual speed-up of the parallelized CAC with respect to various R_{up}, closely follows the theoretical speed-ups in general, as shown in Fig. 8. The largest speed-up we obtain is 33.3 when the uniform coarse element (2197 atoms per element) is used in CAC.

1. **A simple validation**

CAC computer models of notched single-crystal copper specimens in a previous work [23] are used to validate the correctness of the newly implemented parallel algorithm in CAC. A Lennard-Jones (L-J) potential is used, with parameters $\epsilon_0 = 0.167ev$ and $\sigma_0 = 2.3151$Å. This model contains $1,423,107$ atoms and is discretized into $4,149$ elements with each element containing 343 atoms. Figure 9 presents the atomic rearrangements, dislocation structures, and stacking faults from the newly parallelized CAC and also from MD. Two dislocations are emitted from the notch tips and propagate into the specimen interior along {1 1 1} planes. The same non-symmetric dislocation nucleation behavior is captured here [23]. Also, the Lomer-Cottrell or stair-rod locks [41] are formed, which hinders further dislocation glide on the two slip planes and provides a barrier to other dislocations [23]. This is also found in MD simulations [23]. We test this model with random number of processors and results are the same. This demonstrates that the results are independent

of the number of processors and the communications between processors are reliable in the massively parallelized CAC code.

6.7 Numerical Examples

CAC furnished with the newly developed spatial decomposition algorithm is used to simulate dislocations in a $0.25\mu m * 0.25\mu m * 0.53\mu m$ cubic sample with two notches on both sides as shown in Fig. 10. This model contains $2,307,616,753$ atoms and is discretized into $1,050,349$ elements with each element containing 2197 atoms. A constant velocity of $1m/s$ is applied (corresponding to a strain rate on the order of $10^6 s^{-1}$) on the two vertical (z direction) ends of the sample with the other surfaces traction free.

Figure 11 shows that dislocations nucleate around the notches [42]. Through the Burgers vector analysis using the geometric method in OVITO [4], the emitted dislocations are found to be partial dislocations with Burgers vector $\frac{1}{6}[11\overline{2}]$ in the $< 111 >$-plane and $\frac{1}{6}[\overline{1}2\overline{1}]$ in the $(\overline{1}11)$-plane. Dislocations migrate in the sample with different velocities due to the free surface and elastic interactions between dislocations [4]. During their migrations, the curvature of the dislocation lines decreases to reduce the line energy of dislocations [43]. Eventually, the two dislocations lines interact with each other as shown in Fig. 11e. The interaction angle was measured as 18.2^o , which remains constant until the two dislocations formed a Lomer-Cottrell lock [41].

It should be noted that dislocation lines along the thickness direction, i.e., the y-direction, insects two free surfaces in the xz plane. In order to characterize the effects of free surfaces on the dislocation core stress field, the shear stress distribution around the dislocation core at $y = -200,\ 0,\ 900\ and\ 1200$Å is quantified and presented in Figure 12. It is seen that the positive shear stress component decreased when the dislocation core is approaching the free surface. That is, the maximum positive shear stress decreases from $\sim 0.8GPa$ when $y = -200$Å to $\sim 0.2GPa$ when $y = 1200$Å. Clearly, the stress around a dislocation core gradually decays when it gets closer to a free surface. This result implies that dislocation core stress field in a finite-sized material sample is actually size-dependent and will be only approaching the analytical solution of a dislocation core

embedded within an infinite media when the core is reasonably far away, e.g. $120nm$ in this work, from a free surface.

In order to demonstrate that the applicability of the newly parallelized CAC code to different material systems in which use different interatomic potentials, one set of massively parallelized CAC simulation using an embedded atom method (EAM) force field [44] is performed. This simulation employs the Mishin-embedded atom method force field for single crystalline copper. In the CAC simulator, the electron charge density is calculated only on the nodes of elements. The electron charge density of those atoms within the element is interpolated from the electron charge density on the FE nodes. A single crystalline cubic f.c.c. sample in a dimension of 70nm$\times$70nm$\times$70nm containing $54,683,330$ atoms is discretized into $24,890$ coarse elements (the Inset pictures in Fig. 13). A constant velocity of $1m/s$ is applied on the two ends of the sample with the other surfaces traction free. The dislocations activities are analyzed using the dislocation extraction algorithm in OVITO [45]. Figure 13 shows that dislocations nucleate from the free surfaces and propagate into the interior of the sample. Similar with the simulation from the CAC model using the L-J potential, dislocations also have Burges vector $\frac{1}{6}$ [112], which are consistent with those found in the full MD simulations of Cu under tension [46]. Those dislocations interact with each other, form stair-rod lock structure [45] and then a dislocation forest as those in MD simulations [4]. This preliminary simulation demonstrates that, despite the approximations introduced by the coarse mesh in CAC, the atomistic nature associated with dislocation nucleation, interactions, and the formation of sessile structures have been captured at a fraction of the cost of full MD simulations.

6.8 Summary and discussions

In this work, a SD parallel algorithm for a multiscale simulator, CAC, is developed and implemented. Results obtained using the newly parallelized CAC simulator are directly compared with those from MD simulations. It shows that the newly developed CAC simulator can effectively reproduce dislocation nucleation, migration and the formation of Lomer-Cotrell lock formation as that in MD simulations. Furthermore, the parallel algorithm has been tested in CAC using different

number of processors for different models. Using only 512 processors, CAC furnished with this new algorithm exhibits an optimal scalability in computer models which contains up to $4,809,108$ elements for $10,565,610,276$ atoms. This is beyond the reach of classical MD simulator using the same computational resource. The parallel efficiency is shown to be more than 90% and is compared with a well-established atomistic simulator, LAMMPS. For the CAC models with the atomic-scale finite element meshes which reproduce the full MD simulation results, the parallel algorithm achieves 97% efficiency of LAMMPS. To demonstrate the capability of the newly parallelized CAC simulator, dislocation activities in a large sample containing $2,307,616,753$ atoms are simulated. The maximum positive shear stress around a dislocation core in the finite-sized sample was found to gradually decay when it get closer the free surface. It approaches the analytical solution for the stress field around a dislocation core embedded in an infinite media when the core is at least $\sim 120nm$ away from the free surfaces.

It should be noted that the majority of existing concurrent multiscale method is based on domain decomposition [2, 17-23], the present SD parallel algorithm can be applied to those methods and provide a general framework for parallelizing many other multiscale materials simulators. In order to use CAC to simulate more complicated phenomena such as dislocation interaction with obstacles such as voids or grain boundaries, the atomic-scale finite element mesh nearby the obstacles needs to be combined with coarse elements. The computer models with non-uniform meshes with different element sizes in the newly parallelized CAC code will be tested in our future work.

References

1. McDowell, D. L. (2010). A perspective on trends in multiscale plasticity. *International Journal of Plasticity*, *26*, 1280-1309.

2. Wallin, M., Curtin, W. A., Ristinmaa, M., and Needleman, A. (2008). Multi-scale plasticity modeling: Coupled discrete dislocation and continuum crystal plasticity. *Journal of the Mechanics and Physics of Solids*, *56*, 3167-3180.

3. Yamakov, V., Wolf, D., Phillpot, S. R., Mukherjee, A. K., and Gleiter, H. (2002). Dislocation processes in the deformation of nanocrystalline aluminium by molecular-dynamics simulation. *Nature materials*, *1*, 45-49.

4. Buehler, M. J., Hartmaier, A., Gao, H., Duchaineau, M., and Abraham, F. F. (2004). Atomic plasticity: description and analysis of a one-billion atom simulation of ductile materials failure. *Computer Methods In Applied Mechanics And Engineering*, *193*, 5257-5282.

5. Roters, F., Eisenlohr, P., Hantcherli, L., Tjahjanto, D. D., Bieler, T. R., and Raabe, D. (2010). Overview of constitutive laws, kinematics, homogenization and multiscale methods in crystal plasticity finite-element modeling: Theory, experiments, applications. *Acta Materialia*, *58*, 1152-1211.

6. Amodeo, R. J., and Ghoniem, N. M. (1990). Dislocation dynamics. I. A proposed methodology for deformation micromechanics. *Physical Review B*, *41*, 6958.

7. Amodeo, R. J., and Ghoniem, N. M. (1990). Dislocation dynamics. II. Applications to the formation of persistent slip bands, planar arrays, and dislocation cells. *Physical Review B*, *41*, 6968.

8. Van der Giessen, E., and Needleman, A. (1995). Discrete dislocation plasticity: a simple planar model. *Modelling and Simulation in Materials Science and Engineering*, *3*, 689.

9. Broughton, J. Q., Abraham, F. F., Bernstein, N., and Kaxiras, E. (1999). Concurrent coupling of length scales: methodology and application. *Physical review B*, *60*, 2391.

10. Cai, W., de Koning, M., Bulatov, V. V., and Yip, S. (2000). Minimizing boundary reflections in coupled-domain simulations. *Physical Review Letters*, *85*, 3213.

11. Zhou, M., and McDowell, D. L. (2002). Equivalent continuum for dynamically deforming atomistic particle systems. *Philosophical Magazine A*, *82*, 2547-2574.

12. Wagner, G. J., and Liu, W. K. (2003). Coupling of atomistic and continuum simulations using a bridging scale decomposition. *Journal of Computational Physics*, *190*, 249-274.

13. Xiao, S. P., and Belytschko, T. (2004). A bridging domain method for coupling continua with molecular dynamics. *Computer methods in applied mechanics and engineering*, *193*, 1645-1669.

14. Klein, P. A., and Zimmerman, J. A. (2006). Coupled atomistic–continuum simulations using arbitrary overlapping domains. *Journal of Computational Physics*, *213*, 86-116.

15. Shilkrot, L. E., Curtin, W. A., and Miller, R. E. (2002). A coupled atomistic/continuum model of defects in solids. *Journal of the Mechanics and Physics of Solids*, *50*, 2085-2106.

16. Shilkrot, L. E., Miller, R. E., and Curtin, W. A. (2002). Coupled atomistic and discrete dislocation plasticity. *Physical review letters*, *89*, 025501.

17. Shilkrot, L. E., Miller, R. E., and Curtin, W. A. (2004). Multiscale plasticity modeling: coupled atomistics and discrete dislocation mechanics. *Journal of the Mechanics and Physics of Solids*, *52*, 755-787.

18. Miller, R. E., Shilkrot, L. E., and Curtin, W. A. (2004). A coupled atomistics and discrete dislocation plasticity simulation of nanoindentation into single crystal thin films. *Acta Materialia*, *52*, 271-284.

19. Dewald, M., and Curtin, W. A. (2006). Analysis and minimization of dislocation interactions with atomistic/continuum interfaces. *Modelling and Simulation in Materials Science and Engineering*, *14*, 497.

20. Biyikli, E., and To, A. C. (2017). Multiresolution molecular mechanics: Implementation and efficiency. *Journal of Computational Physics*, *328*, 27-45.

21. Miller, R. E., and Tadmor, E. B. (2007). Hybrid continuum mechanics and atomistic methods for simulating materials deformation and failure. *MRS bulletin*, *32*, 920-926.

22. Miller, R. E., and Tadmor, E. B. (2009). A unified framework and performance benchmark of fourteen multiscale atomistic/continuum coupling methods. *Modelling and Simulation in Materials Science and Engineering*, *17*, 053001.

23. Xiong, L., Tucker, G., McDowell, D. L., and Chen, Y. (2011). Coarse-grained atomistic simulation of dislocations. *Journal of the Mechanics and Physics of Solids*, *59*, 160-177.

24. Xu, S., Che, R., Xiong, L., Chen, Y., and McDowell, D. L. (2015). A quasistatic implementation of the concurrent atomistic-continuum method for FCC crystals. *International Journal of Plasticity*, *72*, 91-126.

25. Xu, S., Xiong, L., Chen, Y., and McDowell, D. L. (2016). Sequential slip transfer of mixed-character dislocations across Σ3 coherent twin boundary in FCC metals: a concurrent atomistic-continuum study. *npj Computational Materials*, *2*, 15016.

26. Xu, S., Xiong, L., Chen, Y., and McDowell, D. L. (2016). An analysis of key characteristics of the Frank-Read source process in FCC metals. *Journal of the Mechanics and Physics of Solids*, *96*, 460-476.

27. Xiong, L., Xu, S., McDowell, D. L., and Chen, Y. (2015). Concurrent atomistic–continuum simulations of dislocation–void interactions in fcc crystals. *International Journal of Plasticity*, *65*, 33-42.

28. Yang, S., Xiong, L., Deng, Q., and Chen, Y. (2013). Concurrent atomistic and continuum simulation of strontium titanate. *Acta Materialia*, *61*, 89-102.

29. Yang, S., and Chen, Y. (2015, March). Concurrent atomistic and continuum simulation of bi-crystal strontium titanate with tilt grain boundary. In *Proc. R. Soc. A* (Vol. 471, No. 2175, p. 20140758). The Royal Society.

30. Deng, Q., and Chen, Y. (2013). A coarse-grained atomistic method for 3D dynamic fracture simulation. *International Journal for Multiscale Computational Engineering*, *11*.

31. Xiong, L., Rigelesaiyin, J., Chen, X., Xu, S., McDowell, D. L., and Chen, Y. (2016). Coarse-grained elastodynamics of fast moving dislocations. *Acta Materialia*, *104*, 143-155.

32. Xiong, L., Chen, X., Zhang, N., McDowell, D. L., and Chen, Y. (2014). Prediction of phonon properties of 1D polyatomic systems using concurrent atomistic–continuum simulation. *Arch. Appl. Mech*, *84*, 1665-1675.

33. Plimpton, S. (1995). Fast parallel algorithms for short-range molecular dynamics. *Journal of computational physics*, *117*, 1-19.

34. Chen, Y. (2006). Local stress and heat flux in atomistic systems involving three-body forces. *The Journal of chemical physics*, *124*.5, 054113.

35. Chen, Y. (2009). Reformulation of microscopic balance equations for multiscale materials modeling. *The Journal of chemical physics*, *130*, 134706.

36. Chen, Y., and Lee, J. (2005). Atomistic formulation of a multiscale field theory for nano/micro solids. *Philosophical Magazine*, *85*(33-35), 4095-4126.

37. Pavia, F., and W. A. Curtin. "Parallel algorithm for multiscale atomistic/continuum simulations using LAMMPS." *Modelling and Simulation in Materials Science and Engineering* 23.5 (2015): 055002.

38. Biyikli, Emre, and Albert C. To. "Multiresolution molecular mechanics: Implementation and efficiency." *Journal of Computational Physics* 328 (2017): 27-45.

39. Hardy, R. J. (1982). Formulas for determining local properties in molecular-dynamics simulations: Shock waves. *The Journal of Chemical Physics*, *76*, 622-628.

40. http://hpcgroup.public.iastate.edu/HPC/Condo/homepage.html

41. Yamakov, V., Wolf, D., Phillpot, S. R., and Gleiter, H. (2003). Dislocation–dislocation and dislocation–twin reactions in nanocrystalline Al by molecular dynamics simulation. *Acta materialia*, *51*, 4135-4147.

42. Izumi, S., and Yip, S. (2008). Dislocation nucleation from a sharp corner in silicon. *Journal of Applied Physics*, *104*, 033513.

43. Peter M. Anderson, John P. Hirth and Jens Lothe. Theory of Dislocations. Cambridge University Press. 3 edition. 2016.

44. Mishin, Y., Mehl, M. J., Papaconstantopoulos, D. A., Voter, A. F., and Kress, J. D. (2001). Structural stability and lattice defects in copper: Ab initio, tight-binding, and embedded-atom calculations. *Physical Review B*, *63*, 224106.

45. Stukowski, A. (2009). Visualization and analysis of atomistic simulation data with OVITO–the Open Visualization Tool. *Modelling and Simulation in Materials Science and Engineering*, *18*, 015012.

46. Shabib, I., & Miller, R. E. (2009). Deformation characteristics and stress–strain response of nanotwinned copper via molecular dynamics simulation. *Acta Materialia*, *57*, 4364-4373.

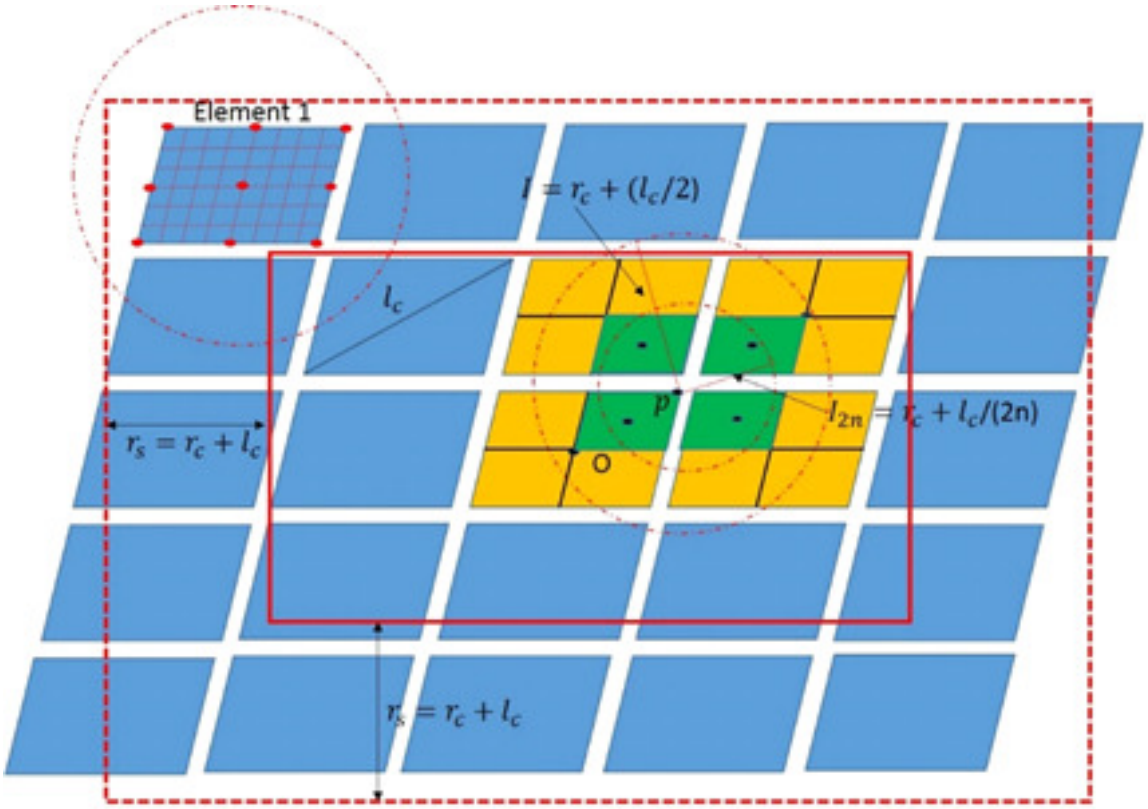

Figure 6.1 The schematic sketch for building the neighbor list of an integration point p in an element centered at point O. The domain bounded by the solid red lines is referred as a "local box" handled by a local processor. The domain bounded by the dotted red line is referred as a "ghost box". The information associated with the elements (elements in blue) falling into the "ghost box" but out of the "local box" is sent to the local processor. Here l_c is the element size which is the largest length of the diagonals and r_c is the cutoff of the interatomic potential. The domain in yellow covers the atomic interaction range associated with an integration point p. In particular, within this interaction range, the instantaneous position of each atom falling into the domain in green is interpolated from the FE nodal positions.

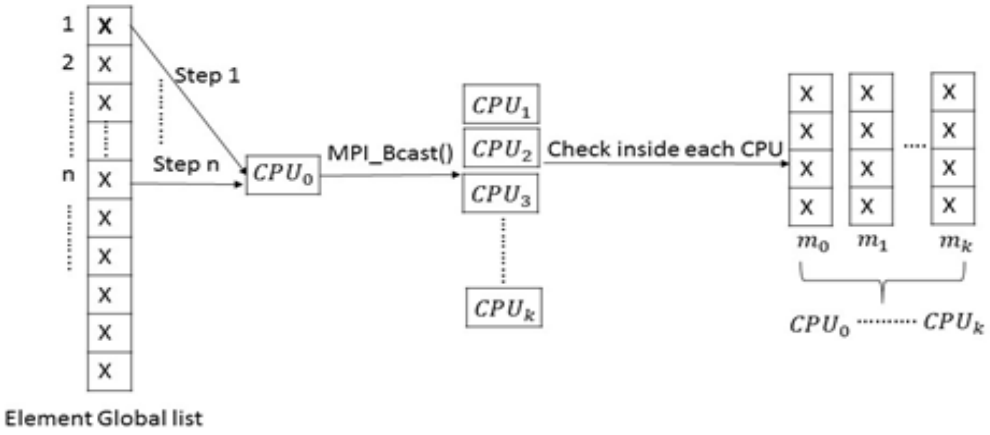

Figure 6.2 The process of reading input file and the information broadcasting to all the processors.

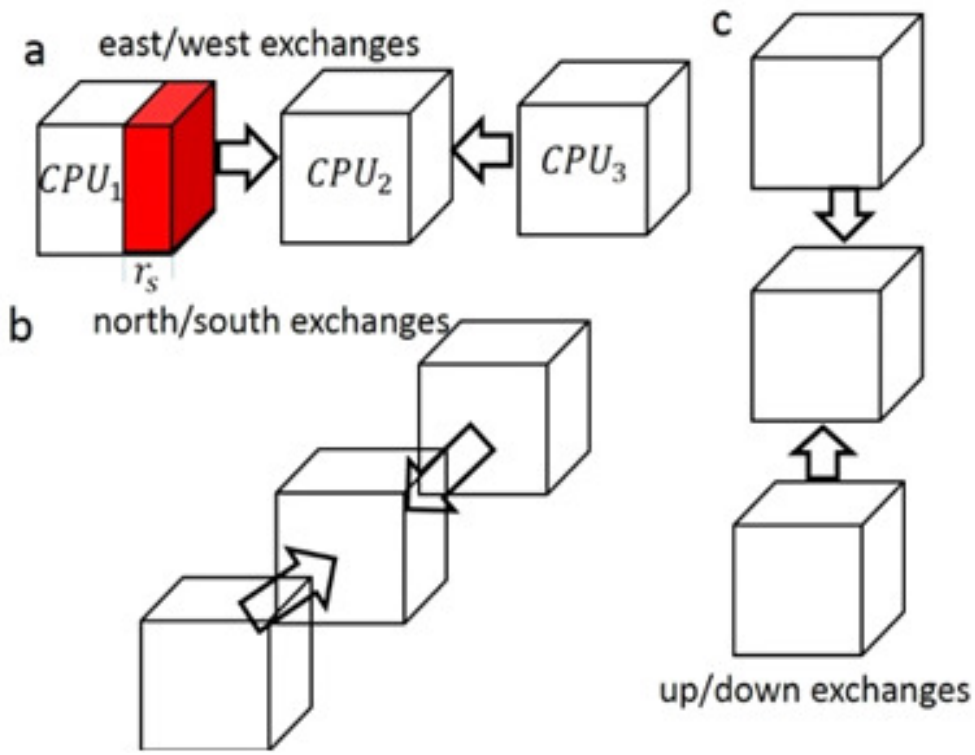

Figure 6.3 A scheme of the communications between processors in the parallelized CAC simulator.

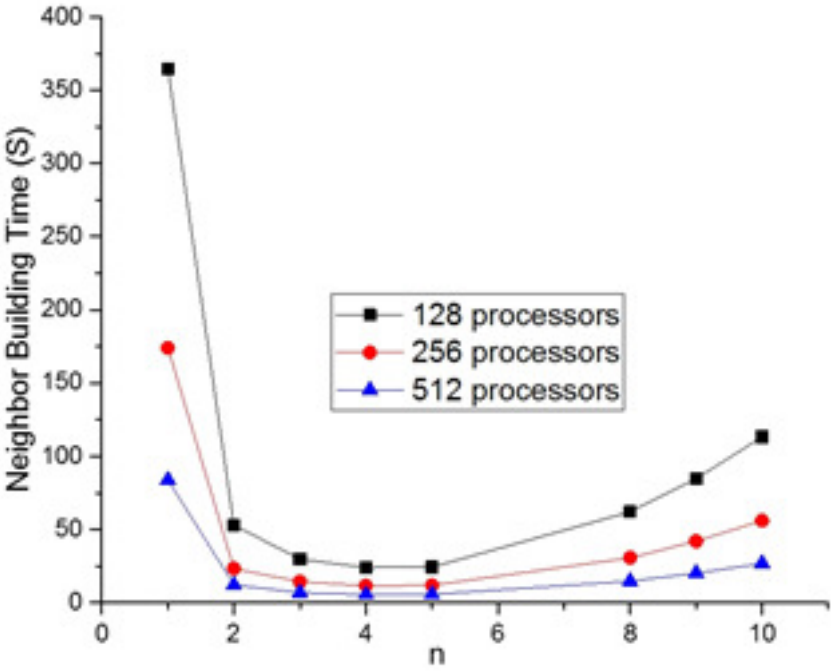

Figure 6.4 The relation between the splitting number n and the time for the neighbor list construction.

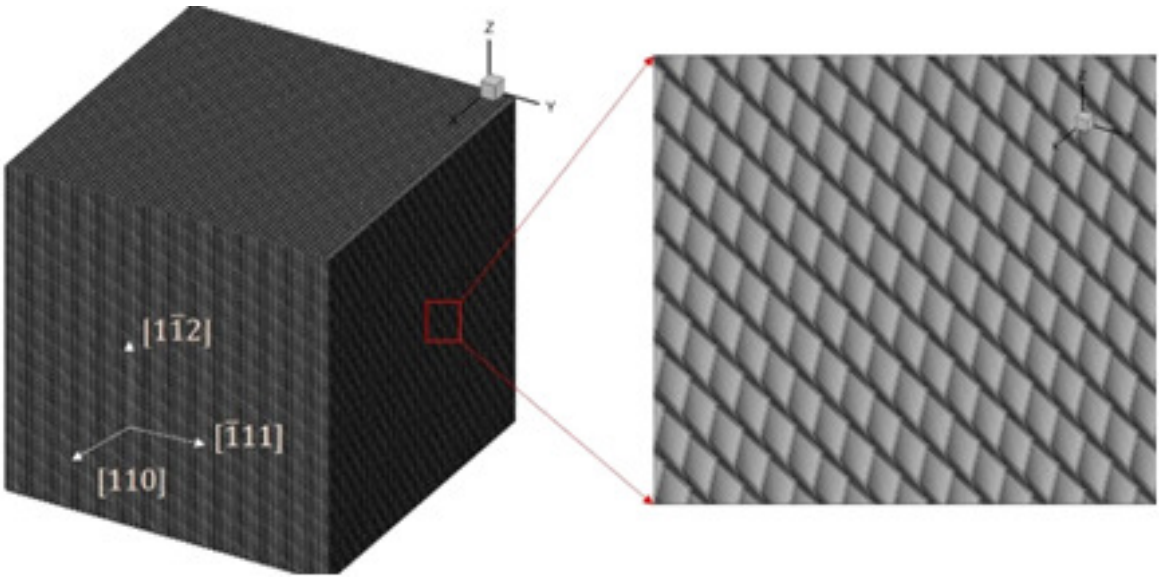

Figure 6.5 CAC model of a $0.5\mu m$ cubic sample used to test the scalability.

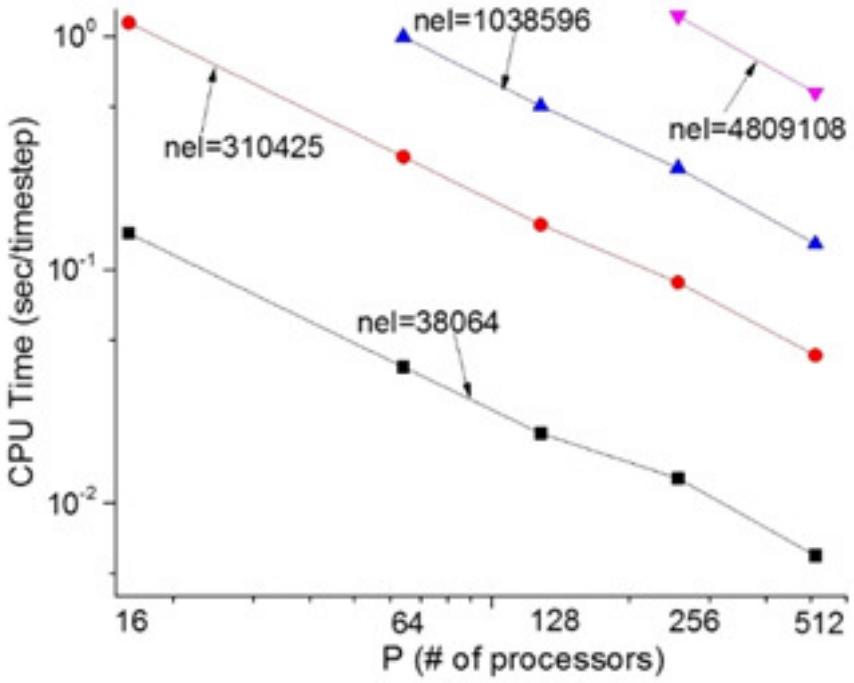

Figure 6.6 CPU timing (seconds/timestep) versus the number of processors used for different CAC computer models containing different number of elements.

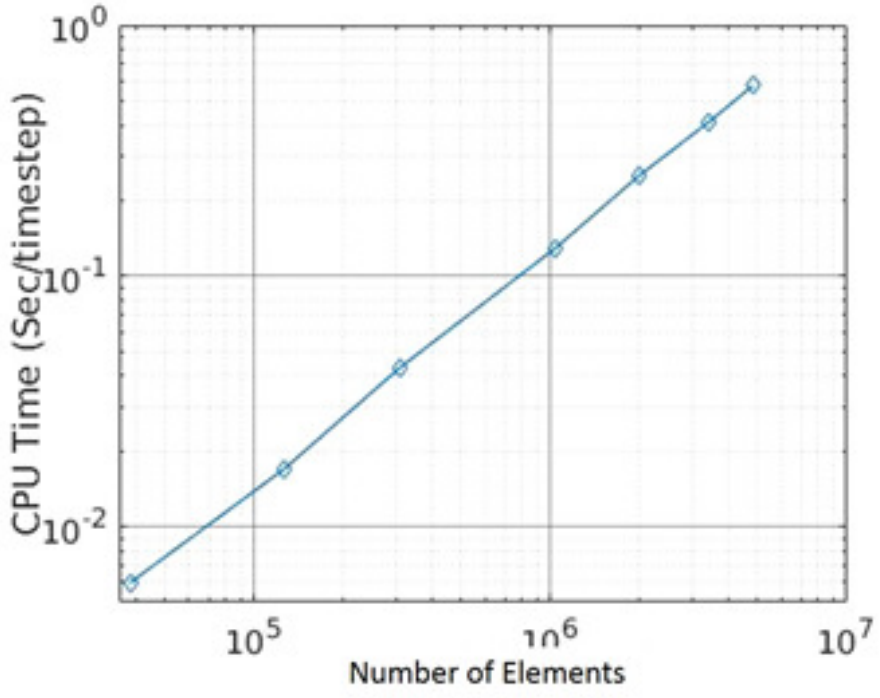

Figure 6.7 A relationship between the CPU timing and the number of elements assigned to each processor.

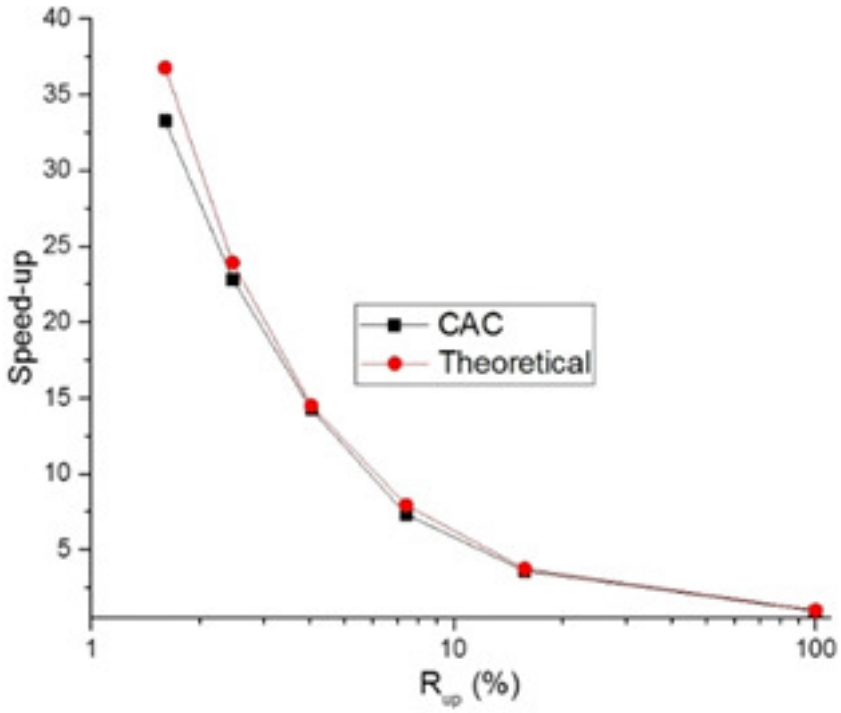

[h!tb]

Figure 6.8 The speed-up of the CAC model with respect to computational workload ratio (R_{up})

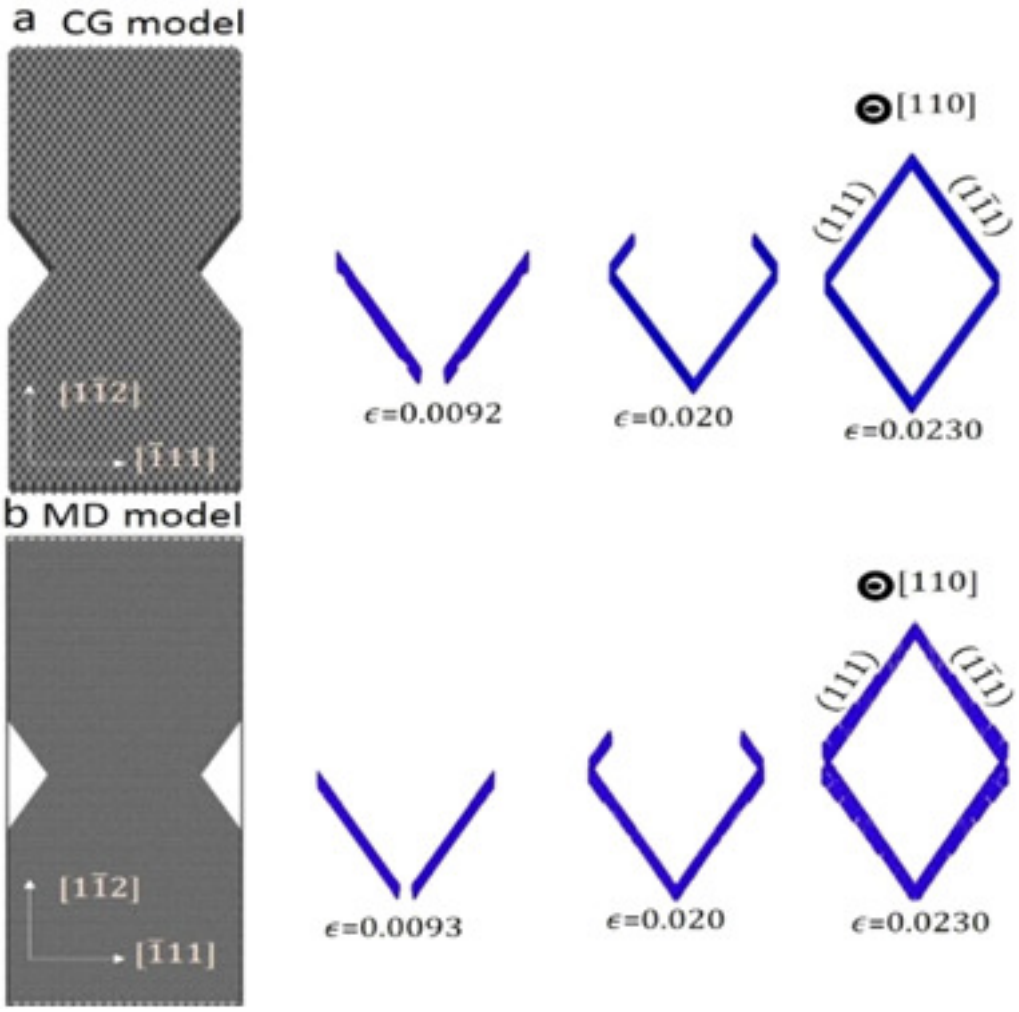

Figure 6.9 Snapshots of atomic arrangements, dislocations and stacking faults. (a) Results from the newly parallelized CAC simulation. (b) Results from MD simulation. Here only the atoms associated with dislocations and stacking faults are displayed in blue.

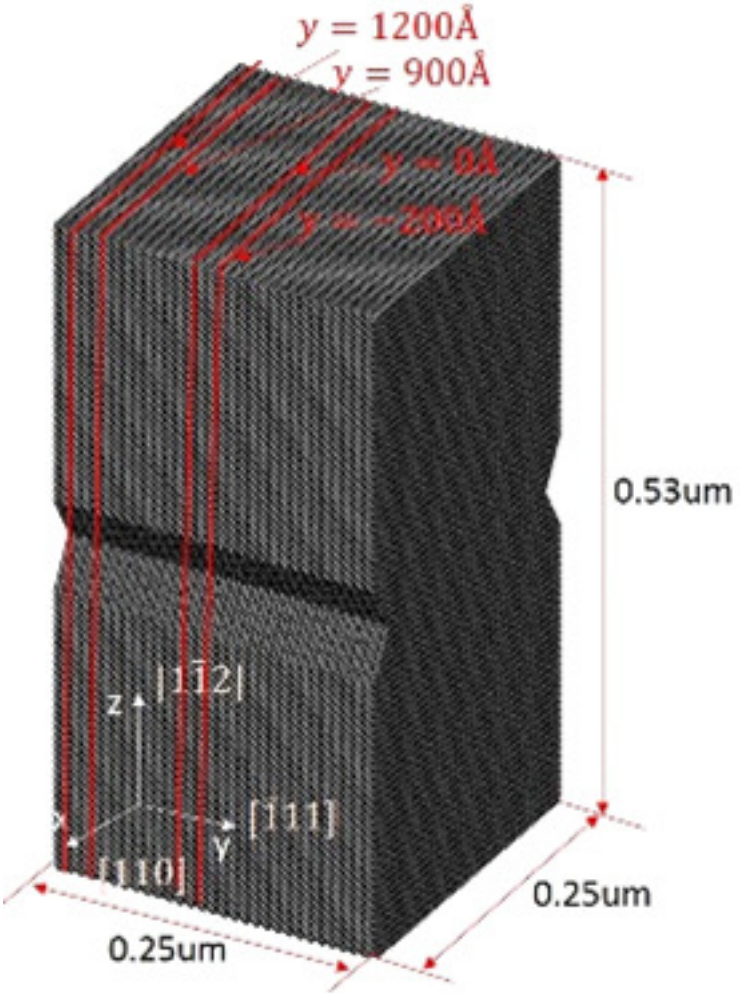

Figure 6.10 CAC model for a billion-atom system to benchmark the spatial decomposition algorithm.

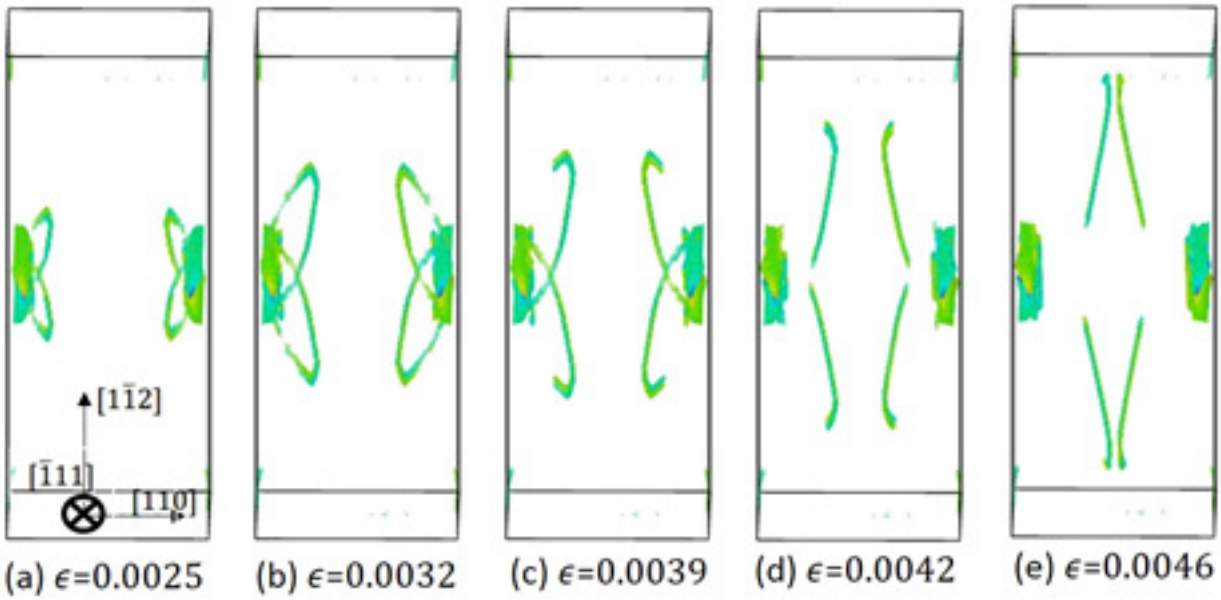

Figure 6.11 Dislocations nucleation and migration in a billion-atom sample by CAC.

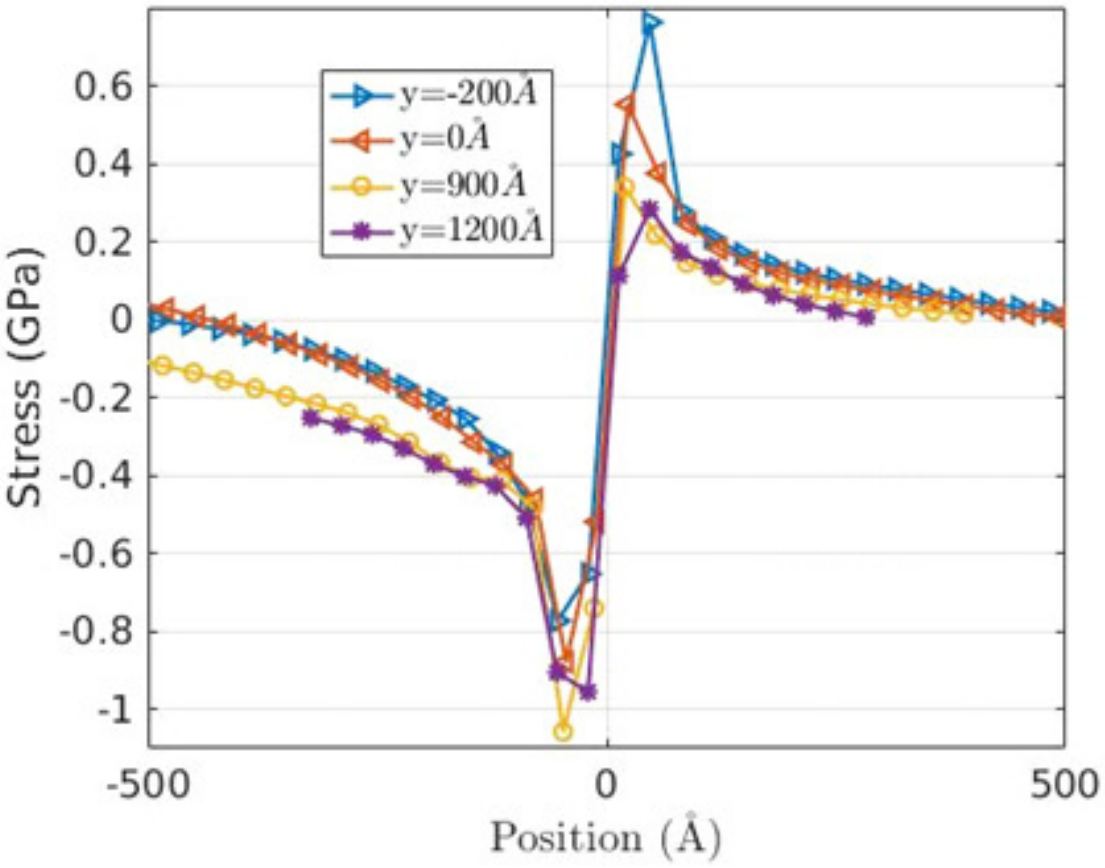

Figure 6.12 Shear stress (σ_{xz}) field around the cores of dislocation in different cutting planes.

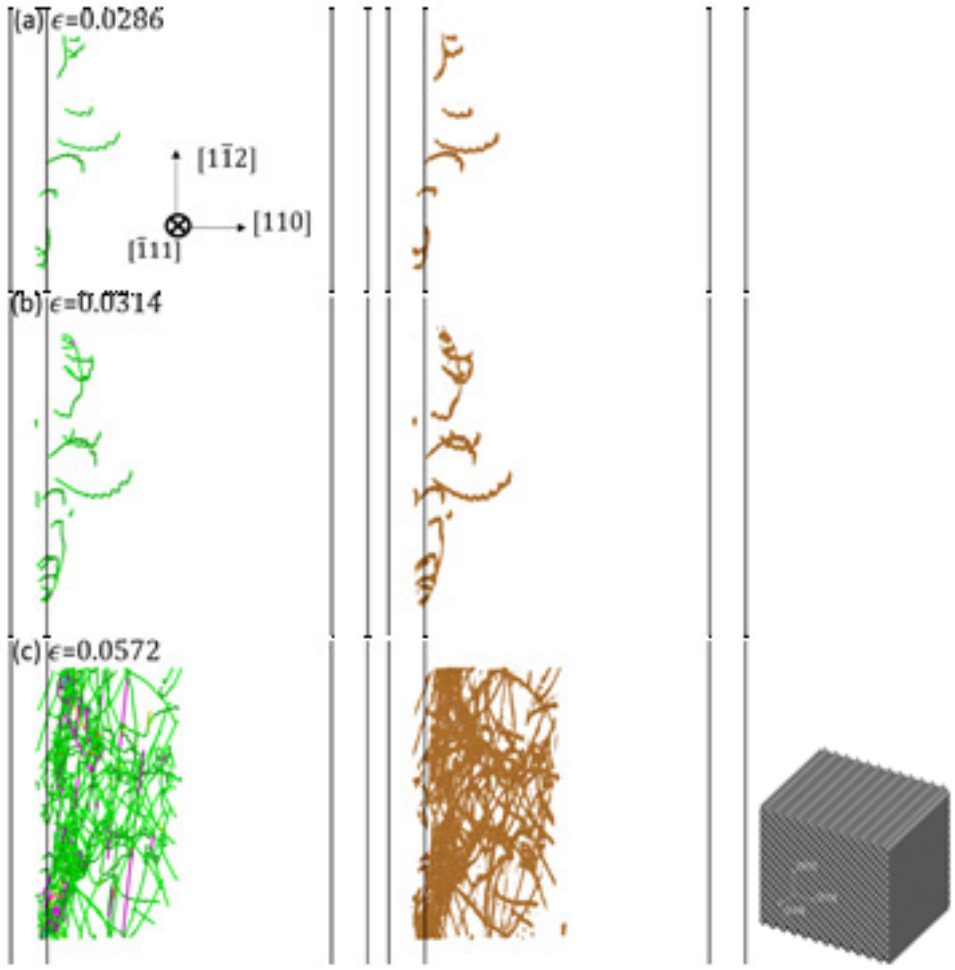

Figure 6.13 CAC (24,890 coarse elements) simulations of dislocations nucleation and migration in a single crystalline EAM-Cu containing 54,683,330 atoms: (a) dislocations nucleate from the free surface on one side.; (b) the nucleated dislocations migrate into the interior of the sample; (c) the dislocation forests are formed as more and more dislocations interact with each other to form stair-rod locks [4, 23]. Here the dislocation analysis is conducted using two different approaches. The dislocation structure in the left column is from the dislocation extraction algorithm in OVITO [45]. This analysis shows that the dislocations (green line) in this simulation are in Burges vector of $\frac{1}{6}$[112] and the purple lines are the stair-rod locks. The dislocation structure in the right column is from the centrosymmetry analysis [45], in which the atoms with centrosymmetry parameter smaller than 0.1 are removed. The black lines above are boundaries of the box.

CHAPTER 7. GENERAL CONCLUSION

First, a conceptually novel approach and a specific crystal lattice instability criterion, which predicts the initiation of the first order PTs in materials under general multiaxial loadings, are developed and validated. In contrast to the existing traditional instability criteria (such as zero moduli or soft phonon modes), the developed approach includes an order parameter, which describes the entire dissipative transformation process. The proposed criterion is rigorously derived utilizing the second law of thermodynamics. The criterion is proven to represent material properties and is independent of the type of the prescribed stress or strain measures. The criterion is validated through hundreds of MD simulations, for direct and reverse PTs between Si I and Si II phases under various combinations of three normal and three shear stresses. The correspondence between theory and simulations is excellent, deviation does not exceed 2%. Most interestingly, all three shear stresses do not affect instability, which directly follows from our theory but sounds very counterintuitive compared to traditional approaches. The criterion is linear in all stress components and can be calibrated by simulations at only two different stress states. Thus, it represents a predictive analytical tool, which determines how to combine six stress components to initiate various PTs in materials. Traditional approaches do not supply an analytical expression and require numerical simulations for each stress state. That is why there was no data in literature for PT criteria under more than two stresses. The obtained results also significantly advance the generalized Landau-type theory for PTs in terms of unexpected dependence of transformation strain, elastic and thermal parts of the free energy as functions of an order parameter. Second, we performed a comprehensive DFT study of the phase transition between semiconducting Si I and metallic Si II under all six components of the stress tensor with normal stresses along 110, $11\bar{1}$, and 001 directions. We investigated the stress-strain curves, elastic lattice instabilities, the electronic band gap, and metallization. The key results is that Si I to Si II PT can be described by the critical value of the modified transformation

work obtained within a phase field formalism. Thus, with normal stress σ_3 in 001 direction, the PT criterion is linear in normal stresses, depends on $\sigma_1 + \sigma_2$; is independent of $\sigma_1 - \sigma_2$ and shear stress τ_{21} acting alone or with one more shear stress; contribution of all shear stresses can be described through the theoretically predicted geometric nonlinear term (without any additional adjustable constants). The PT criterion contains just two adjustable parameters, which can be calibrated by instability stresses at two different stress states without shears. Those parameters can be fitted to DFT results or experiment. Then our criterion accurately describes instability in a broad range of variations of all six components of the shear tensor. While Si I to Si II occurs due to elastic instability, the modified transformation work criterion is based on completely different principles and assumptions. In particular, it considers the entire dissipative PT process described by the transformation strain tensor and does not include the terms with a discontinuity in elastic moduli, in order to avoid nonlinearity in normal stresses. Using these paradoxical results, we formulate a problem of finding a fundamental relationship between the elastic instability and the modified transformation work criterion, which will be studied in future works. The elastic instability analysis for the simplest model with quadratic in E energy qualitatively reproduces our main results for relatively low stresses. The PT pressure under hydrostatic condition is 20 times larger than under uniaxial loading. Such a strong effect of nonhydrostaticity at least partially explains the significant difference between the experimental PT pressure (9-12 GPa) and the instability pressure of 75.81 GPa, as well as a scatter in the experimental data under quasi-hydrostatic conditions.

Although the stress-strain curve is continuous, the electronic PT precedes the structural PT. That means that under stresses there is a metallic Si I. Metallization can be caused by compressive or tensile stresses, and the effect of nonhydrostatic stresses is extremely strong. In the (σ_1,σ_3) plane it is described by a closed contour, which can be approximated by two straight lines and a parabolic cap. Only one of the metallization lines is relatively close and approximately parallel to the Si I to Si II PT line. Interestingly, metallization occurs deeply in the region of stability of Si I and is not causing the Si I to Si II structural PT. Surprisingly, a stress-free Si II is metastable in DFT. Although at zero pressure Si II has a higher enthalpy than Si I, both Si I and Si II correspond

to local enthalpy minima and both have stable phonons. In addition, shear stress-strain curves are obtained for different simple shears and their combinations at different normal stresses. A shear instability competes with a tetragonal instability, which does not lead to Si II, but rather to possible amorphization or hexagonal diamond Si IV. Pressure and compressive normal stresses reduce shear stresses below and at the shear instability strain. Under hydrostatic or near-hydrostatic conditions, shear instability in Si I occurs earlier than tetragonal instability, which may result in amorphization. Third, Using molecular dynamics (MD), special triaxial compression-tension states were found for which stresses for instability of crystal lattice of silicon (Si) are the same for direct and reverse phase transformations (PTs) between semiconducting Si I and metallic Si II phases. This leads to unique homogeneous and hysteresis-free first-order PTs, for which each intermediate crystal lattice along the transformation path is in indifferent thermodynamic equilibrium and can be arrested and studied by fixing the strain in one direction. By approaching these stress states, a traditional two-phase system continuously transforms to homogenous intermediate phases. This also allows one to stabilize unique heterogeneous intermediate structures, which may possess unexpected properties. Zero hysteresis and homogeneous transformation are the optimal property for various PT applications, which reduce damage and energy dissipation. Further increases in stresses substitutes the first-order PT with the unusual second-order PT, without intracell atomic displacements and change in symmetry, and at large strains. Fourth, a SD parallel algorithm for a multiscale simulator, CAC, is developed and implemented. Results obtained using the newly parallelized CAC simulator are directly compared with those from MD simulations. It shows that the newly developed CAC simulator can effectively reproduce dislocation nucleation, migration and the formation of Lomer-Cotrell lock formation as that in MD simulations. Furthermore, the parallel algorithm has been tested in CAC using different number of processors for different models. Using only 512 processors, CAC furnished with this new algorithm exhibits an optimal scalability in computer models which contains up to 4,809,108 elements for 10,565,610,276 atoms. This is beyond the reach of classical MD simulator using the same computational resource. The parallel efficiency is shown to be more than 90% and is compared with a well-established atomistic

simulator, LAMMPS. For the CAC models with the atomic-scale finite element meshes which reproduce the full MD simulation results, the parallel algorithm achieves 97% efficiency of LAMMPS. To demonstrate the capability of the newly parallelized CAC simulator, dislocation activities in a large sample containing 2,307,616,753 atoms are simulated. The maximum positive shear stress around a dislocation core in the finite-sized sample was found to gradually decay when it get closer the free surface. It approaches the analytical solution for the stress field around a dislocation core embedded in an infinite media when the core is at least $120nm$ away from the free surfaces. It should be noted that the majority of existing concurrent multiscale method is based on domain decomposition, the present SD parallel algorithm can be applied to those methods and provide a general framework for parallelizing many other multiscale materials simulators. In order to use CAC to simulate more complicated phenomena such as dislocation interaction with obstacles such as voids or grain boundaries, the atomic-scale finite element mesh nearby the obstacles needs to be combined with coarse elements. The computer models with non-uniform meshes with different element sizes in the newly parallelized CAC code will be tested in our future work. Fifth, In the paper, the interactions between tilt GBs and a shuffle screw dislocation in silicon are investigated using molecular dynamics. Results show that the dislocation transmits into the neighboring grain for all GBs. For $\Sigma 3$ GB, the dislocation goes through the GB directly. For $\Sigma 9$ and $\Sigma 19$ GBs, when the dislocation is on heptagon site, the dislocation transmits the GB directly as well. However, when the dislocation is on the pentagon site, it first cross slips to a plane on the heptagon site and then transmits the GB. The energy barrier was calculated using the climbing image nudged elastic band method. Results show that $\Sigma 3$ GB generates the barrier at the level of the Peierls barrier. For both $\Sigma 9$ and $\Sigma 19$ GBs, the barrier for dislocation transmission of heptagon sites is 0.6ev/nm, while it is 1.9ev/nm for pentagon defects. Furthermore, we found that the critical shear stress for the transmission is lowered from 5.3GPa to 2.9GPa for moving dislocation versus the static dislocation. Since energy barrier for crossing the $\Sigma 3$ is equal to the Peierls barrier for dislocation motion in bulk, and for $\Sigma 9$ and $\Sigma 19$ GBs at the heptagon defects it is only slightly larger than the Peierls barrier, perfect screw dislocations cannot pile up against these GBs and cannot reduce phase trans-

formation pressure during plastic deformations. At last, interaction between shuffle 60^o dislocations and $\Sigma 3$ and $\Sigma 9$ GBs are investigated using atomistic simulations. Results show that a dislocation pile-up along the GBs can activate the formation of an amorphous shear band in the neighboring grain. For different GBs, two different mechanisms of amorphizations were observed. For GB with relative small inclination angle, i.e., low-angle GBs, like $\Sigma 9$ and $\Sigma 19$ GBs, the intermediate phase is formed through the rotation of a very thin band of the crystals accompanied by dis location nucleations. However, for GBs with a large inclination angle, like $\Sigma 3$, the intermediate phase is an amorphous core. The amorphous shear band grows when more dislocations pile up at the GBs. The critical shear stress needed for the formation of the amorphous shear band decrease linearly with the number of dislocation pileup being increased. When the number of dislocations in a pileup increases from 3 to 8, for $\Sigma 9$ GB, the critical shear stress drops from 4.7GPa to 1.6GPa. For $\Sigma 3$ GB, it drops from 4.6GPa to 2.1GPa. Comparing with the shear stress to form amorphous shear band for perfect crystal both from MD (8.1GPa) and experimental (10GPa) results, dislocation pileup along the GB can greatly reduce the shear stress for the formation of the amorphous shear band. This new mechanism for forming amorphous shear band can have a potential application in machining silicon in semiconductor industry. This mechanism may be also found in other covalent materials.